The Dissertation Committee for Chinmaya Baburao Patil
certifies that this is the approved version of the following dissertation:

Robust Design of Selectively Compliant Flexure-based Precision Mechanisms

Committee:

S. V. Sreenivasan, Supervisor

Raul G. Longoria, Supervisor

Richard H. Crawford

Joseph J. Beaman Jr.

Byung-Jin Choi

Robust Design of Selectively Compliant Flexure-based Precision Mechanisms

by

Chinmaya Baburao Patil, B.E., M.S.

DISSERTATION

Presented to the Faculty of the Graduate School of
The University of Texas at Austin
in Partial Fulfillment
of the Requirements
for the Degree of

DOCTOR OF PHILOSOPHY

THE UNIVERSITY OF TEXAS AT AUSTIN
May 2008

Dedicated to my family.

Acknowledgments

I wish to thank a number of people who have helped me in my professional and personal development during my graduate studies at The University of Texas at Austin.

Firstly, I would like to express my sincere gratitude to Prof. Raul G. Longoria, who has been more than a mentor to me. His guidance, motivation, and support have been critical in all my accomplishments in graduate school.

I would like to thank Prof. S. V. Sreenivasan, who helped me to overcome my weaknesses, by instilling discipline and confidence in my work. His professionalism and down-to-earth demeanor will always be inspirational to me.

Thanks go to my dissertation committee members, namely, Prof. Joseph J. Beaman Jr., Prof. Richard H. Crawford, and Dr. Byung Jin Choi for their valuable suggestions in improving the dissertation. I would like to especially thank Dr. Choi and engineers at Molecular Imprints, namely, Pawan Kumar, and Mario Meissl, for their help with the experimental work included in the dissertation.

I thank the Mechanical Engineering Department, the Cockrell School of Engineering, and the Office of Graduate Studies for financial support throughout my graduate education.

Finally, a special note of appreciation to my family members. To my beloved wife, Rashmi, whose many sacrifices, and unflinching support carried us through the travails and triumphs of higher education, I couldnt be more thankful. To my parents, for their patience, encouragement, and faith in me, I am always grateful.

Robust Design of Selectively Compliant Flexure-based Precision Mechanisms

Publication No. ____________________

Chinmaya Baburao Patil, Ph.D.
The University of Texas at Austin, 2008

Supervisors: S. V. Sreenivasan
Raul G. Longoria

Nano-scale positioning and metrology are at the cutting edge of motion control technology, driven by ever-increasing number of applications, including semiconductor fabrication, data storage, nano-fabrication, biotechnology among others. In this 'very small range (few μm) and very high precision (few nm) domain', flexure-based mechanisms are the preferred means for the motion guiding systems, because of several exceptional properties like selective compliance, monolithic design, absence of friction, hysteresis, and wear. However, despite their numerous advantages, their motion characteristics are extremely sensitive to thermal variations, material property variations, machining tolerances among others. The geometric errors induced by machining process variations interact with the mechanism geometry, and lead to parasitic motion in directions other than the mechanism degrees of freedom. These errors cannot be completely eliminated by calibration, as they are coupled with the desired mechanism motion.

This thesis focuses on the problem of parasitic motion in flexure based precision compliant mechanisms in the presence of geometric errors induced by machining tolerances. A spatial kinematics approach based on screw systems is used to model the compliance of the flexure mechanisms. The geometric errors induced by machining tolerances are systematically included in the modeling. The model not only determines the complete spatial motion of flexure mechanisms, but also provides geometric insight into the parasitic motion problem, which leads to decoupling of error motions into intrinsic and extrinsic parasitic motion. The intrinsic error motion is shown to be tied to the mechanism motion, and cannot be corrected by calibration. A metric to quantify the intrinsic error motion is obtained for both rotational and translational degree of freedom systems, and is used to define the precision capability of the flexure mechanisms. The model is used to formulate an optimization problem that aims to minimize the intrinsic parasitic motion metric by optimal joint compliance design. The stochastic optimization problem is solved numerically for both rotational and translational flexure mechanisms with one degree of freedom. A test setup is developed to characterize the pitch of screw motion of a one degree of freedom rotational flexure mechanism. The experimental results validate the existence of intrinsic parasitic motion. The setup demonstrates the metrology capability required for parasitic motion characterization, and forms a preliminary prototype for a quality control station for evaluating precision capability of flexure mechanisms.

Significant contributions from the proposed work include, (1) complete

mathematical and geometric interpretation of parasitic motion of flexure mechanisms due to machining tolerances, (2) formulation and solution of the flexure mechanism joint compliance robust design problem applied to rotational and translational one degree of freedom mechanisms, (3) development of an experimental setup to characterize the spatial parasitic motion of one DOF rotational flexure mechanism, that forms the basis of a modular quality control station in a ‘test-and-select’ approach for precision flexure-based compliant mechanisms.

Table of Contents

List of Tables

List of Figures

Chapter 1

Introduction

1.1 Ultra-precision Motion Guidance

Nano-scale precision motion guiding is at the cutting edge of motion control systems technology. They form the foundation for a vast number of applications, such as imprint lithography based semiconductor fabrication [1, 2] striving to pack more integrated circuits on silicon chips, biotechnology aiming to manipulate individual DNA molecules[3, 4], development of MEMS systems for fabrication of nano devices [5, 6], development atomic force microscopes for scanning surfaces at sub-nanometer scale [7, 8]. Some of these applications are depicted in Figure 1.1.

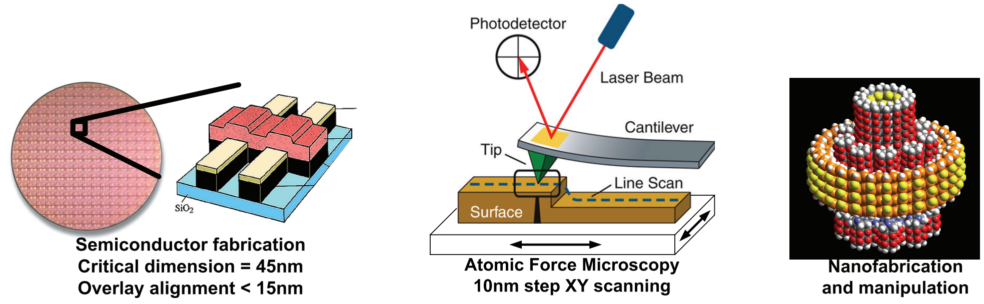

(a) (b) (c)

Figure 1.1: Applications requiring precision motion guidance.

The common requirement for each of these applications is motion guidance over a very small range, of the order of few microns, and with very high repeatability, of the order of a nanometer or less. The technologies that enable this 'very small range and very high precision' positioning include magnetic levitation, air-bearings, and compliant flexure mechanisms. By avoiding contact between parts in relative motion, thereby eliminating the problems associated with friction, these systems are able to achieve positioning with nano-scale precision. Magnetic levitation and air bearings enable comparatively larger motion ranges (few cm) than compliant mechanisms. However, compliant mechanisms are inherently stable systems in contrast to both magnetic levitation and air-bearings which require stabilizing control for operation. Flexure mechanisms rely on material elasticity to enable fine motion, and are suitable for passive operation, leading to reduced system cost [9]. Besides, they exhibit several exceptional properties like monolithic design, particle-free operation for vacuum and clean rooms compatibility required by many of the aforementioned applications, well developed precision manufacturing processes, all of which make them the leading technology in the precision positioning [10].

While compliant mechanisms can be of distributed nature (see for example [11–14]), lumped compliant mechanisms are preferred for precision motion guiding applications. The use of localized compliance in the form of flexure joints enables superior control over the mechanism stiffness in the controlled and constrained directions, which is critical for mechanisms with fewer than six degrees of freedom [15]. Many different designs of flexure joints are available [9], but the notch type right circular flexure joint is most commonly used in precision applications. The properties of the notch type flexure joint including its compliance characteristics, precision of motion, stress distribution etc have been well documented [9, 16]. Figure 1.2 shows some examples of precision mechanisms based on notch type flexure joint.

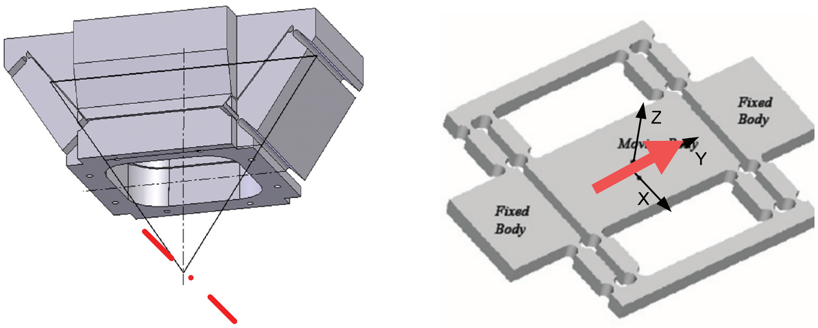

(a) One DOF Rotation [1] (b) One DOF Translation [17]

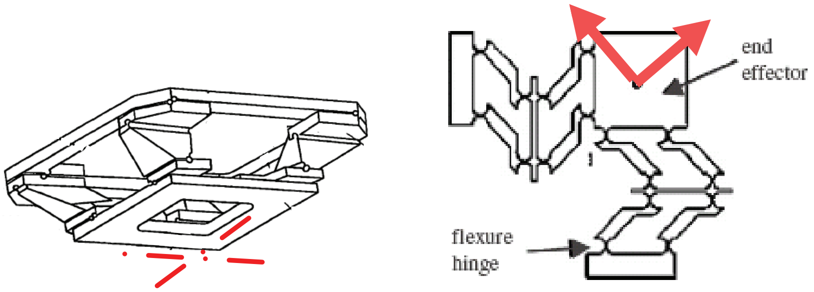

(c) Two DOF Rotation [18] (d) Two DOF Translation [19]

Figure 1.2: Examples of flexure-based precision mechanisms.

1.2 Parasitic Motion

Despite their many excellent properties, the motion characteristics of the selectively compliant flexure-based mechanisms is highly sensitive to many disturbances. Significant discrepancy can exist between the desired and actual motion at the nano-scale due to thermal variations, vibration, manufacturing tolerances, material property variations etc. Any undesirable motion along the constrained directions of the mechanisms decreases the precision capability and is termed as parasitic motion. Although thermal variations and vibration significantly contribute to the parasitic motion, they are external to the flexure mechanism itself, and their influence can be minimized by proper engineering practices like thermal/vibration isolation, material selection, etc. Material property variations occur with a small spatial frequency, hence their effects within a single flexure mechanism can be neglected. The manufacturing tolerances on the other hand are built into the flexure mechanisms, irreversibly changing their motion characteristics. Flexure mechanisms achieve their degrees of freedom via selective compliance, which relies on special geometric arrangement of joints in the mechanism. Machining process variations induce geometric errors that intrinsically perturb the flexure mechanism kinematics.

As an example, Figure 1.3 shows a rigid-link one rotational DOF four-bar mechanism and its equivalent flexure-based precision mechanism. A geometric requirement for the four-bar mechanism to possess its rotational DOF is that all the joint axes must be parallel to one another [20, 21]. Finite machining tolerances in the fabrication of flexure mechanism induce perturbation in the joint axes that violate the geometric condition. The rigid-link four-bar mechanism requires clearances in joints to accommodate this condition and exhibit the rotational DOF. Although clearances are not available in flexure joints, the flexure four-bar mechanism will move by virtue of the compliance in the joints. When acted upon by external forces, the compliance of the joint about directions other than the sensitive axis are activated. This changes the mechanism topology, as the flexure joints no longer behave as simple revolute joints, and the resulting mechanism motion is no longer purely rotational. The geometric perturbations lead to undesirable parasitic effects in many other selectively compliant flexure mechanisms, such as out-of-plane motion in planar XY stages [22–24], rotation in a single degree of freedom translation stage [25], translation in a single DOF rotation alignment stage [1] Overall, the undesirable motion significantly reduces the nano-scale precision capability of the flexure mechanisms.

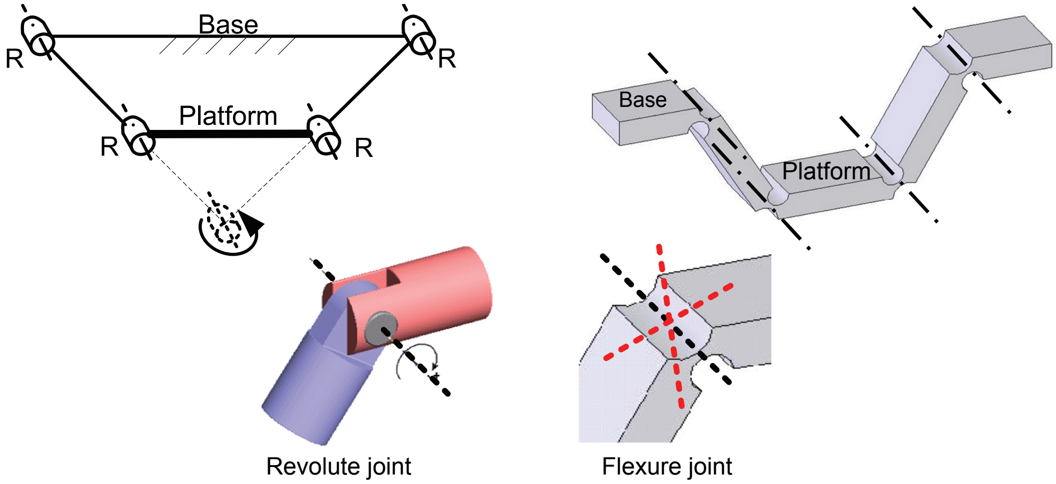

Figure 1.3: Four-bar mechanism.

1.3 Research Outline

Reducing the tolerance limits by reducing the machining process variations can mitigate the parasitic motion, however, the cost associated may be prohibitively high, or it may be infeasible [26]. Active compensation of the parasitic motion may be impractical, because it requires not only additional degrees of freedom of the mechanism along constrained directions (thus defeating the selective compliance purpose of the flexure mechanisms) but also sophisticated calibration equipment and techniques [27], which add to the cost significantly. This motivates the analysis of parasitic motion in compliant flexure mechanisms due to the geometric errors induced by machining tolerances, and systematic ways to synthesize the mechanisms with reduced sensitivity to the machining process variations.

The complexity of the flexure mechanisms owing to the coupled nature of geometry and compliance, in addition to the statistical nature of the machining tolerances, makes both the analysis and synthesis problems challenging. The analysis and design of rigid-link mechanisms has been a classical area of research in the robotics world, and the underlying geometry is well understood. However, the analysis of flexure mechanisms motion characteristics has been limited only to numerical approaches. Ryu [28] discusses the various machining tolerances of a notch type flexure joint, and presents a parametric model and simulation results for the worst-case parasitic motion of a one DOF translation stage. Niaritsiry [29] presents similar study for a delta-type translation manipulator. Smith [17] discusses the use of elastic averaging as a means to reduce the parasitic motion of a precision translation stage. Huh [30] presents a finite element based approach to characterize the uncertainty in performance of a nano-positioning device. While these models enable numerical calculation of the error motions of flexure mechanisms, they do not present any insight into either the geometry of the flexure mechanism, or the synthesis of robust mechanisms. Further, the design of flexure mechanisms, in general, focuses on the 'type synthesis' of the mechanism to obtain the desired degrees of freedom, sizing the flexure joints to achieve the required range of motion while keeping the maximum stress in the joints within the elastic region for the material [16]. Little or no emphasis is placed on the robustness of the mechanism to parasitic motion.

This thesis addresses the problem of parasitic motion in flexure based compliant mechanisms. The research is outlined below. A spatial kinetostatic model of the compliance of flexure mechanisms based on screw systems [31, 32] is developed for the analysis of parasitic motion. The analytical model systematically includes the machining process variations as geometric error parameters of flexure joints. A unique advantage of the screw systems based model is that, it not only provides the minimal representation of complete spatial motion characteristics, but also captures the underlying geometry of the flexure mechanisms motion. Screw systems have been extensively investigated for the purposes of robot compliance analysis [33–35] and synthesis [36, 37], and robot control [38, 39]. Here, the approach is extended to analyze the mobility of flexure-based mechanisms by accommodating the compliance of the flexure joints that make up the mechanisms. By studying the parasitic motion of flexure mechanisms in terms of screw systems rather than the numerical values, it is shown that the overall undesirable motion can be decoupled into two parts, extrinsic and intrinsic. The extrinsic parasitic motion is found to be correctable by calibration procedures [40, 41], while the intrinsic parasitic motion is inherently tied to the flexure mechanism motion and cannot be corrected apriori. Thus the extent of intrinsic motion associated with a flexure mechanism defines the precision capability of the mechanism. The analysis is demonstrated using a one DOF rotational mechanism, and a one DOF translation stage, and the geometric errors due to machining process variations are shown to perturb the screw systems of motion of the mechanisms from the special first order systems to the general first order system. Extension to two DOF flexure mechanisms illustrates the general applicability of the developed parasitic motion analysis. The details of the analysis are presented in Chapter 2.

In order to demonstrate the metrology capability required to measure the nano-scale parasitic motion of precision flexure mechanisms, a test setup is built to experimentally determine intrinsic error motion of a one DOF rotational flexure mechanism. Although, a six axis motion measurement scheme is required for complete motion measurement of the mechanism, it is shown that an estimate of the intrinsic parasitic motion can be obtained via a simplified arrangement using only three precision displacement sensors. The test setup is built as per the three axis measurement scheme, and two experiments are carried out. Firstly, the effective rotational compliance of the mechanism is determined, and verified via finite element analysis to illustrate the effectiveness of the test setup. Then, the parasitic motion of the one DOF mechanism is determined. The results validate the concept of intrinsic error motion of flexure-based compliant mechanisms. The test setup serves as a preliminary proof-of-concept for a modular 'quality control' setup that can be used to determine the precision capability of general flexure mechanisms. Chapter 3 covers the setup design and experimental results.

Finally, the problem of synthesis of flexure mechanisms that are robust to machining process variations is investigated. The analytical model of compliance of the flexure mechanisms presents four approaches to reduce the parasitic motion in flexure mechanisms. A system design approach is pursued in this research. The decoupling of parasitic motion is critical in the formulation of the robust design problem, since the design can focus on minimizing the intrinsic parasitic motion. The metrics to quantify the intrinsic parasitic motion of general flexure mechanisms are obtained from the screw systems analysis. The geometric parameters of the notch-type flexure joint are used as the design variables, and the design problem is solved via an optimization scheme to minimize the parasitic motion metric. The statistical nature of the machining tolerances is accounted for by sampling the random geometric error parameters at every iteration step of the optimization, leading to a stochastic optimization formulation. The results of optimization are presented for a one DOF rotational mechanism, a one DOF translation stage, and a two rotational

DOF tip-tilt flexure mechanism. The varying degree of improvement in the precision capability of the flexure mechanisms is shown to be related to the improvement in the mechanism compliance distribution via Eigen-screw analysis. The nature of the global optimization problem is discussed for the one DOF rotational flexure mechanism. Details of the robust design are discussed in Chapter 4.

1.4 Contributions

The research presented in this thesis makes the following contributions in the study of motion characteristics of precision flexure-based compliant mechanisms.

- The analysis of flexure mechanisms using screw systems is the first mathematical/geometric characterization of intrinsic parasitic motion, leading to classification and quantification of the error motions. The concept of intrinsic parasitic motion is shown to be applicable to general flexure mechanisms. Metrics to quantify the intrinsic error motion of rotational and translational DOF mechanisms are defined based on screw systems analysis.

- A test setup is developed to demonstrate the metrology capability requirement for experimental investigation of parasitic motion of flexure mechanisms. It is used to determine the pitch of screw motion of a one DOF rotational flexure mechanism.

- The problem of robust synthesis of flexure-based precision compliant mechanisms is developed based on the parametric compliance model. Geometric parameters of flexure joints are chosen via an optimization scheme to minimize the intrinsic parasitic motion metric. Results of optimization are presented for several candidate mechanisms, and the enhanced robustness is shown to be related to improvement in compliance distribution in the mechanisms.

Chapter 2

Parasitic Motion Analysis of Flexure Mechanisms

The analysis of parasitic motion of flexure-based selectively compliant mechanisms due to geometric errors induced by machining tolerances is covered in this chapter. The development of the spatial kinetostatic modeling of flexure mechanism motion based on screw systems is presented first. The model is used to study the spatial motion characteristics of a one rotational DOF, and a one translational DOF flexure mechanisms in the presence of geometric uncertainties. The results of the analysis are used to define the extrinsic and intrinsic parasitic motion for both the rotational and translational DOF mechanisms. The metrics for intrinsic parasitic motion are identified, and the notion of flexure mechanism precision capability is defined. The analysis is finally extended to two DOF flexure mechanisms. The parametric model developed here for parasitic motion analysis forms the basis of the robust synthesis approach developed in the next chapter.

2.1 Flexure Mechanism Motion Modeling

A flexure-based compliant mechanism is a passive system, designed to operate when actuated by external forces. The kinematics of the mechanism and the compliance of the flexure joints are designed to ensure high compliance along the degrees of freedom, and high stiffness along the constrained directions. This selective compliance coupled with the external forces generates the desired motion of the flexure mechanism. Although large unregulated forces can induce undesirable motion in the mechanism along the constrained directions, despite the high design stiffness, the applications requiring ultra precision positioning all include very high degree of control over the actuation forces. Under the assumptions of small travel range, and quasi-static operating conditions, the compliance of the flexure mechanism in the 'task space' maps any external force to the spatial motion of the mechanism. This is shown as a block diagram representation in Figure 2.1. The quasi-static operation is justified by the high fundamental natural frequency design of flexure mechanisms, which is required to promote vibration isolation.

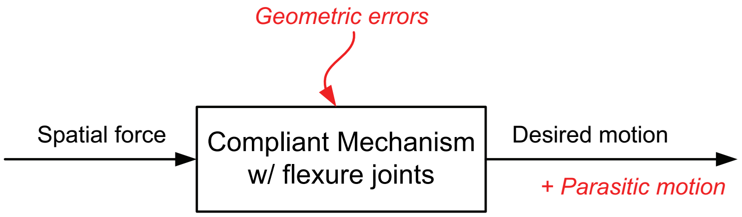

Figure 2.1: Flexure mechanism motion modeling.

As the task-space compliance depends on the mechanism geometry, errors induced by machining process variations perturb the compliance and induce undesirable parasitic motion. The analysis of parasitic motion can thus be accomplished by determining the compliance of flexure mechanism in terms of the joint geometry and compliance, and accounting for the influence of geometric errors. The modeling of an ideal flexure mechanism compliance is presented first. The geometric errors induced by machining process variations, and their influence on the flexure mechanism compliance are then included in the model.

The modeling approach followed here is based on spatial kinematics or screw theory for two primary reasons. Firstly, the geometric entity of a screw provides a minimal representation of spatial motion and force [31, 32, 42], and effectively captures the spatial nature of the mechanism parasitic motion. Secondly, the rich theoretical developments from screw theory can be adapted towards the analysis and synthesis of compliant mechanisms, giving superior insight into the problem. A short review of representing spatial quantities using screws is presented first, in order to establish the notation used in the thesis. This is followed by the compliance modeling.

2.1.1 Representation of Spatial Motion, Force and Compliance Using Screw vectors

A unit screw is a purely geometric entity, represented by a 6×1 vector in some reference frame 'i' as,

$$ {}^{\mathrm{i}}\hat{\$} = \begin{bmatrix} \mathbf{w} \\ \mathrm{h}\cdot\mathbf{w} + \boldsymbol{\rho}\otimes\mathbf{w} \end{bmatrix} \tag{2.1} $$

where, **w** is a 3 × 1 unit vector defining the screw orientation, and $\boldsymbol{\rho}$ is a 3 × 1 vector defining the screw location in the reference frame i, and h is a scalar quantity, called pitch of the screw. $\otimes$ represents the vector cross product operation. The pre-superscript 'i' identifies the reference frame in which the screw is defined. Two special cases of the screw are identified by the value of pitch; a zero pitch screw is called a line vector, while an infinite pitch screw is called a zero vector. Given a screw, its pitch can be determined as,

$$ \mathrm{h} = \left(\frac{1}{2}\right)\cdot\frac{\hat{\$}^{\mathrm{T}}\cdot\Delta\cdot\hat{\$}}{\hat{\$}^{\mathrm{T}}\cdot\Gamma\cdot\hat{\$}} \tag{2.2} $$

Here, the superscript T indicates transpose operator, and,

$$ \Delta = \begin{bmatrix} \mathbf{0}_{3\times3} & \mathbf{I}_{3\times3} \\ \mathbf{I}_{3\times3} & \mathbf{0}_{3\times3} \end{bmatrix}, \Gamma = \begin{bmatrix} \mathbf{I}_{3\times3} & \mathbf{0}_{3\times3} \\ \mathbf{0}_{3\times3} & \mathbf{0}_{3\times3} \end{bmatrix} \tag{2.3} $$

Here, **I** is the identity matrix, and **0** the zero matrix.

By associating the unit screw with scalar quantities of angular displacement or force, a representation for the spatial motion, namely a twist, or spatial force, namely a wrench, are obtained, respectively. This is indicated below.

$$ {}^{\mathrm{i}}\hat{\mathrm{t}} = {}^{\mathrm{i}}\hat{\$}\cdot\theta = \begin{bmatrix} \boldsymbol{\theta} \\ \boldsymbol{\delta} \end{bmatrix} \rightarrow \text{twist} \tag{2.4} $$

$$ {}^{\mathrm{i}}\hat{\mathrm{f}} = {}^{\mathrm{i}}\hat{\$}\cdot f = \begin{bmatrix} \mathbf{f} \\ \mathbf{m} \end{bmatrix} \rightarrow \text{wrench} \tag{2.5} $$

Here, θ and f are the scalar physical quantities representing angular displacement and force, respectively. Also, $\boldsymbol{\delta}$ is the linear displacement of the origin of the reference frame 'i' due to the twist, and $\mathbf{m}$ is the moment about the origin due to the wrench. Depending upon the value of the pitch of the screw, the twist can represent either pure rotation (zero pitch), or pure translation (infinite pitch). Similarly, the wrench can be either pure force (zero pitch) or pure moment (infinite pitch).

A flexure joint can be completely characterized by a unit screw defining the joint geometry, and a lumped scalar compliance value which defines its elastic property. A 6 × 6 matrix form is used to represent the joint compliance to indicate that it maps any wrench acting on the joint to the joint twist, i.e.,

$$ {}^{\mathrm{i}}\hat{\mathrm{t}} = {}^{\mathrm{i}}\mathbf{C} \cdot {}^{\mathrm{i}}\hat{\mathrm{f}} \tag{2.6} $$

The joint compliance matrix $\mathbf{C}$ in terms of the joint screw and the scalar compliance 'c' is given by,

$$ {}^{\mathrm{i}}\mathbf{C} = {}^{\mathrm{i}}\hat{\$} \cdot \mathrm{c} \cdot {}^{\mathrm{i}}\hat{\$}^{\mathrm{T}} \cdot \Delta \tag{2.7} $$

This definition of the joint compliance can be used to represent both rotational and translational compliant joints; for rotational compliance, $\hat{\$}$ is a line vector with 'c' having the units of [rad/Nm], and for linear compliance $\hat{\$}$ is a zero vector with 'c' having the units of [m/N]. The expression of the joint compliance matrix can be interpreted as follows. By substituting equation (2.7) into equation (2.6), the expression for twist of motion is obtained as,

$$ {}^{\mathrm{i}}\hat{\mathrm{t}} = {}^{\mathrm{i}}\hat{\$} \cdot \mathrm{c} \cdot {}^{\mathrm{i}}\hat{\$}^{\mathrm{T}} \cdot \Delta \cdot {}^{\mathrm{i}}\hat{\mathrm{f}} \tag{2.8} $$

Here, the term $\left({}^{\mathrm{i}}\hat{\$}^{\mathrm{T}} \cdot \Delta \cdot {}^{\mathrm{i}}\hat{\mathrm{f}}\right)$ represents the reciprocal product of the wrench and the joint screw [31]. The result of the reciprocal product is a scalar quantity that defines the effective moment (rotational compliance) or force (translational compliance) acting on the joint due to the wrench. The effective moment or force when multiplied with the scalar compliance 'c' determines either an angular (for rotational compliance) or linear (for translational compliance) displacement. This scalar displacement term associated with the joint screw yields the twist representation of the resulting joint motion.

2.1.2 Flexure Joint Compliance Modeling

In order to account for the complete spatial motion of a flexure mechanism, the flexure joints that make up the mechanism are treated as a six-DOF joint associated with three rotational and three translational scalar compliances. For a flexure joint with symmetrical notches, the rotational and translational compliances are known to be maximally decoupled at the centroidal or principal coordinate frame of the flexure joint [43, 44]. The centers of elasticity and compliance [33, 45] coincide with the origin of the principal coordinate frame for the symmetrical flexure joint. Thus six screws, three line vectors and three free vectors, aligned with the principal coordinate frame of a flexure joint, and associated with rotational (denoted as cx, cy and cz) and translational (denoted as cX, cY and cZ) scalar compliance values respectively, completely describe the compliance of the joint in the local reference frame. This is shown in Figure 2.2 for a notch type flexure joint. The joint screws in their local reference frame together form a identity matrix. The compliance matrix of the flexure joint in the local reference frame of the joint is thus denoted as,

$$\mathbf{c} = \left[\begin{array}{ccc|ccc} \mathrm{cx} & & & & & \\ & \mathrm{cy} & & & \mathbf{0}_{3\times3} & \\ & & \mathrm{cz} & & & \\ \hline & & & \mathrm{cX} & & \\ & \mathbf{0}_{3\times3} & & & \mathrm{cY} & \\ & & & & & \mathrm{cZ} \end{array}\right] \tag{2.9}$$

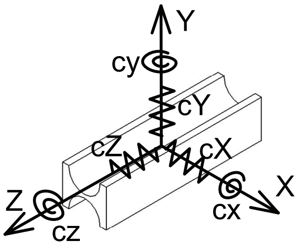

Figure 2.2: Compliance representation of a notch type flexure joint in its local coordinate frame.

In order to obtain the compliance matrix of a flexure joint in the global reference frame of the flexure mechanism, a spatial coordinate transformation matrix is used. The 6 × 6 matrix transforms the flexure joint screws from the local joint reference frame to the global reference frame of the mechanism. If the local joint frame is denoted by '1', and the global frame by '0' (see Figure 2.3), the transformation matrix from frame '1' to frame '0' is defined by [42],

$${}^{0}_{1}\mathbf{X} = \begin{bmatrix} {}^{0}\mathbf{R}_1 & \mathbf{0} \\ (\boldsymbol{\rho}_1 \otimes) \cdot {}^{0}\mathbf{R}_1 & {}^{0}\mathbf{R}_1 \end{bmatrix} \tag{2.10}$$

Here, ${}^{0}\mathbf{R}_1$ is a 3×3 rotation matrix defining the orientation of the frame '1' in frame '0', and $\boldsymbol{\rho}_1$ is a 3×1 vector that defines the location of frame '1' in frame '0'. Also, '$\otimes$' represents the vector cross-product operation. The compliance matrix of the flexure joint in the global reference frame '0' is then,

$$ {}^{0}\mathbf{C} = {}^{0}_{1}\mathbf{X} \cdot \mathbf{c} \cdot {}^{0}_{1}\mathbf{X}^{\mathrm{T}} \cdot \boldsymbol{\Delta} \tag{2.11} $$

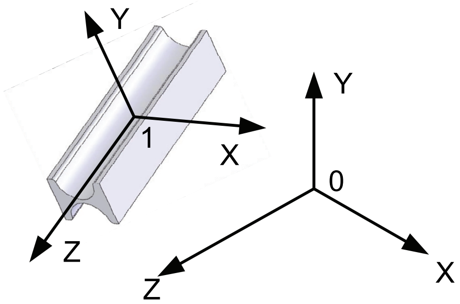

Figure 2.3: Flexure joint with local and global reference frames.

2.1.3 Task-Space Compliance Formulation

The procedure of finding the mechanism compliance is outlined for a general parallel flexure-based mechanism with ideal geometry. The model is then extended to include the influence of machining tolerances. Figure 2.4a shows schematic of a general mechanism that is a parallel connection of N limbs. Each limb is a serial connection of J joints. The joints in each limb are labeled alphabetically, and each limb labeled numerically, as indicated. The origin of the global reference frame is coincident with any point of interest on the mechanism platform.

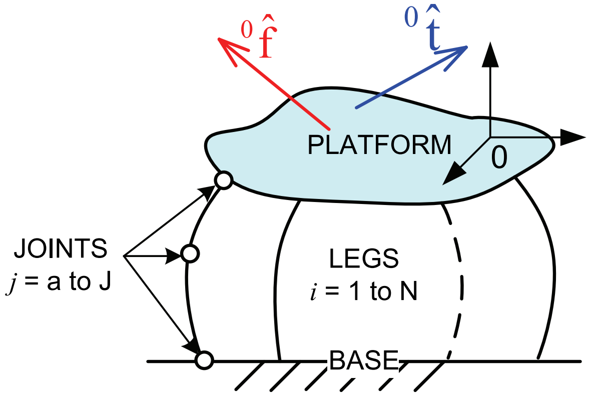

(a) General flexure mechanism

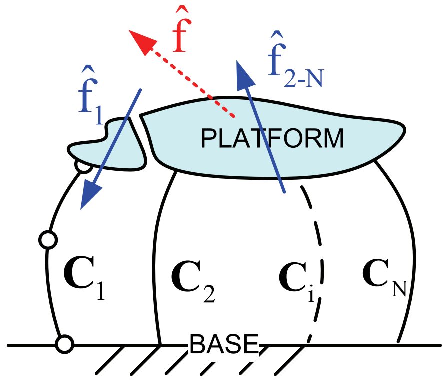

(b) Force distribution

Figure 2.4: Mechanism compliance analysis

Consider wrench $^0\hat{f}$ acting on the mechanism platform. The twist of motion of the platform $^0\hat{t}$ is then given by,

$$^0\hat{t} = {}^0\mathbf{C} \cdot {}^0\hat{f} \tag{2.12}$$

where, $^0\mathbf{C}$ is the mechanism task-space compliance. The mechanism can be considered to be made up of two limbs, limb 1 and an equivalent limb made up of limbs 2 to N joined together, such that, if ${}^0\hat{\mathrm{f}}_1$ is the wrench supported by limb 1, then the wrench supported by the equivalent limb 2-N is $\left({}^0\hat{\mathrm{f}} - {}^0\hat{\mathrm{f}}_1\right)$. This is shown in Figure 2.4b. The twist of each of these limbs is given by,

$$\begin{aligned} {}^0\hat{\mathrm{t}}_1 &= {}^0\mathbf{C}_1 \cdot {}^0\hat{\mathrm{f}}_1 \\ {}^0\hat{\mathrm{t}}_{2-\mathrm{N}} &= {}^0\mathbf{C}_{2-\mathrm{N}} \cdot \left({}^0\hat{\mathrm{f}} - {}^0\hat{\mathrm{f}}_1\right) \end{aligned} \tag{2.13}$$

where, ${}^0\mathbf{C}_1$ is the compliance matrix of limb 1, and ${}^0\mathbf{C}_{2-\mathrm{N}}$ represents the compliance of the equivalent 2-N limb. But the two chains are rigidly connected to each other in the mechanism, and are thus constrained to move together, i.e.,

$$ {}^0\hat{\mathrm{t}}_1 = {}^0\hat{\mathrm{t}}_{2-\mathrm{N}} = {}^0\hat{\mathrm{t}} \tag{2.14}$$

where, ${}^0\hat{\mathrm{t}}$ is the twist of the mechanism. From equations (2.13) and (2.14), the wrench supported by limb 1 is given by,

$$ {}^0\hat{\mathrm{f}}_1 = \left({}^0\mathbf{C}_1 + {}^0\mathbf{C}_{2-\mathrm{N}}\right)^{-1} \cdot {}^0\mathbf{C}_{2-\mathrm{N}} \cdot {}^0\hat{\mathrm{f}} \tag{2.15}$$

From equations (2.13), (2.14), and (2.15), it follows that,

$$\begin{aligned} {}^0\hat{\mathrm{t}} &= {}^0\hat{\mathrm{t}}_1 = {}^0\mathbf{C}_1 \cdot {}^0\hat{\mathrm{f}}_1 \\ &= {}^0\mathbf{C}_1 \cdot \left({}^0\mathbf{C}_1 + {}^0\mathbf{C}_{2-\mathrm{N}}\right)^{-1} \cdot {}^0\mathbf{C}_{2-\mathrm{N}} \cdot {}^0\hat{\mathrm{f}} \end{aligned} \tag{2.16}$$

Comparing equations (2.12) and (2.16), the expression for task space compliance of the mechanism is found as,

$$ {}^0\mathbf{C} = {}^0\mathbf{C}_1 \cdot \left({}^0\mathbf{C}_1 + {}^0\mathbf{C}_{2-\mathrm{N}}\right)^{-1} \cdot {}^0\mathbf{C}_{2-\mathrm{N}} \tag{2.17}$$

Since the equivalent 2-N limb is actually a parallel connection of limbs 2 to N, its compliance matrix ${}^0\mathbf{C}_{2-\mathrm{N}}$ can be found in exactly the same manner as for the entire mechanism. Equation (2.17) can be re-written to find ${}^{0}\mathbf{C}_{2-\mathrm{N}}$ as,

$$ {}^{0}\mathbf{C}_{2-\mathrm{N}} = {}^{0}\mathbf{C}_{2} \cdot \left({}^{0}\mathbf{C}_{2} + {}^{0}\mathbf{C}_{3-\mathrm{N}}\right)^{-1} \cdot {}^{0}\mathbf{C}_{3-\mathrm{N}} \tag{2.18} $$

where, ${}^{0}\mathbf{C}_{2}$ is the compliance matrix of limb 2, and ${}^{0}\mathbf{C}_{3-\mathrm{N}}$ represents the equivalent compliance of limbs 3 to N connected in parallel. Thus, by applying equation (2.17) iteratively, until the compliance matrices of all the limbs of the mechanism are included, the task-space compliance of the overall mechanism can be determined.

The compliance matrix of each individual limb of the mechanism is found simply by taking the sum of the compliance matrices of the joints in that limb, since the joints are in serial connection, i.e.

$$ {}^{0}\mathbf{C}_{\mathrm{i}} = \sum_{\mathrm{j}}^{\mathrm{J}} {}^{0}\mathbf{C}_{\mathrm{ij}}, \mathrm{i} = 1, \ldots, \mathrm{N} \tag{2.19} $$

The following observations about the model are noted.

- If the matrix $({}^{0}\mathbf{C}_{1} + {}^{0}\mathbf{C}_{2-\mathrm{N}})$ in equation (2.17) is rank deficient, the twist of motion of the mechanism is undefined. The wrenches supported by the two limbs of the mechanism 1 and 2-N in parallel cannot be resolved using equation (2.15), and are statically indeterminate. In other words, the mechanism is overconstrained, and does not move at all. Thus, the singularity condition of the matrix $({}^{0}\mathbf{C}_{1} + {}^{0}\mathbf{C}_{2-\mathrm{N}})$ can be used to determine whether the mechanism is overconstrained. It also leads to the conclusion that flexure mechanisms can never be overconstrained, since the flexure hinge is modeled as a 6 DOF joint, and its compliance matrix is full rank.

- It can be shown that under quasi-static operation, the wrenches supported by the chains determined from equation (2.15) satisfy the condition that the strain energy stored in the mechanism is always the minimum.

- The flexure mechanism compliance formulation is obtained using only the compliance matrices of the constituent flexure joints. This formulation is different from existing approaches [46, 47], which require inversion of the compliance matrices to find stiffness matrices to resolve the parallel connection between mechanism limbs. The advantage is important for selectively compliant mechanisms, where the joint compliance matrices could be ill-conditioned owing to very small compliance along the constrained directions. Repeated inversion of ill-conditioned matrices can potentially lead to numerical instabilities in the computation [48].

- The developed compliance model can be applied to any general flexure-based mechanisms with serial, parallel or hybrid topology.

2.1.4 Geometric Errors induced by Machining Tolerances

The machining process commonly used to fabricate flexure based mechanisms is wire electro discharge machining. A four-axis wire EDM machine is capable of creating complex profiles required to cut the notches of flexure joints of various shapes, such as circular, elliptical, hyperboloidal [16]. While several skim cuts can achieve extremely high surface finish from the machining, the positioning errors in the four-axis motion controller still leads to μm-scale dimensional tolerances [49]. A schematic of the four-axis wire EDM process is shown in Figure 2.5.

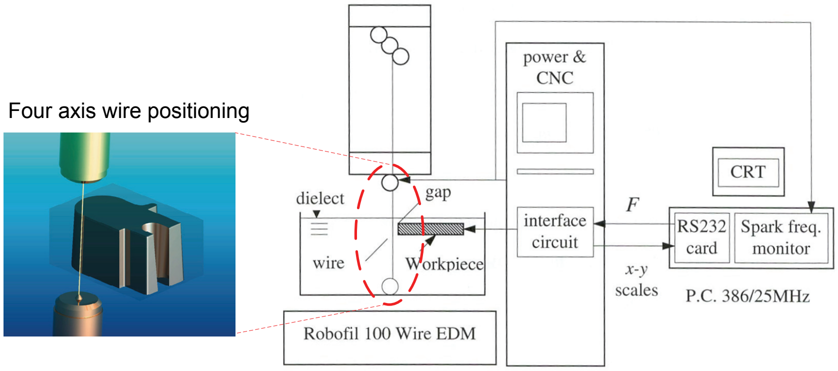

Figure 2.5: Wire EDM process schematic.

The tolerances in machining of the flexure joints have two-fold effect on the task-space compliance of the flexure-based mechanisms. Firstly, the tolerances in machining the geometrical parameters of the flexure joint, such as the minimum hinge thickness etc, can cause variation in the joint compliance values. Secondly, the tolerances can also introduce variation in the location and orientation of the joint screws. These two effects combine to perturb the compliance matrix of the mechanism, which in turn leads to undesirable parasitic motion of mechanism. In this research, the focus is on the geometry errors of joint screws due to machining tolerances.

Ryu [28] presents detailed modeling of the various errors in the flexure joint geometry induced by machining tolerances. Figure 2.6 shows the possible orientation and location errors in the joint screws. Due to the geometric errors, the spatial location of the flexure joint is displaced from its design value in the mechanism. If reference frame '1' represents the intended location/orientation of a flexure joint, and reference frame 'G' coincides with the actual joint, then the spatial displacement between the two reference frames is caused by the geometric errors. In the classical kinematics, this displacement is modeled using an adjoint matrix which operates on homogenous coordinates [50]. In spatial kinematics, the displacement is represented by a spatial transformation matrix [42], which for the geometric errors is given by,

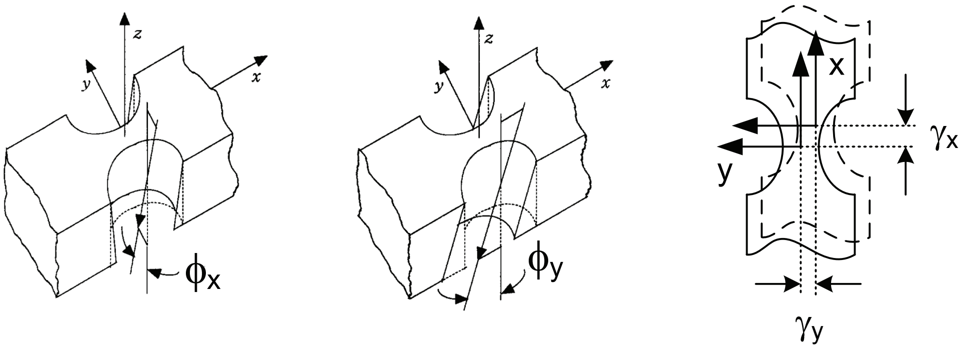

(a) Orientation errors (b) Location errors

Figure 2.6: Errors induced by machining tolerances in flexure joint axis geometry.

$$ {}^{1}_{\mathrm{G}}\mathbf{X} = \begin{bmatrix} \mathbf{R}(\boldsymbol{\phi}) & \mathbf{0} \\ (\boldsymbol{\gamma}\otimes)\cdot\mathbf{R}(\boldsymbol{\phi}) & \mathbf{R}(\boldsymbol{\phi}) \end{bmatrix} \tag{2.20} $$

Here, $\boldsymbol{\gamma} = \begin{bmatrix} \gamma_{\mathrm{x}} & \gamma_{\mathrm{y}} & \gamma_{\mathrm{z}} \end{bmatrix}^{\mathrm{T}}$ are the location errors, and $\boldsymbol{\phi} = \begin{bmatrix} \phi_{\mathrm{x}} & \phi_{\mathrm{y}} & \phi_{\mathrm{z}} \end{bmatrix}^{\mathrm{T}}$

are the orientation errors of the joint screws. Also, the sequence of rotation matrices in computing $\mathbf{R}\left(\boldsymbol{\phi}\right)$ is chosen as,

$$\mathbf{R} = \mathbf{R}\left(\phi_{\mathrm{X}}\right) \cdot \mathbf{R}\left(\phi_{\mathrm{Y}}\right) \cdot \mathbf{R}\left(\phi_{\mathrm{Z}}\right) \tag{2.21}$$

In the above analysis, the parameterization of the geometric errors in terms of the orientation and location perturbations implicitly assumes that the even after the perturbations, the flexure joint geometry is symmetrical. In other words, the two notches that constitute the flexure joint are displaced by the same parameters. Section 2.1.5 considers the case of asymmetrical flexure joint.

The representation of the flexure joint screws in the global reference frame ‘0’ can be obtained by applying the transformations in sequence, from frame ‘G’ to ‘1’, and then from frame ‘1’ to ‘0’. Thus,

$${}^{0}\hat{\$} = {}^{0}_{1}\mathbf{X} \cdot {}^{1}\hat{\$} = {}^{0}_{1}\mathbf{X} \cdot {}^{1}_{\mathrm{G}}\mathbf{X} \tag{2.22}$$

The representation of the joint compliance matrix in the global reference frame ‘0’ is then given by,

$${}^{0}\mathbf{C} = \left({}^{0}_{1}\mathbf{X} \cdot {}^{1}_{\mathrm{G}}\mathbf{X}\right) \cdot \mathbf{c} \cdot \left({}^{0}_{1}\mathbf{X} \cdot {}^{1}_{\mathrm{G}}\mathbf{X}\right)^{\mathrm{T}} \cdot \boldsymbol{\Delta} \tag{2.23}$$

The task-space compliance matrix of the mechanism is determined as before with this new joint screw expression.

By parameterizing the errors caused by machining tolerances, the statistical nature of the machining process variations can be captured by treating the geometric error parameters as random variables with zero mean Gaussian distribution. The standard deviations can be estimated from the angular and linear machining tolerance limits achievable from standard wire EDM machining process [49]. For example, with angular and linear machining tolerance limits of ±10mrad and ±100μm, respectively, the standard deviations of the orientation and location error parameters are equivalent to,

$$\sigma_\phi = 3\text{mrad},\ \sigma_\gamma = 33\mu\text{m} \tag{2.24}$$

2.1.5 Compliance Modeling of Asymmetrical Flexure Joints

In this section, the compliance modeling presented in Section 2.1.2 is extended to include asymmetrical flexure joint designs. Although the analysis and design tasks considered in this dissertation only assume symmetrical flexure joints, the following discussion is included for completeness. The flexure joint may be rendered asymmetrical either by virtue of design (see for example Figure 2.7a) or due to machining imperfections (see for example Figure 2.7b).

For an asymmetrical flexure joint it may not be possible to diagonalize the scalar compliance of the joint, since the center of compliance may no longer exist. The necessary and sufficient condition for the existence of center of compliance, where the rotational and translational scalar compliance values are maximally decoupled, is that the compliance matrix have three pairs of eigenscrews, with each pair consisting of coincident eigenscrews of equal and opposite pitch values [45]. In this case, the complete 6×6 compliance matrix has to be considered, with the elements of the matrix populated via finite

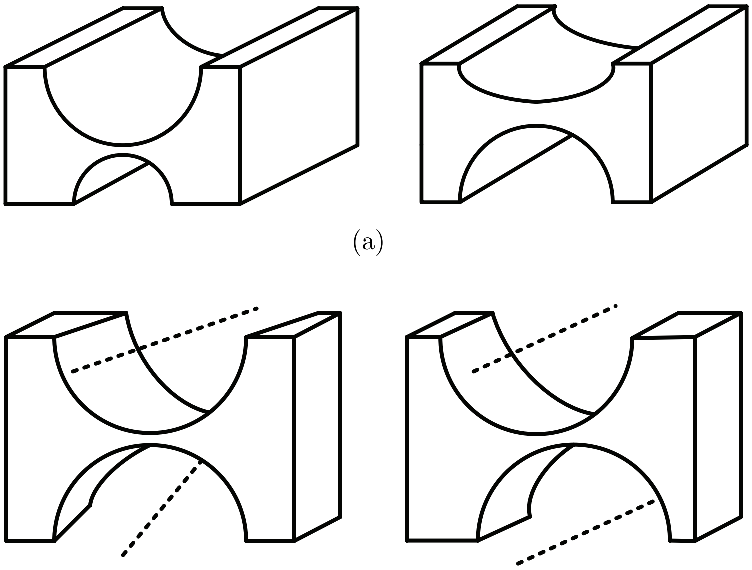

(a)

(b)

Figure 2.7: Asymmetry in flexure joint (a) by design, notches of different radii, or shapes(b) due to machining imperfections, notches perturbed differently in orientation or location.

element analysis. The procedure for identifying the joint compliance matrix in the mechanism reference frame is outlined next.

A suitable reference frame is selected for the joint to represent its local coordinate frame. Six linearly independent wrenches are chosen in the local reference frame. The twists of motion of the joint can be computed from the displacement results of a finite element analysis, for each of the six wrenches. The compliance matrix in the local reference frame can then be identified by,

$${}^{i}\mathbf{C} = {}^{i}\hat{\mathrm{t}} \cdot {}^{i}\hat{\mathrm{f}}^{-1} \tag{2.25}$$

where, ${}^{i}\hat{\mathrm{t}}$ are the six twists corresponding to the six wrenches ${}^{i}\hat{\mathrm{f}}$. By choosing

${}^{i}\hat{\mathrm{f}}$ to be an identity matrix, i.e., three forces aligned with the axes of the coordinate frame and passing through the origin, and three moments about the axes of the coordinate frame, the above computation is further simplified. As the 6×6 compliance matrix in equation (2.25) is symmetric and positive by definition, it is comprised of 21 independent scalar compliance terms, 6 diagonal terms consisting of pure rotational or translational compliance terms, and 15 off-diagonal terms that represent coupling effects. Knowing the spatial transformation between the local joint frame and the global mechanism frame, the representation of the joint compliance in the global frame can be obtained as before.

To account for the statistical nature of the machining perturbations, a response surface method can be adopted. Huh [30] present an approach to capture the influence of parametric uncertainty on the performance of a precision positioning device using a combination of finite element based analysis and statistical experiment design. A similar method is discussed here. By regarding the geometric errors due to machining imperfections as Gaussian random variables, an experiment design based on D-optimal selection [51] can be created. Specifically, for N independent random variables, a total of $(\mathrm{N}+1)\cdot(\mathrm{N}+2)/2$ experimental points are identified using the D-optimal selection method. Using the finite element approach presented above, the values of the 21 compliance matrix terms are determined for every point, from which the statistical moments of each term are calculated. Thus the uncertainty due to the geometric errors induced by machining imperfections are captured in the uncertainty of the scalar compliance of the flexure joint in its local reference frame.

2.1.6 Model Validation: One DOF Flexure Mechanisms

As a validation of the compliance modeling approach, the numerical results for twist of motion obtained from the model is compared with those obtained from finite element analysis. Two flexure-based mechanisms that are commercially available as part of precision positioning systems are used to demonstrate the comparison. A one rotational DOF mechanism (the classical four-bar mechanism) used in imprint lithography tool [1], and a one translational DOF mechanism used in atomic force microscopes sample scanners [7] are the candidate mechanisms. The comparison aims to establish the fact that, with known flexure mechanism geometry, flexure joint compliance properties, and external wrench acting on the mechanism, the model accurately determines the spatial motion of the flexure mechanism, with and without any machining tolerance induced geometric errors. Thus two analysis scenarios are presented for both the candidate mechanisms, firstly, with zero geometric error parameters, and secondly, with a randomly chosen configuration for the error parameters to reflect the statistical nature of the machining process. The details of the analyses for the two candidate mechanisms are described next.

Four-bar Flexure Mechanism

The key parameters defining the mechanism geometry are shown in Figure 2.8a. The global reference frame is located at the instantaneous center of the four bar mechanism. The mechanism is contained in the XY plane. The spatial transformation matrices to locate each of the four flexure joints in the global reference frame are obtained from the geometry parameters. For example, for joint '11',

$$
\begin{aligned}
{}^{0}\boldsymbol{\rho}_{11} &= \begin{bmatrix} -0.11 & 0.04 & 0 \end{bmatrix}^{\mathrm{T}}, && (2.26)\\
{}^{0}\mathbf{R}_{11} &= \begin{bmatrix} \cos(\theta_{\mathrm{z}}) & \sin(\theta_{\mathrm{z}}) & 0 \\ -\sin(\theta_{\mathrm{z}}) & \cos(\theta_{\mathrm{z}}) & 0 \\ 0 & 0 & 1 \end{bmatrix}, \text{with } \theta_{\mathrm{z}} = -10^{\mathrm{o}} && (2.27)
\end{aligned}
$$

Substituting these parameters in equation (2.10), yields the spatial transformation for the joint '11'.

The FE model that is used for comparison is shown in Figure 2.8b. The links of the mechanism are modeled as rigid connections between the flexure joints. The nodal displacement results from the FE analysis are used to calculate the twist of motion of the mechanism [32, 52]. A portion of the coupler link is included in the FE model for this purpose. The FE analysis was carried out using COSMOSWorks 2004 edition linear solver.

A pure force is used to actuate the flexure mechanism, to simulate the actual loading the mechanism would undergo in an application. The force acts along the Y-axis, and is located at a distance of 25mm from the origin along the positive X axis. With a magnitude of 1N, the effective wrench acting on

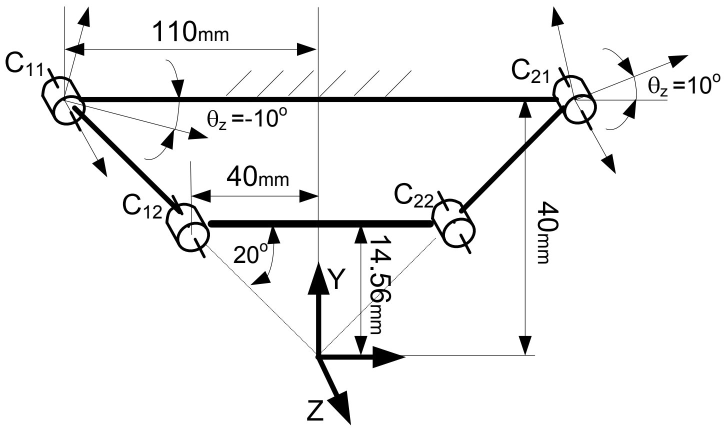

(a) Schematic

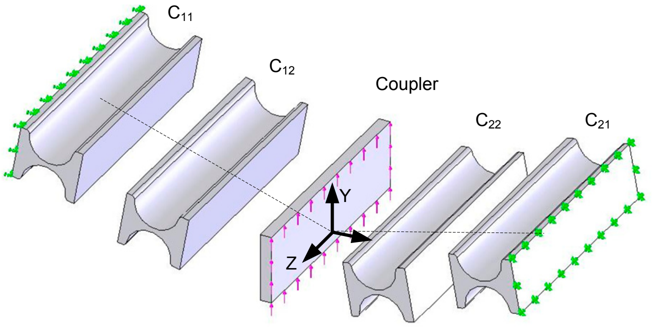

(b) FE Model

Figure 2.8: Four-bar mechanism analysis.

the mechanism is,

$$\hat{\mathrm{f}} = \left[\begin{array}{cccccc} 0 & 1 & 0 & 0 & 0 & 0.025 \end{array}\right]^{\mathrm{T}} \tag{2.28}$$

A right circular notch hinge flexure joint, shown schematically in Figure 2.9, is used as the flexure element in the mechanism. Table 2.1a lists the main geometric and material parameters of the joint. The scalar rotational and translational compliance parameters of the joint are determined by FE analysis [53], and are listed in Table 2.1b.

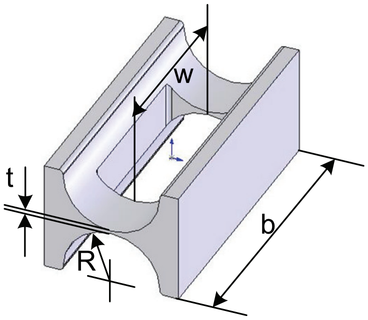

Figure 2.9: Right circular notch hinge flexure joint geometry.

Table 2.1: Right circular joint properties

(a) Joint properties

Parameter	Value
R	9.0mm
t	0.5mm
b	50.0mm
w	30.0mm
E	69GPa

(b) Joint scalar compliance

Parameter	Value	
cx	6.031×10^{-4}	rad/Nm
cy	2.169×10^{-5}	
cz	1.559×10^{-1}	
cX	8.811×10^{-9}	m/N
cY	2.453×10^{-7}	
cZ	3.945×10^{-8}	

Table 2.2 shows the values of the twist parameters obtained from the analytical compliance model and FE analysis, for both the zero error and the random error configuration cases. The results indicate that the error in estimation of the mechanism motion using the compliance model is less than 5%, for both the error configurations.

Table 2.2: Comparison of twist from model and FE analysis for four-bar flexure mechanism

Twist parameter	Zero Error		Random Error	
	FEA	Model	FEA	Model
$\mathbf{w}$	9.412E-5	0.0	2.163E-2	2.203E-2
	-3.608E-5	0.0	3.775E-3	3.615E-3
	1.0	1.0	9.998E-1	9.998E-1
$\boldsymbol{\rho}$ [m]	-2.058E-4	-1.954E-4	-3.287E-4	-3.506E-4
	4.174E-5	4.094E-5	6.808E-5	7.691E-5
	-5.045E-7	0.0	6.182E-5	7.448E-6
h [nm/mrad]	-2.038	0.0	-555.16	-578.3
θ [mrad]	7.004E-1	6.977E-1	6.444E-1	6.487E-1

The twist of motion of the four-bar mechanism in the ideal case of zero errors is a zero pitch screw (line vector) located at the instantaneous center of the four-bar mechanism, indicating pure rotational degree of freedom. In the presence of geometric errors, the location, orientation and pitch of the twist are all perturbed. The finite pitch associated with the twist causes translation along the twist axis that is proportional to the rotation. Thus, in the presence of geometric errors, the purely rotational motion of the four-bar mechanism changes to screw motion.

One DOF Translation Stage

The key parameters defining the mechanism geometry are shown in Figure 2.10. The mechanism is contained in the XY plane, with the origin of the reference frame located at the center of the mechanism platform. Y-axis is the direction of linear travel of the mechanism platform. The mechanism is decomposed into four symmetrical chains, each of which is further broken down into the inner and the outer chains for computation of the spatial compliance matrix from the individual flexure joint compliance. The links and the flexure joints are labeled as shown in the figure.

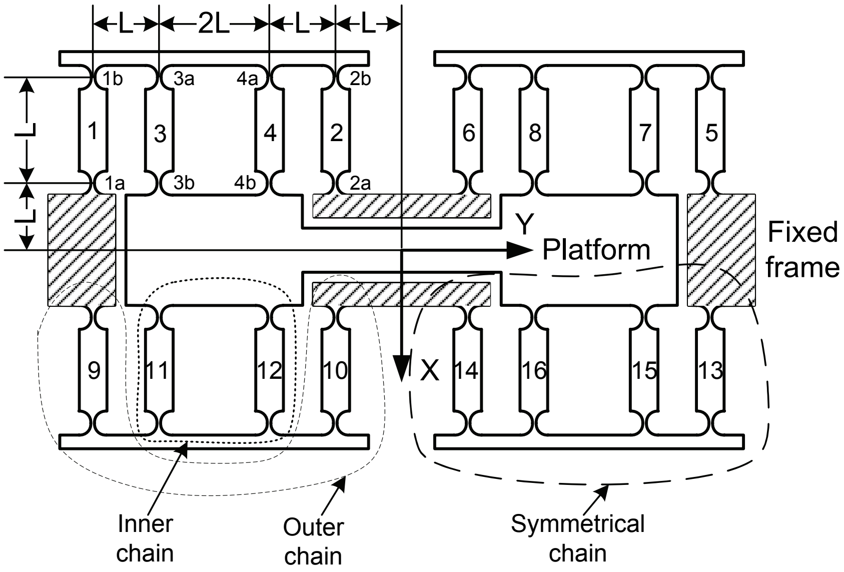

Figure 2.10: One DOF translation stage schematic.

The spatial transformation matrices required to locate each of the flexure joints in the mechanism reference frame are determined from the mechanism geometry. For example, for joint ‘1a’,

$$ {}^{0}\boldsymbol{\rho}_{1\mathrm{a}} = \begin{bmatrix} -\mathrm{L} & -5\mathrm{L} & 0 \end{bmatrix}^{\mathrm{T}} \tag{2.29} $$

$$ {}^{0}\mathbf{R}_{1\mathrm{a}} = \mathbf{I}_{3\times 3} \tag{2.30} $$

where, L is chosen to be 50mm. Substituting these into equation 2.10 yields the spatial transformation for the joint '1a'.

The wrench used to actuate the translation stage is a pure force of magnitude 10 N acting along the Y-axis, and located at the origin of the reference frame, i.e.,

$$\hat{\mathrm{f}} = \left[\begin{array}{cccccc} 0 & 10 & 0 & 0 & 0 & 0 \end{array}\right]^{\mathrm{T}} \tag{2.31}$$

The magnitude is chosen high enough to sufficiently excite the mechanism. The flexure joint parameters are chosen identical to those from the four-bar mechanism, and are listed in Tables 2.1a and 2.1b. The nodal displacement of seven reference points[1] on the mechanism platform from FE analysis are compared to the displacement of the corresponding points obtained from the model. The comparison is made for two cases of geometric error configurations, zero error and a random sample of error parameters. Table 2.3a lists the displacement of the chosen reference points for the zero error case, while Table 2.3b shows the values for the random error case. The FE analysis is carried out using COSMOSWorks Linear Solver.

As seen from the zero geometric error case, the mechanism responds to the external wrench by translating along the Y axis, which is the direction of its degree-of-freedom. The distance traveled is predicted by the model to within 3% of the FE analysis result. The FE analysis results of the random geometric error case clearly indicate the significant motion along the constrained directions of X and Z axes. Again, the displacement calculated by the model

---

[1] Displacement of at least six points is required to estimate the twist of motion [52].

Table 2.3: One DOF translation stage motion analysis

(a) Zero error

	Model			FE analysis		
Point	X [m]	Y [m]	Z [m]	X [m]	Y [m]	Z [m]
1	2.62E-25	4.88E-05	0	-3.63E-11	4.74E-05	1.85E-11
2	2.62E-25	4.88E-05	0	-3.48E-11	4.74E-05	1.85E-11
3	-2.62E-25	4.88E-05	0	7.78E-11	4.74E-05	1.81E-11
4	-2.62E-25	4.88E-05	0	-7.61E-11	4.74E-05	1.88E-11
5	-2.62E-25	4.88E-05	0	-7.77E-11	4.74E-05	1.88E-11
6	2.62E-25	4.88E-05	0	3.98E-11	4.74E-05	1.84E-11
7	2.62E-25	4.88E-05	0	3.81E-11	4.74E-05	1.84E-11

(b) Random error configuration

	Model			FE analysis		
Point	X [m]	Y [m]	Z [m]	X [m]	Y [m]	Z [m]
1	-1.05E-08	4.32E-05	-4.06E-08	-9.79E-09	4.21E-05	-4.11E-08
2	1.03E-08	4.32E-05	-4.06E-08	9.77E-09	4.21E-05	-4.11E-08
3	-1.05E-08	4.32E-05	-3.93E-08	-9.68E-09	4.21E-05	-4.04E-08
4	1.03E-08	4.32E-05	-3.52E-08	9.72E-09	4.21E-05	-3.62E-08
5	-1.05E-08	4.32E-05	-3.52E-08	-9.83E-09	4.21E-05	-3.62E-08
6	1.03E-08	4.32E-05	-3.64E-08	9.84E-09	4.21E-05	-3.78E-08
7	-1.05E-08	4.32E-05	-3.64E-08	-9.71E-09	4.21E-05	-3.78E-08

is within 5% of the FE results, which confirms that the compliance model reliably accounts for the geometric errors.

The twist of motion of the mechanism platform determined from the model is found to be an infinite pitch screw oriented along the Y axis, in the case of zero geometric errors. This indicates the mechanism exhibits pure translation along the applied force. However, in the presence of geometric errors, the twist becomes a finite pitch screw, as shown in equation (2.32).

$$\hat{\mathrm{t}} = \begin{bmatrix} -1.24\times10^{-7} \\ -4.16\times10^{-7} \\ -9.56\times10^{-10} \\ -7.47\times10^{-11} \\ 4.32\times10^{-5} \\ -3.78\times10^{-8} \end{bmatrix} \quad \begin{array}{c} \mathrm{w} = \begin{bmatrix} -0.286 \\ -0.958 \\ -0.002 \end{bmatrix}, \ \boldsymbol{\rho} = \begin{bmatrix} 0.303 \\ -0.025 \\ -28.48 \end{bmatrix} \mathrm{m} \\ \theta = 4.34\times10^{-7}\mathrm{rad}, \ \mathrm{h} = -95.45\mathrm{m/rad} \end{array} \tag{2.32}$$

Remarks

From the results of model validation analysis for the two candidate flexure mechanisms, it is evident that, given the topology of a flexure mechanism, the location and orientation of the joints, the scalar compliance values of the joints, the external wrench acting on the mechanism, and information about the machining process variations, the model determines the complete spatial motion characteristics of the flexure mechanisms, from which the parasitic motion can be ascertained. Further, the good correspondence between the displacement results from the model with that of the FE analysis for the random geometric error configuration indicates that the developed model systematically accounts for the machining tolerances with sufficient accuracy.

2.2 Parasitic Motion Classification and Quantification

The screw systems based compliance model for mechanism motion analysis reveals an important geometric insight into the parasitic motion problem of flexure mechanisms that is not available from models that only yield the numerical values of spatial displacement (for example, FE analysis). Flexure-based compliant mechanisms with one or more degrees of freedom are designed such that the motion along each DOF is simple, i.e., pure rotation or translation. For example, the previously discussed one DOF rotation or translation mechanism, a two rotational DOF orientation mechanism with tip-tilt motion (equivalent to a universal joint), a planar XY translation stage, and so on. The twist of motion of each of these mechanisms belongs to special screw system whose order equals the degrees of freedom of the mechanisms [31]. This is clear from the spatial motion analysis with zero geometric errors of both the four-bar mechanism and the translation stage. The zero pitch twist of the four-bar flexure mechanism, and the infinite pitch twist of the one DOF translation stage, are both special cases of the general first order screw system with a finite pitch twist. This is shown in Figure 2.11. Geometric errors induced in the flexure joints by machining process variations perturb the special screw systems, and the actual twist of motion of the mechanisms belongs to the corresponding general screw systems.

The significance of the above geometric insight is that the overall undesirable motion of flexure mechanisms can be decoupled into two parts. The parasitic motion that results only from the differences between the special screw system of the ideal mechanism and the corresponding general screw system of the actual mechanism characterizes the intrinsic error motion that is coupled to the degrees of freedom of the mechanism. Any other error motion is extrinsic to the mechanism that can be corrected by well-known calibration techniques [40, 41, 54].

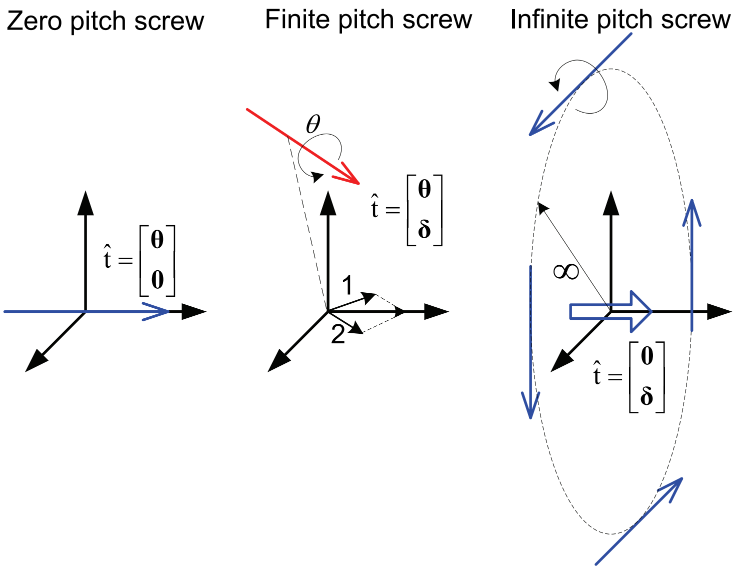

Figure 2.11: Special and general screw systems of first order.

Consider a general finite pitch twist of motion, shown in Figure 2.11, given by the expression,

$$\hat{\mathrm{t}} = \begin{bmatrix} \boldsymbol{\theta} \\ \boldsymbol{\delta} \end{bmatrix} = \hat{\$} \cdot \theta = \begin{bmatrix} \mathbf{w} \\ \underbrace{\boldsymbol{\rho} \otimes \mathbf{w}}_{1} + \underbrace{\mathrm{h} \cdot \mathbf{w}}_{2} \end{bmatrix} \cdot \theta \tag{2.33}$$

Here, θ is the rotation about the screw axis, and $\boldsymbol{\delta}$ is the translation of the origin of the reference frame, and is the sum of two orthogonal vectors, terms 1 and 2. The term 1 represents translation due to the offset in the location of the twist axis from the origin, while term 2 represents the translation along the axis of rotation due to the finite pitch of the twist.

In the case of one DOF rotational four-bar mechanism, if the twist axis coincides with the origin of the reference frame, then both the terms are reduced to zero. However, the analysis revealed that, in the presence of geometric errors, not only did the twist of motion not pass through the origin, it also had a finite pitch of twist. The offset in the twist axis from the origin can be minimized by calibration, but the finite pitch, which represents the translation of the mechanism along the rotation axis, is intrinsically tied to the mechanism motion, and cannot be corrected apriori.

For the one DOF translation stage, the ideal twist of motion (infinite pitch screw, or zero pitch screw at infinity), is associated with zero rotation. Either a very small but finite pitch twist located far away from the mechanism (term 1 dominates in the translation), or a very high pitch twist located around the origin of the reference frame (term 2 dominates in the translation) could result due to perturbations in the mechanism geometry caused by machining tolerances. In both the cases, the rotation θ associated with the twist defines the parasitic motion that cannot be corrected via calibration.

The metrics to quantify the intrinsic parasitic motion of both rotation and translation DOF flexure mechanisms can be defined as,

$$\mathrm{m_R} = \frac{\boldsymbol{\theta} \bullet \boldsymbol{\delta}}{\boldsymbol{\theta} \bullet \boldsymbol{\theta}} \rightarrow \text{ translation per unit rotation (pitch)} \tag{2.34}$$

and,

$$\mathrm{m_T} = \frac{\boldsymbol{\theta} \bullet \boldsymbol{\delta}}{\boldsymbol{\delta} \bullet \boldsymbol{\delta}} \rightarrow \text{ rotation per unit translation} \tag{2.35}$$

respectively. An important property of the above metrics is that they are independent of the magnitude of the external wrench acting on the mechanism.

Based on the spatial kinetostatic model of the flexure mechanism compliance, the metrics of intrinsic parasitic motion can be represented in functional form as,

$$\mathrm{m} = fn\left(\hat{\$}, \mathbf{c}, \boldsymbol{\epsilon}, \hat{\$}_{\mathrm{f}}\right) \tag{2.36}$$

Here, $\hat{\$}$ includes all the screws defining the geometry of the flexure joints, and $\hat{\$}_{\mathrm{f}}$ the unit screw representing the geometry of the external wrench acting on the mechanism, both defined in the mechanism reference frame. The joint compliance is represented by $\mathbf{c}$, a diagonal matrix with the rotational and translation scalar compliance values on the principal diagonal. The term $\boldsymbol{\epsilon}$ represents the random geometry errors induced by machining process variations, and includes both the location and orientation errors at each of the mechanism joint.

The function itself is uniquely defined for every flexure mechanism based on the mechanism topology, and is statistical in nature due to the random geometric error terms. The function is made deterministic by sampling the geometric error terms which are assumed to belong to Gaussian distributions. The model can be used to propagate the variations of the error terms to determine the variation of the metric via Monte Carlo simulations, as shown schematically in Figure 2.12. The standard deviation of the metric can then be used as the measure of precision capability of the flexure mechanism, with a smaller value denoting a better precision capability.

The results of Monte Carlo simulation with 10^4 samples for the four-bar flexure mechanism with the mechanism geometry, external wrench, geometric

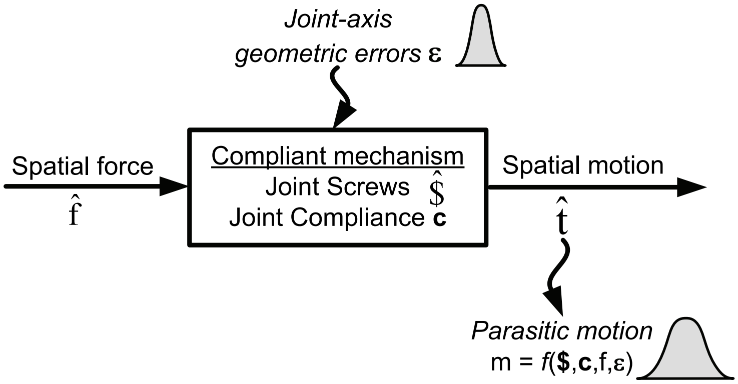

Figure 2.12: Block diagram representation of parasitic motion analysis.

errors, and scalar joint compliance identical to those from the model validation analysis, is shown in Figure 2.13. The distribution of pitch of twist is overlaid with the Gaussian distribution curve. The standard deviation of pitch is found to be 340nm/mrad, and the kurtosis of 2.97 indicates that the distribution is nearly Gaussian. The precision capability of the four-bar mechanism can be

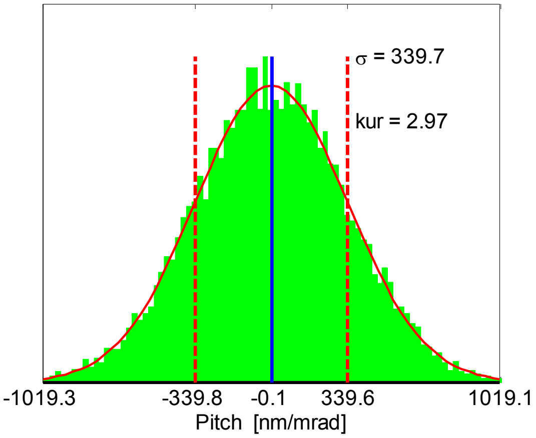

Figure 2.13: Pitch distribution of four-bar flexure mechanism.

interpreted as follows. The four-bar mechanism is used in imprint lithography application to align the template to the substrate. If the mechanism is required to rotate 20μrad then, due to the finite pitch of twist of the mechanism, the intrinsic parasitic translation has a standard deviation of $340 \times 0.02 = 6.8$nm. If the imprinting application can tolerate a maximum relative translation between template and substrate of ±5nm, then the probability that a four-bar mechanism fabricated with machining tolerances of equation (2.24) will have the desired precision capability is only 0.538.[2] In other words, the 'scrap' in a 'build-test-select' scheme to realize the mechanism will be 46%.

The result of a similar Monte Carlo analysis for the one DOF translational stage is shown in Figure 2.14. The distribution is found to be Gaussian (kurtosis = 3.01), with a standard deviation of 7.6375 mrad/m. If the mechanism is required to have a translation range of 50 μm (at the center of the platform), the standard deviation of the rotation of the platform is then $\left(7.638 \times 10^{-3}\right) \times \left(50 \times 10^{-6}\right) \approx 0.4\mu$rad. At any point on the platform at a distance of 50mm from the center of the platform, the out-of-plane linear displacement will have a standard deviation of $(5 \times 10^{-2}) \times (0.4 \times 10^{-6}) = 20$nm. If the mechanism is required to achieve out-of-plane displacement of at most ±25nm, then the probability that a mechanism fabricated with tolerance limits specified in equation (2.24) meets the specifications is about 0.81. In other words, up to 19% scrap can be expected in a 'build-test-select' scheme to

---

[2] Area under the Gaussian distribution curve with zero mean, and $\sigma = 6.8$nm, between +5nm and -5 nm.

realize the mechanism.

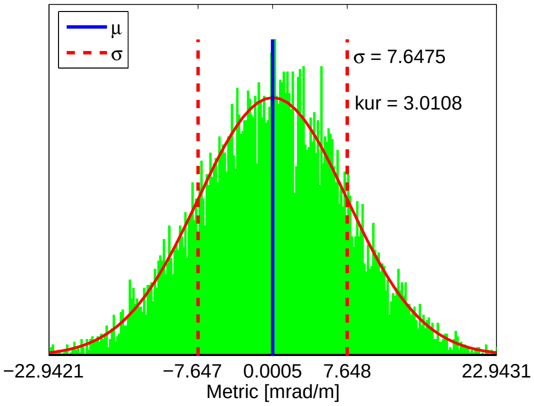

Figure 2.14: Metric distribution of one DOF translation stage.

2.3 Extension to Two DOF Flexure Mechanisms

The parasitic motion analysis is extended to two DOF flexure mechanisms to demonstrate the general applicability of the developed compliance modeling approach. A two rotational DOF tip-tilt flexure mechanism which is employed in optics for tilting mirrors/lenses, in imprint lithography for template-substrate alignment [18], and a two translational DOF planar XY stage used in a number of precision applications are chosen as the candidate mechanisms.

Two DOF Tip-Tilt Mechanism

Figure 2.15 shows the mechanism, along with the schematic of one limb. The four limbs of the mechanism exhibit reflective symmetry about the XZ and the YZ planes. The unique arrangement of the flexure joints enables the mechanism platform to rotate with respect to the base about two axes located in the XY plane and intersecting orthogonally at the origin of the reference frame. This is equivalent to a classical universal joint. The screw system of motion of the ideal mechanism is a special second order system, called a planar pencil [31].

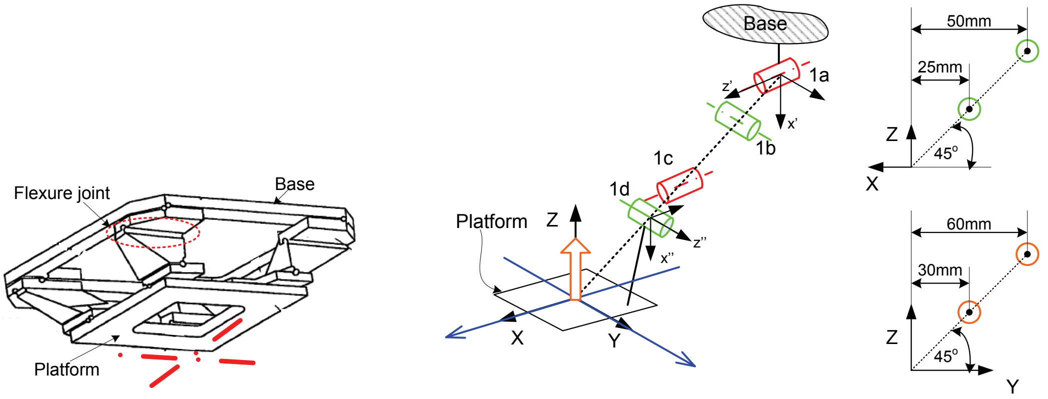

(a) Tip-tilt mechanism (b) Schematic of one limb

Figure 2.15: Two rotational DOF tip-tilt mechanism analysis.

With the geometry shown, the location and orientation of the joint '1a' in the mechanism reference frame is given by,

$$
\begin{aligned}
{}^{0}\boldsymbol{\rho}_{1\mathrm{a}} &= \begin{bmatrix} -\mathrm{a} & \mathrm{a} & \mathrm{a} \end{bmatrix}^{\mathrm{T}}, \text{ with a} = 60\text{mm} && (2.37)\\
{}^{0}\mathbf{R}_{1\mathrm{a}} &= \begin{bmatrix} 0 & 0 & 1 \\ 0 & 1 & 0 \\ -1 & 0 & 0 \end{bmatrix} && (2.38)
\end{aligned}
$$

For a pure force acting on the platform along the Z axis with an offset along the X axis, the twist of motion of the platform is a zero pitch screw, passing through the origin, aligned along the Y axis. The geometric errors induce perturbation in the special screw system, and the resulting screw system of the actual mechanism is the general second order screw system called the cylindroid. The pitch of twist of motion of the actual mechanism is a finite value between the maximum and minimum values corresponding to the two principal screws of the cylindroid. The parameters of twist of motion of the mechanism with two different geometric error cases, namely zero errors and random error configuration, are shown in Table 2.4.

Table 2.4: Twist of motion of two DOF tip-tilt mechanism

Twist parameter	Zero Error	Random Error
$\mathbf{w}$	0	1.49×10^{-3}
	1	9.99×10^{-1}
	0	-3.48×10^{-3}
$\boldsymbol{\rho}$ [m]	-1.46×10^{-3}	-1.55×10^{-3}
	3.58×10^{-18}	6.97×10^{-7}
	4.49×10^{-4}	4.62×10^{-4}
h [nm/mrad]	1.62×10^{-10}	-10.13
θ [mrad]	1.99×10^{-4}	1.98×10^{-4}

The results of Monte Carlo simulations with 10^4 samples of the geometric error parameters is shown in Figure 2.16. The flexure joint compliance are taken from Table 2.1. The precision capability of the mechanism is found to be 7.381nm/mrad.

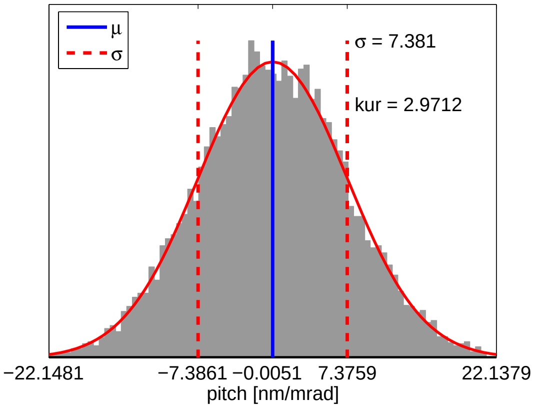

Figure 2.16: Pitch distribution of two rotation DOF tip-tilt mechanism.

Two Translation DOF XY Stage

Figure 2.17a shows the schematic of the two DOF translation stage. The mechanism platform is located in the XY plane of the global reference frame and can translate about the X and the Y axis independently. The symmetry of the mechanism ensures that the effective compliance about the two translation axes are equal. Figure 2.17b shows the main geometric parameters of the mechanism, including the link length L (=50mm) and orientation $\alpha\left(=45^0\right)$. Further, the parameters L*, L' and L" are given by,

$$\mathrm{L}^* = 0.8 \cdot \mathrm{L}, \mathrm{L}' = \mathrm{L} \cdot \sin\left(\alpha\right), \mathrm{L}'' = 0.2 \cdot \mathrm{L} \tag{2.39}$$

The geometry of joint ‘11’ used to locate the joint screws in the global

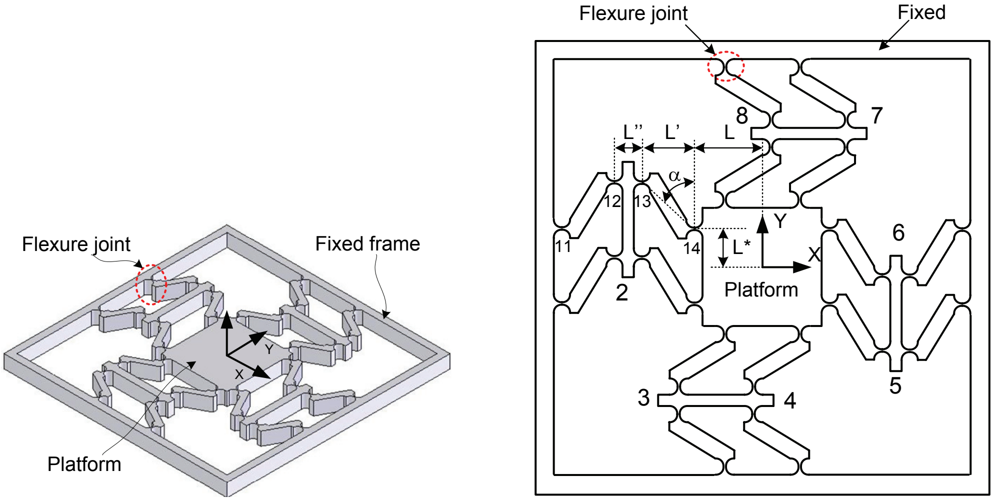

(a) XY Stage (b) Geometry of mechanism

Figure 2.17: Two translation DOF XY stage analysis.

reference frame is,

$$^{0}\boldsymbol{\rho}_{11} = \begin{bmatrix} -(\mathrm{L} + 2 \cdot \mathrm{L}' \cdot \sin(\alpha) + \mathrm{L}'') & \mathrm{L}^{*} & 0 \end{bmatrix}^{\mathrm{T}} \tag{2.40}$$

$$^{0}\mathbf{R}_{11} = \mathbf{I}_{3\times 3} \tag{2.41}$$

The wrench used in the simulations is a pure force of magnitude 1 N acting in the XY plane, at an angle of 45^{0} to the Y-axis, and located at the origin of the reference frame, i.e.,

$$\hat{\mathrm{f}} = \begin{bmatrix} 0.707 & 0.707 & 0 & 0 & 0 & 0 \end{bmatrix}^{\mathrm{T}} \tag{2.42}$$

Table 2.5 lists the parameters of the twist of motion with zero geometric errors and random error configuration cases. In the zero error case, the twist is an infinite pitch screw, while in case of the random geometric error, the twist is a finite pitch screw, offset from the origin, and is associated with a finite rotation.

Table 2.5: Twist of motion of two DOF translation stage

Twist parameter	Zero Error	Random Error
w	0.707	-0.906
	0.707	0.420
	0	0.058
$\boldsymbol{\rho}$ [m]	0	-1.261
	0	1.264
	0	-28.991
h [m/rad]	∞	-10.637
θ [rad]	0	4.247×10^{-8}

The standard deviation of the metric of intrinsic parasitic motion determined from Monte Carlo simulation with 10^4 iterations is found to be 15.505 mrad/m (see Figure 2.18). This implies that, for a translation range of 50μm (at the origin of the mechanism reference frame), the standard deviation of the platform rotation is $\left(15.505 \times 10^{-3}\right) \times \left(50 \times 10^{-6}\right) \approx 0.775\mu$rad, which corresponds to an out-of-plane linear displacement of $(5 \times 10^{-2}) \times (0.76 \times 10^{-6}) =$ 38nm at any point on the platform at a distance of 50mm from the origin. With a desired precision capability of ±25nm out-of-plane displacement, only 49% of the two DOF mechanisms fabricated with tolerance limits specified in equation (2.24) will satisfy the requirement, thus generating up to 51% scrap in a 'build-test-select' scheme to realize the mechanism.

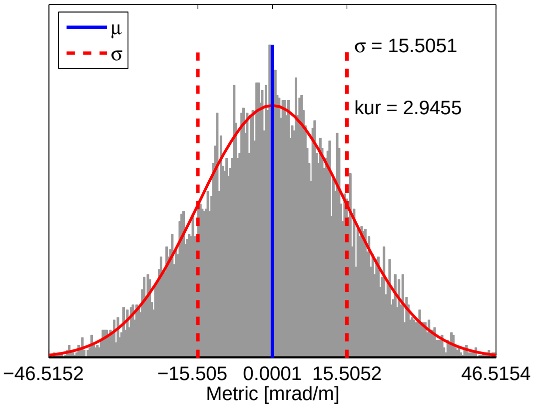

Figure 2.18: Metric distribution of two translation DOF XY stage.

Chapter 3

Experimental Determination of Parasitic Motion

This chapter presents the details of experimental determination of intrinsic parasitic motion of a flexure-based one DOF rotational mechanism that is part of an imprint lithography equipment [1]. The focus of the experiments was to determine the pitch of twist of the screw motion of the mechanism platform. Development of the experimental setup serves two purposes. Firstly, it demonstrates the nano-scale precision metrology capability required to measure the parasitic motion of flexure mechanisms. The ability to measure parasitic motion opens up possibilities like feedback control to improve the flexure mechanisms precision capability by active compensation. Secondly, the setup forms a preliminary prototype of a modular 'quality control' station, that can be used to compare the precision capabilities of general flexure mechanisms. This can find application in a manufacturing setup, to measure-test-select the best performing candidate from a batch of precision flexure mechanisms. The one DOF rotational mechanism is chosen as the candidate for parasitic motion measurement because the sample mechanism and the resources for the test setup development were made readily available by Molecular Imprints, Inc.

As parasitic motion is inherently spatial in nature, its measurement requires determination of complete spatial motion of the mechanism. A brief introduction to spatial motion measurement is presented first. The simplified model used for parasitic motion measurement in one DOF rotational mechanism is then discussed. The design considerations and the development of the test-setup are then presented. Experimental procedure is outlined, and the results of parasitic motion measurement are summarized.

3.1 Spatial Motion Measurement

Determination of the location and orientation of end effectors in robots, moving platforms in motion guiding systems, is crucial for the purposes of calibration, and closed-loop operation. While indirect metrology (for example, using joint position encoders) can be a cost-effective means of spatial motion measurement, in the field of precision engineering, direct metrology is preferred for high accuracy and precision [10]. Non-contact measurement schemes using optical (laser interferometry, diffraction grating), capacitive or inductive sensors can detect relative motion with nano-scale precision [55]. Finding the complete spatial motion of a body requires at least six linearly independent displacement measurements. Slocum [56] presents a six DOF sensing device based on impedance sensors. Barriere et al [57] discuss a CCD-based optical six axis position sensor. Fan et al [58] describe a six-axis measurement setup using laser interferometry. The mechanics of six-axis metrology to determine complete spatial motion is briefly discussed here.

3.1.1 Six-axis Metrology

Finding the complete spatial motion of a body amounts to determining the twist of motion associated with it. Figure 3.1 shows schematic of a general mechanism with its platform undergoing spatial motion. If the corresponding twist of motion is represented in the platform reference frame as,

$$ {}^{\mathrm{P}}\hat{\mathrm{t}} = \begin{bmatrix} \boldsymbol{\theta} \\ \boldsymbol{\delta} \end{bmatrix} = \begin{bmatrix} \mathbf{w} \\ \boldsymbol{\rho} \otimes \mathbf{w} + \mathrm{h} \cdot \mathbf{w} \end{bmatrix} \cdot \theta \tag{3.1} $$

then, in order to determine the six terms associated with the twist, namely, three rotation and three translation terms, six independent displacement measurements are required.

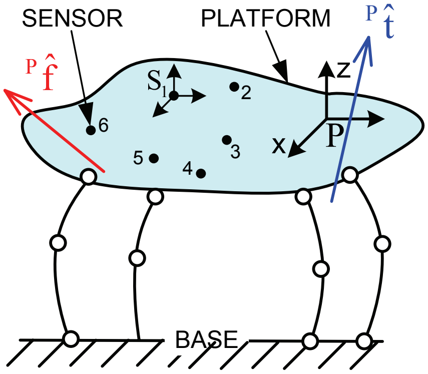

Figure 3.1: Six-axis metrology schematic.

Let ${}^{\mathrm{P}}\hat{\mathrm{S}}_{\mathrm{i}}$ represents a line vector defined in the platform reference frame, located at the sensor ‘i’ and directed along its measurement axis. Let the linear displacement recorded by the sensor be $\mathrm{d_i}$. Then, the six sensor readings $\mathbf{d}$

are related to the twist of motion by the expression,

$$\mathbf{d} = \mathbf{J}_{\mathrm{s}}^{\mathrm{T}} \cdot \mathbf{\Delta} \cdot {}^{\mathrm{P}}\hat{\mathrm{t}} \tag{3.2}$$

where, $\mathbf{\Delta}$ is the 6×6 permutation matrix defined in equation (2.3), and $\mathbf{J}_{\mathrm{s}}$ is the Jacobian matrix, consisting of the six sensor line vectors, i.e.,

$$\mathbf{J}_{\mathrm{s}} = \left[\begin{array}{ccc} {}^{\mathrm{P}}\hat{\mathrm{S}}_1 & \cdots & {}^{\mathrm{P}}\hat{\mathrm{S}}_6 \end{array} \right]_{6\times 6} \tag{3.3}$$

The interpretation of equation (3.2) is as follows. Spatial vectors ${}^{\mathrm{P}}\hat{\mathrm{S}}_{\mathrm{i}}$ are unit screws, and if they are used to represent a unit force acting on the platform, then the reciprocal product ${}^{\mathrm{P}}\hat{\mathrm{S}}_{\mathrm{i}}^{\mathrm{T}} \cdot \mathbf{\Delta} \cdot {}^{\mathrm{P}}\hat{\mathrm{t}}$ yields the work done by the spatial motion of the platform against the unit force. The work is also equal to the product of magnitude of force and resultant displacement. With unit force, the work corresponds to the scalar linear displacement recorded by the sensor d_{i}.

The twist of motion is then given by,

$${}^{\mathrm{P}}\hat{\mathrm{t}} = \mathbf{\Delta} \cdot \left(\mathbf{J}_{\mathrm{s}}^{\mathrm{T}}\right)^{-1} \cdot \mathbf{d} \tag{3.4}$$

If the Jacobian is singular, that is if the six displacement measurements are not linearly independent, the twist of motion cannot be determined. The most commonly adopted method to obtain six linearly independent measurements is to mount the sensors in a corner-cube scheme or 3-2-1 scheme [23], where three sensors are mounted on one plane, two on an orthogonal plane, and the last one on a mutually orthogonal plane.

In the event of more than six sensors, the pseudo-inverse of the Jacobian can be used to obtain the best estimate of the twist in a least-squared error sense as,

$$^{\mathrm{P}}\hat{\mathrm{t}} = \mathbf{\Delta} \cdot \left(\mathbf{J}_{\mathrm{s}} \cdot \mathbf{J}_{\mathrm{s}}^{\mathrm{T}}\right)^{-1} \cdot \mathbf{J}_{\mathrm{s}} \cdot \mathbf{d} \tag{3.5}$$

The implementation of six-axis sensing requiring six sensors can become very expensive. For example, a parallel-plate capacitive sensor with 10 nm resolution costs between 3000$ and 5000$, with laser interferometric techniques costing even more. If only the intrinsic parasitic motion characterization of flexure mechanisms is required, the six-axis sensing may not be necessary. A simplified parasitic motion measurement scheme for the particular case of the one DOF rotational mechanism is discussed next.

3.1.2 Simplified 3-axis Metrology

Ideally, the platform one DOF rotational mechanism rotates about the mechanism instantaneous center. Machining tolerances induce the mechanism to exhibit general screw motion instead. The intrinsic parasitic motion of the one DOF rotational mechanism is captured by the pitch associated with the screw motion. With the general twist representation of equation (3.1), the pitch of twist given by,

$$\begin{aligned} \mathrm{h} &= \frac{\boldsymbol{\theta} \bullet \boldsymbol{\delta}}{\boldsymbol{\theta} \bullet \boldsymbol{\theta}} \\ &= \frac{\theta_{\mathrm{x}}}{\|\boldsymbol{\theta}\|} \cdot \delta_{\mathrm{x}} + \frac{\theta_{\mathrm{y}}}{\|\boldsymbol{\theta}\|} \cdot \delta_{\mathrm{y}} + \frac{\theta_{\mathrm{z}}}{\|\boldsymbol{\theta}\|} \cdot \delta_{\mathrm{z}} \end{aligned} \tag{3.6}$$

Since θ_x and θ_y are very small in comparison to θ_z, the contribution to the pitch from perturbation of the orientation and location of the twist of motion from their ideal values can be considered negligible. Then, an approximation for the pitch of twist can be made as,

$$h = \frac{\delta_z}{\theta_z} \tag{3.7}$$

Thus, measuring only the significant rotation and the associated out-of-plane translation of the mechanism platform enables estimation of the pitch. This 3-axis sensing is used for characterizing intrinsic parasitic motion of the one DOF rotational flexure mechanism. Figure 3.2 shows the 3-axis metrology scheme.

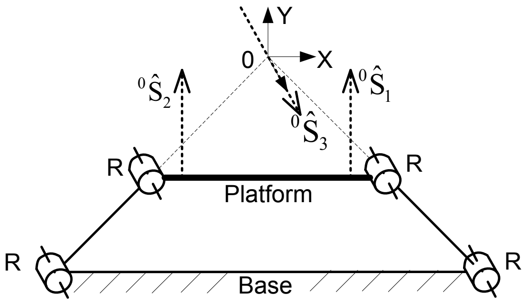

Figure 3.2: Three-axis metrology for one DOF rotational mechanism.

The origin of the reference frame is located on the instantaneous axis and in the plane of the mechanism. The figure shows the locations of the three sensors with respect to the reference frame '0'. Sensors 1 and 2 are aligned with the Y axis and offset from the origin along the X axis. Sensor 3 is aligned with the Z axis and located at the origin. Thus, the line vectors defining the three sensors are,

$$\begin{aligned} {}^{0}\hat{\mathrm{S}}_1 &= \left[\begin{array}{cccccc} 0 & 1 & 0 & -\mathrm{z}_1 & 0 & \mathrm{x}_1 \end{array} \right]^{\mathrm{T}} \\ {}^{0}\hat{\mathrm{S}}_2 &= \left[\begin{array}{cccccc} 0 & 1 & 0 & -\mathrm{z}_2 & 0 & \mathrm{x}_2 \end{array} \right]^{\mathrm{T}} \\ {}^{0}\hat{\mathrm{S}}_3 &= \left[\begin{array}{cccccc} 0 & 0 & 1 & 0 & 0 & 0 \end{array} \right]^{\mathrm{T}} \end{aligned} \tag{3.8}$$

Using equation (3.2), the relative displacements measured by the three sensors are given by,

$$\begin{aligned} \mathrm{d}_1 = \; & {}^{0}\hat{\mathrm{S}}_1^{\mathrm{T}} \cdot \boldsymbol{\Delta} \cdot {}^{0}\hat{\mathrm{t}} && = -\mathrm{z}_1 \cdot \theta_{\mathrm{x}} + \mathrm{x}_1 \cdot \theta_{\mathrm{z}} + \delta_{\mathrm{y}} \\ \mathrm{d}_2 = \; & {}^{0}\hat{\mathrm{S}}_2^{\mathrm{T}} \cdot \boldsymbol{\Delta} \cdot {}^{0}\hat{\mathrm{t}} && = -\mathrm{z}_2 \cdot \theta_{\mathrm{x}} + \mathrm{x}_2 \cdot \theta_{\mathrm{z}} + \delta_{\mathrm{y}} \\ \mathrm{d}_3 = \; & {}^{0}\hat{\mathrm{S}}_3^{\mathrm{T}} \cdot \boldsymbol{\Delta} \cdot {}^{0}\hat{\mathrm{t}} && = \delta_{\mathrm{z}} \end{aligned} \tag{3.9}$$

Thus, by locating the two sensors 1 and 2 in the same XY plane, i.e., $\mathrm{z}_1 = \mathrm{z}_2$, yields,

$$\begin{aligned} \theta_{\mathrm{z}} &= \frac{\mathrm{d}_1 - \mathrm{d}_2}{\mathrm{x}_1 - \mathrm{x}_2} \\ \delta_{\mathrm{z}} &= \mathrm{d}_3 \end{aligned} \tag{3.10}$$

which when substituted back in equation (3.7) gives the approximate pitch estimate.

The following assumptions/requirements are implicit in the three axis metrology,

1. rotation about the X and Y axes is negligible,
2. the X and Z locations of sensors $\hat{\mathrm{S}}_1$ and $\hat{\mathrm{S}}_2$ are known and their measurement axes are aligned with the Y axis,
3. the measurement axis of sensor $\hat{\mathrm{S}}_3$ is aligned with the Z axis, and contains the origin of the reference frame.

If the assumptions are not satisfied in the test setup, errors build up in the pitch estimate. In the following section, the steps taken to capture these assumptions in the development of the test setup are discussed.

3.2 Test Setup Design

The design of an experimental test setup for parasitic motion characterization of the one DOF rotational flexure mechanism is described here. Figure 3.3 shows the candidate flexure mechanism with a few important dimensions shown to establish the scale of the setup. The test setup has three functional requirements, namely,

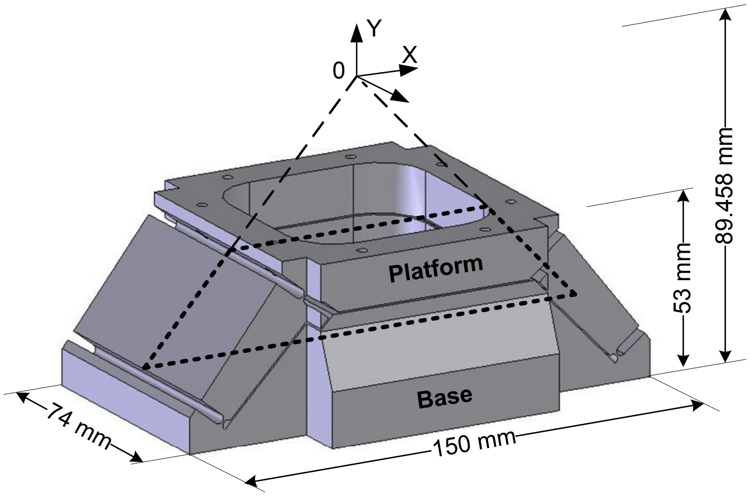

Figure 3.3: Candidate flexure mechanism with one rotation DOF.

- repeatably locate the mechanism and fix the mechanism base,

- locate (and orient) the sensors with respect to the mechanism at three defined locations on the platform,
- enable application of a defined moment to the mechanism platform.

Figure 3.4 shows the schematic of the complete test setup. The design pertaining to each of the three functions are presented next.

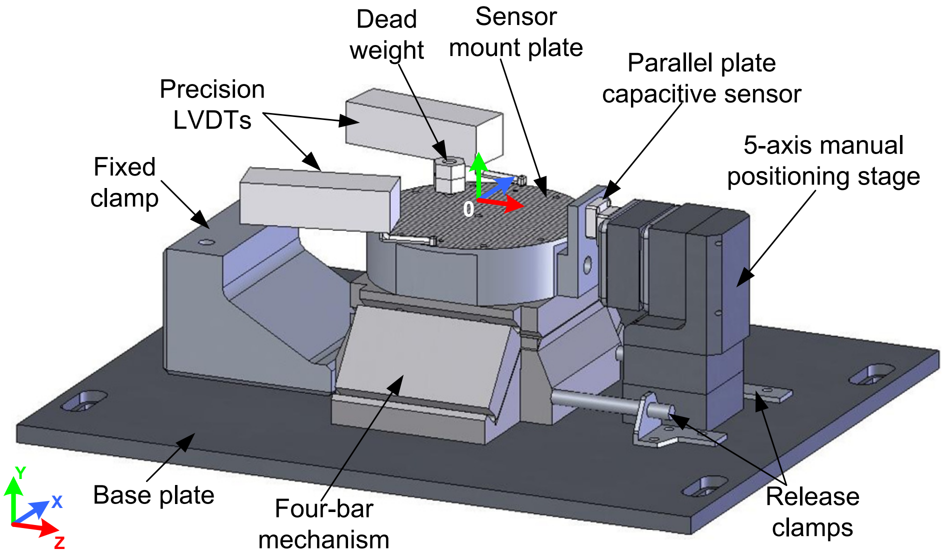

Figure 3.4: Test setup schematic.

3.2.1 Fixture Design

The flexure is made of aluminum alloy 6061 by wire EDM fabrication process. A base-plate also made of aluminum is used to provide the reference to mount and locate the flexure mechanism and sensors. The mechanism is located on the base-plate by means of a fixed block and a dowel pin. Two bistable quick-release clamps are used to apply the required clamping force. As the flexure mechanism is to be loaded by dead weights, very little clamping force is needed to fix the base on the base-plate. The quick-release clamps are adjustable, and care is taken to avoid undesirable loading the mechanism by excessive clamping forces. The base-plate itself is mounted onto a vibration isolation table.

3.2.2 Sensor setup

The candidate mechanism finds use in an imprint lithography machine, to align the silicon substrate and the imprint template. The template is mounted on the platform using a chuck such that, the template-substrate interface occurs at the instantaneous center of the one DOF rotational mechanism. Thus small angular misalignments between the template and the substrate are corrected without any translation at the interface, which is a critical requirement for the imprint lithography application. If the mechanism exhibits screw motion instead of pure rotation, then out-of-plane translation equal to the pitch of the screw times the angular rotation results at the template-substrate interface. The measurands, namely, the angular rotation and the out-of-plane translation of the platform, are typically of the order of micro-radians, and nanometers, respectively. The relative displacement sensors that are available for use in the test setup are listed in Table 3.1 along with relevant specifications.

The precision LVDTs are gage head type with stylus tips. They come

Table 3.1: List of sensors.

#	Type	Make	Range (Nom/Max)	Resolution
1	Capacitive	Physik Instrumente	50 μm / -	1.0 nm
2	LVDT	Precision Devices Inc.,	50 μm / 0.5 mm	0.1 μm

with mounting blocks, an amplifier and display units, and are popularly used as electronic height gages [59]. Two LVDTs are used as sensors $\hat{S}_1$ and $\hat{S}_2$ in the three-axis sensing scheme, as shown in Figure 3.4 (mounting blocks not shown). The differential configuration enables measurement of the angular rotation of the platform. An aluminum plate of diameter 96.5mm with a lapped surface (1mm thick annular ring at the periphery) is mounted on the mechanism platform and acts as the land for the LVDT styluses. The separation between the two LVDTs along the X axis, i.e., $x_1 - x_2$, is thus 96.5mm. The Z location of the two LVDT styluses are set to zero visually, using a scale mounted on the sensor mount plate, with a maximum error or 0.5mm. The styluses are aligned with the top of the sensor mount plate, thus eliminating any cosine errors in the readings, effectively aligning the measurement axis with the Y axis of the mechanism reference frame.

The parallel plate capacitive sensor is used to measure the out-of-plane translation of the mechanism. The target plate of the sensor is mounted on the sensor mount plate on the platform via a coupler plate to locate the sensor at the mechanism instantaneous center. The probe plate is mounted at the end of a 5-axis manual fine positioning stage. The other end of the positioning stage is clamped rigidly to the base-plate. The fine positioning stage is assembled by serial connection of three single DOF translation stages and a tip-tilt 2 DOF rotational stage. Each of the individual stages are made of aluminum thereby ensuring material match with both the sensor plate and the base-plate. Positioning is achieved by fine-pitch set screws, which can be locked in place. The 5-axis positioning is required to eliminate any offset and misalignment between the two parallel plates of the capacitive sensor. The PI sensor comes with signal conditioning amplifier and display unit. The feedback from the display unit is used to 'calibrate' the manual positioning stages to achieve desired positioning of the parallel plates, such that the measurement axis is aligned with the Z axis, and contains the origin of the reference frame.

The data from both the precision LVDTs and the capacitive sensors is recorded on a computer using a data acquisition program built in LabVIEW. Serial communcation is used to interface the sensor amplifiers output with the host PC. The LabVIEW program for each sensor is separately available from the manufacturer. The two programs were modified to run simultaneously, and additional data logging features were added. The sampling rate for the data acquisition is set at 1Hz. This was deemed sufficient as the entire experiment is carried out in a quasi-static manner.

3.2.3 Actuation setup

Voice-coil motors are popular actuators for precision applications [55], because they operate in non-contact mode, and exhibit linear force output with input excitation current. However, the driver amplifiers and additional flexure-based bearing mechanisms needed for their operation, add to the cost of the setup significantly. The use dead-weights for applying known forces is an attractive low-cost alternative [25]. In the case of the candidate flexure mechanism, dead weights can be used effectively to load the mechanism. A scale with graduations along two orthogonal axes is attached to the sensor mount plate on the platform. Three dowel pins on the sensor mount plate are used to locate the scale such that its origin is along the Y axis of the mechanism reference frame. The graduations are in increments of 2.5 mm. By locating a known mass on the scale, desired moments can be applied about the X and Z axes of the mechanism reference frame.

The moment about the X axis is used to compensate the moment due to the offset loading by the capacitive sensor coupler plate. This is needed to reduce the angular rotation of the mechanism platform about the X axis. The mass distribution of the sensor coupler plate and the sensor mount plate are determined using the SolidWorks CAD software. Given the mass of the dead weight, the required offset along the Z axis for placing the dead weight on the mechanism platform is determined. Table 3.2 lists the calculations for finding the location of the dead weight. The part numbers 1 and 2 correspond to the sensor mount plate and coupler plate, respectively. The known mass (92gm) is placed on the platform at a Z offset of -12.5mm, with the X offset varied to induce different moment about the Z axis, and thus different angular rotation of the mechanism.

Table 3.2: Loading calculations to compensate for undesirable moment about X axis

Part	Mass [kg]	X [mm]	Z [mm]	M_x [Nmm]
1	0.2730	0.22	-0.31	-0.832
2	0.0244	-0.18	49.91	11.9
Total (1+2)	0.2974	0.187	3.796	11.09
Applied	0.092	0	-12.5	-11.28

3.3 Experiments: Procedure and Results

Figure 3.5 shows the actual experimental setup. The setup is used to perform two experiments. Firstly, the effective scalar compliance of the one DOF rotational flexure mechanism about the instantaneous axis of rotation is estimated. This simple experiment is used as a calibration step before the second experiment to estimate the pitch of twist. The details of the two experiments are outlined, and the results are presented.

3.3.1 Compliance estimation

Procedure

In this experiment, the dead weight is manually placed on the mechanism platform at various locations along the X axis, and the readings of the two precision LVDTs are recorded with and without the load. The dead weight placement location x_W is varied from +1in to -1in in steps of 0.2in. The dead weight is placed on the platform at the chosen location, held in place for a period of time. It is then removed and after sensor signals stabilize, the process is repeated with the next location. The experiment is repeated for ascend-

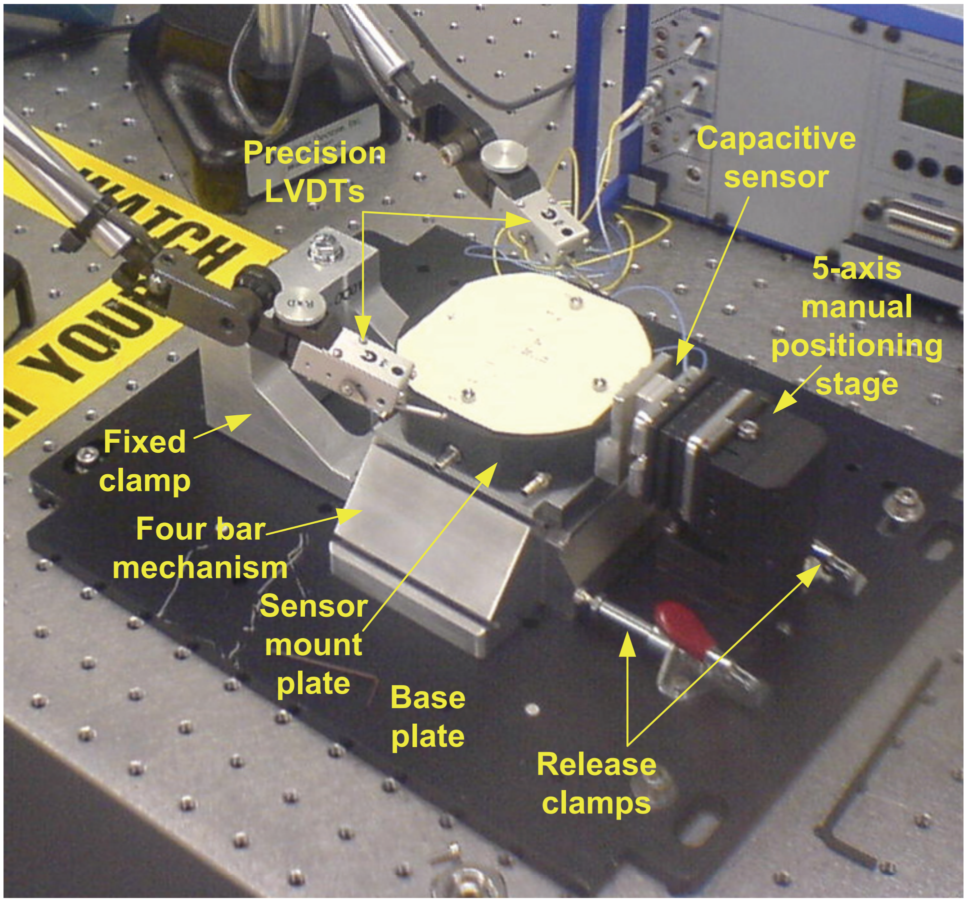

Figure 3.5: Experimental setup for parasitic motion estimation of one DOF rotational flexure mechanism.

ing values of X axis offsets, from -1in to +1in, to check for hysteresis in the mechanism motion. The moment applied about the instantaneous axis of the mechanism is calculated from the X axis offset x_W, and the known dead weight W as,

$$M_z = 9.81 * W * (-x_W) \tag{3.11}$$

The LVDT data is continuously acquired during the experiment with a sampling rate of 1Hz. The factory calibration settings for the LVDT amplifiers is used to obtain the displacement values from the sensor voltage output. The angle of rotation is determined from the LVDT readings d_1 and d_2 as follows. For every value of x_W, the sensor reading of the two LVDTs are recorded with load $\left(\mathrm{d}_\mathrm{i}^\mathrm{L}\right)$ and without load $\left(\mathrm{d}_\mathrm{i}^\mathrm{NL}\right)$ for a period of time. The data points are then averaged to yield $\left(\overline{\mathrm{d}}_\mathrm{i}^\mathrm{L}\right)$, and $\left(\overline{\mathrm{d}}_\mathrm{i}^\mathrm{NL}\right)$. The data averaging is required to account for the thermal drift in the sensor data. The difference between the average sensor reading for the loaded and unloaded cases represents the change in the LVDT readings for the applied load. Finally, the angle of rotation is calculated as,

$$\theta_\mathrm{z} = \frac{\left(\overline{\mathrm{d}}_1^\mathrm{L} - \overline{\mathrm{d}}_1^\mathrm{NL}\right) - \left(\overline{\mathrm{d}}_2^\mathrm{L} - \overline{\mathrm{d}}_2^\mathrm{NL}\right)}{(\mathrm{x}_1 - \mathrm{x}_2)} \tag{3.12}$$

Figure 3.6a shows a set of data points from the two LVDTs for the loaded and unloaded cases.

Results and discussion

Figure 3.6b shows the plot of the applied moment and the measured rotation angle for the mechanism. The effective scalar compliance, i.e., the ratio of the rotation angle of the mechanism and the applied moment, is determined from slope of the plot. The scalar compliance is also determined from finite element analysis of the flexure mechanism with identical loading condition, to verify the experiment. The results of the FE analysis are also shown on the same plot as the experiment. The rotational compliance is found to be 0.0023 rad/Nm, with a 20% error in comparison with the FE analysis.

The discrepancy in the estimation can be explained as follows. Due to geometric errors in the flexure mechanism, the instantaneous axis of rotation of the mechanism is no longer aligned with the Z axis of the mechanism reference frame. The FE analysis was carried out with zero geometric errors, and thus determines the compliance about the ideal mechanism rotation axis. The experimentally measured compliance value, on the other hand, is thus a combination of compliance about the instantaneous axis of rotation and the off axes values, which are designed to be less compliant. Thus the estimated compliance from FE analysis is higher than that measured from the experiment.

3.3.2 Pitch estimation

Procedure

In order to determine the pitch of twist, the out-of-plane translation of the flexure mechanism platform is measured using the capacitive sensor in addition to the rotation angle. The amplifier/display unit of the capacitive sensor handles the necessary signal conditioning, and the factory calibration setting determines the actual displacement at the sensor from the output voltage. Prior to the experiment, the probe plate of the sensor is manually aligned with the target plate, and the required nominal separation of 25μm between them is set using the 5-axis fine positioning stage. The steps to align the two sensor plates are illustrated in Figure 3.7. The displacement reading from the

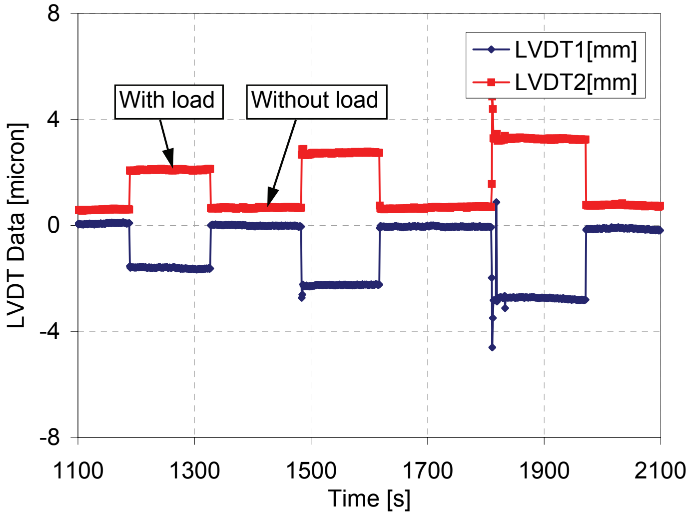

(a) LVDT Data

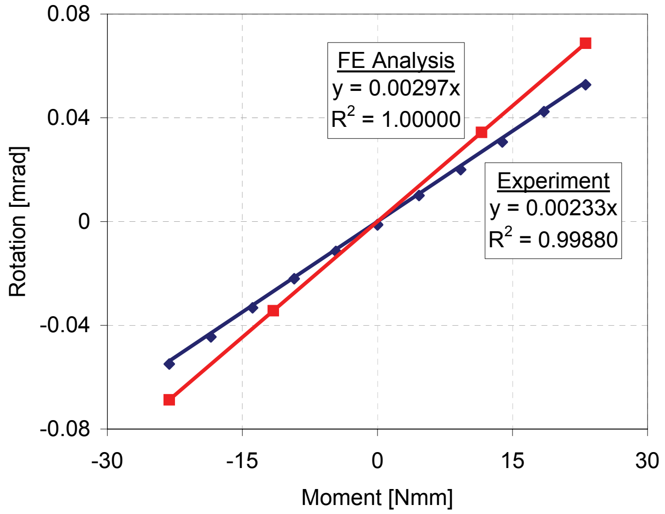

(b) Compliance

Figure 3.6: Scalar compliance determination

sensor display unit is used to guide the adjustment using the fact that, the final near parallel condition yields a displacement reading compared to the perturbed condition.

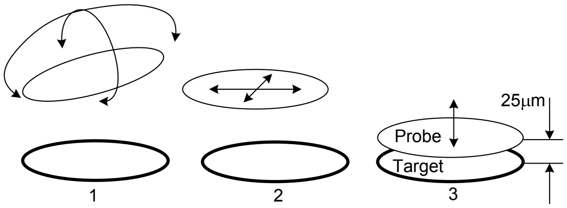

Figure 3.7: Capacitive sensor plates alignment steps.

Following the initial sensor setup, the experiment is carried out by repeatedly placing the dead weight on the mechanism platform at known locations and the readings from the LVDTs and the capacitive sensor are recorded. The X axis offset values for the dead weight placement are chosen as 1in, 0.5in, 0in, -0.5in, and -1in. The sensors data is recorded at 1Hz sampling rate.

The mechanism loading is done in the following manner. The weight is manually placed at +1in and -1in X axis offset alternatively. The weight is placed on the mechanism platform first at 1in X offset, and is held in place for a period of time until the sensor signals stabilize (typically 10 to 20s). The weight is withdrawn and the signals are allowed to stabilize in the unloaded condition. The weight is then placed at -1in X offset, and the process is repeated. The loading/unloading is then repeated for the 0.5in and -0.5in X offsets. This method was found to be better suited to capture the out-of-plane translation consistently with the angular rotation of the mechanism, in comparison with the steady increase/decrease of the offset values.

Figure 3.8 shows the displacement data obtained from the capacitive sensor and the LVDT over a period of 1200s. Only data from LVDT 1 is shown for clarity, since the data from LVDT 2 is similar to LVDT 1 except for the polarity. The data corresponds to loading the mechanism at ±1in X offset.

Data analysis

The sensor data shows a low frequency drift over the test period in addition to the mechanism displacement due to loading/unloading. To verify if the drift occurs due to temperature variations in the test environment, the sensor signals are logged along with the ambient temperature in the vicinity of the test setup for a period of 3 hours with the setup undisturbed (no load). Figure 3.9 shows the temperature along with the three sensor signals. The correlation coefficient between the sensor signals and the ambient temperature are listed in Table 3.3. From the data trends and the correlation coefficients, it can be concluded that there is a strong relationship between ambient temperature variation and the low frequency drift in the sensor data.

Table 3.3: Correlation coefficients

	Capacitive	LVDT1	LVDT2
Temperature	0.796	0.861	0.819

In order to extract the relative displacement information from the data,

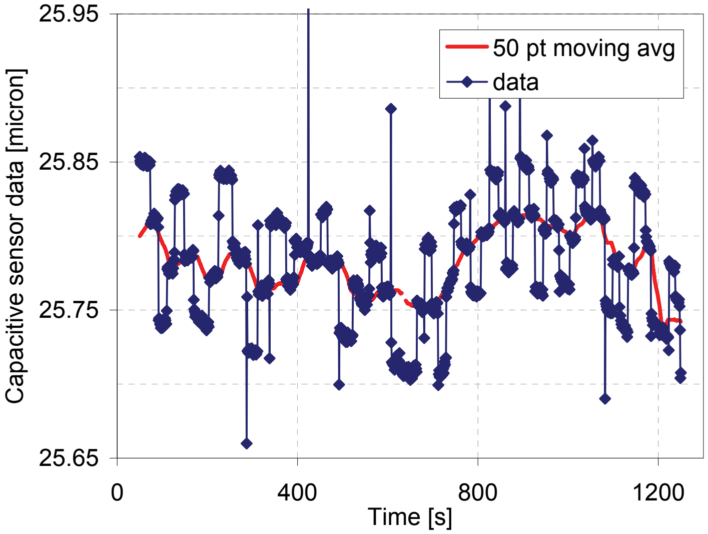

(a) Capacitive sensor data

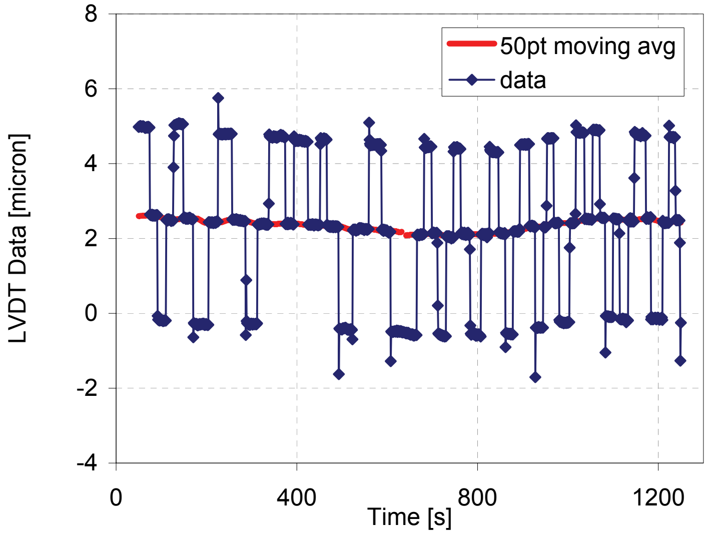

(b) LVDT data

Figure 3.8: Raw sensor data.

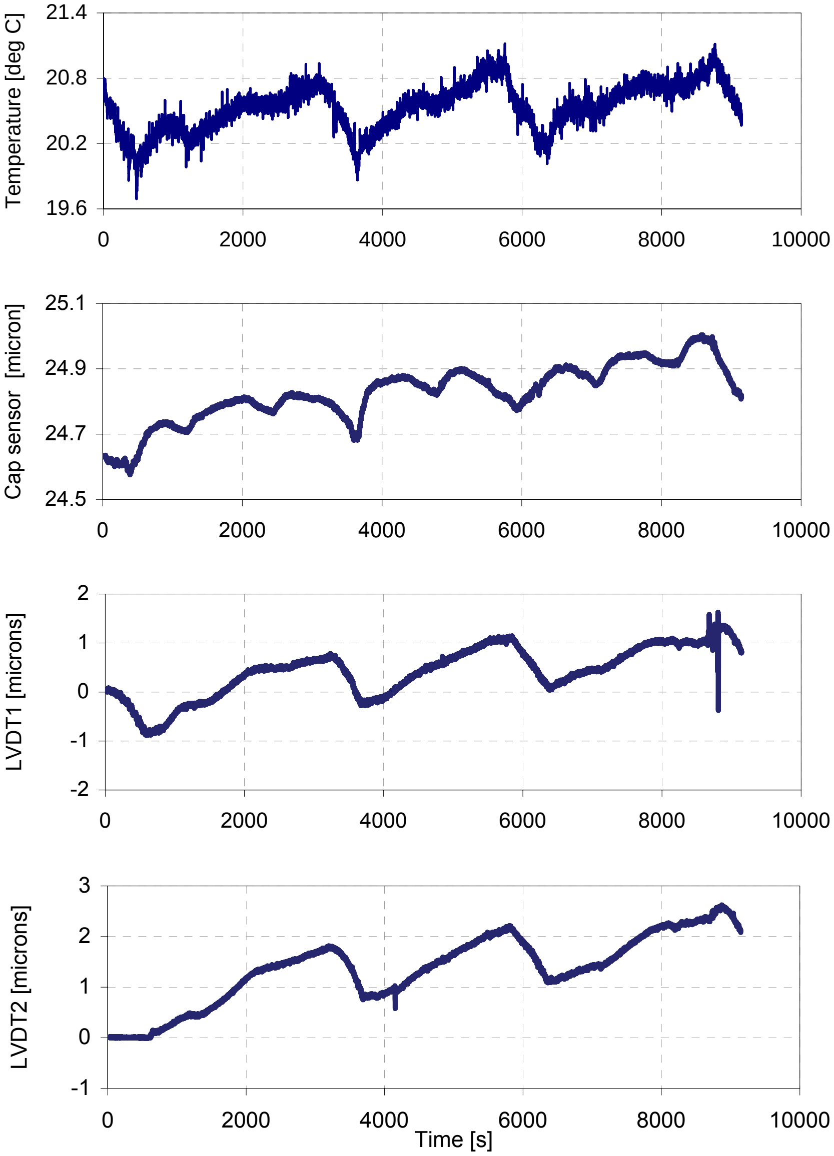

Figure 3.9: Log of sensor signals with temperature measurement for 3 hours.

the low frequency bias in the signals has to be removed. This is done by taking a 50 point moving average of the data points corresponding to the unloaded condition of the flexure mechanism to represent the reference for the sensor displacement data. By subtracting the reference from all the data points, the bias is eliminated. A portion of the unbiased data from the sensors is shown in Figure 3.10. The angular rotation and the out-of-plane translation of the mechanism platform about the Z axis, are determined from the unbiased sensor data, $\mathrm{d}_\mathrm{i}^\mathrm{u}$, using equation (3.10).

From Figure 3.10 of the unbiased data plot, it is clear that out-of-plane translation of the platform changes its sign with the mechanism angular rotation. That is, the mechanism platform translates in the negative Z axis direction for positive angular rotation about the Z axis, and vice-versa. This indicates that the one DOF rotational flexure mechanism is in fact executing screw motion with a finite negative pitch value.

Results and discussion

The plot of the out-of-plane translation versus the angle of rotation of the mechanism is shown in Figure 3.11 observed for both ±1in and ±0.5in X offset loading. A least square linear fit to the data is also shown. From equation (3.7), the slope of the line corresponds to the estimate of the magnitude of the pitch of twist of the flexure mechanism.

Although, the plot shows significant variation in the data along both the abscissa and the ordinate axes, the goodness of fit, as measured by the

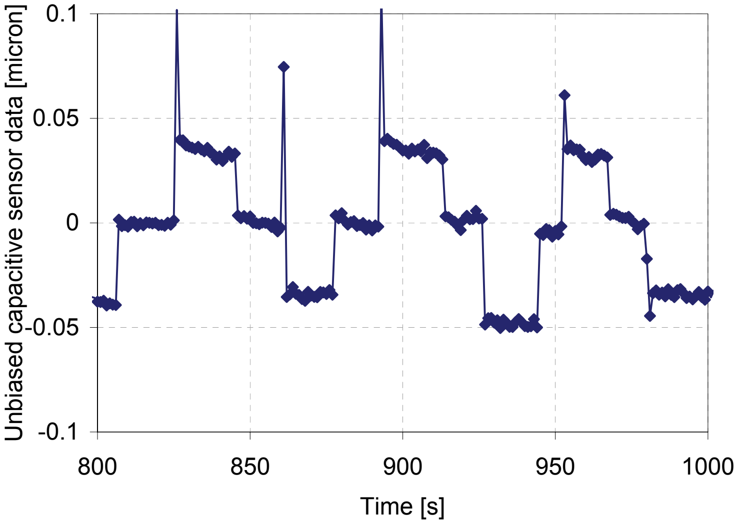

(a) Capacitive sensor data

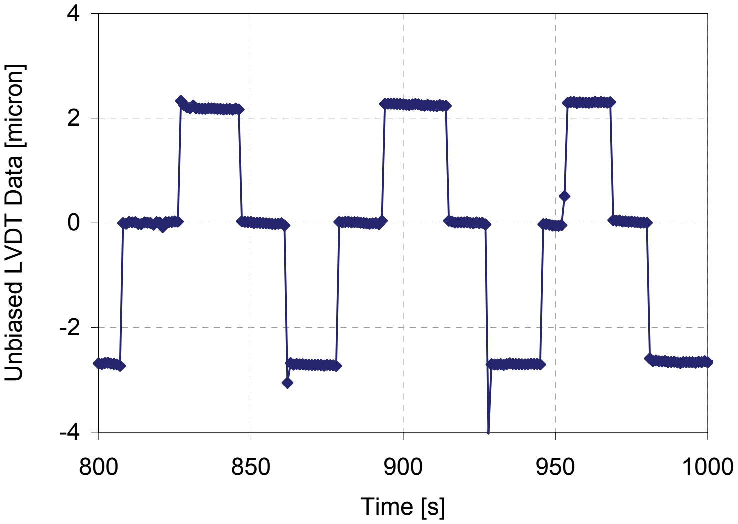

(b) LVDT data

Figure 3.10: Sensor data unbiased using the moving average value as reference.

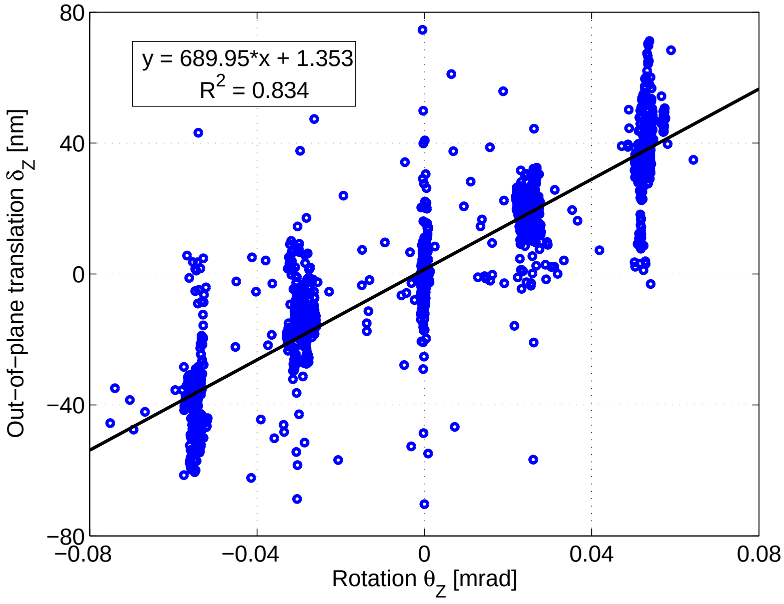

Figure 3.11: Pitch estimation results.

normalized sum of squares of the residuals, is found to be 0.834. This indicates that the linear fit accounts for 83% of the variation in the out-of-plane translation due to variation in the rotation of the mechanism [60].

The following comments about the sensor data are noted.

- The noise-floor of the capacitive sensor causes some uncertainty in the out-of-plane translation measurement. Although the resolution of the sensor is specified as 1nm, a noise level of ±5nm was observed in the sensor signal.
- The data points that lie completely outside the trend are the sensor data

associated with the dynamics of loading/unloading. As only the steady state loaded condition is of interest, these outliers are ignored.

- The uncertainty associated with locating the weight on the mechanism platform during repeated manual loading/unloading causes variation in both the rotation of the mechanism and the out-of-plane translation. Specifically, the location of the weight along X axis is known within ± 0.1in, as the scale used to locate the dead weight is graduated in increments of 0.2in. With a dead weight of 92.8gm, the variation in moment is $\pm 92.8 \times 10^{-3} * 9.81 * 0.1 * 25.4 \approx \pm 2$Nmm. Since the effective compliance is $\approx$2.5mrad/Nm (see Figure 3.6b), this amounts to a variation in the angular rotation of the flexure mechanism of $\approx \pm 5\mu$rad for each loaded condition, which can be seen in Figure 3.11.
- Finally, the drift in the sensor signals due to temperature variation when the mechanism is actuated by the dead weight leads to several data points along the ordinate axis for one point on the abscissa. The unbiased capacitive sensor data shows drifts up to 10nm (see Figure 3.10a) for each of the loaded condition of the mechanism. By averaging the capacitive sensor data points for each loading instance, one value for the out-of-plane translation of the mechanism corresponding to one value of angular rotation of the mechanism for each loading instance is obtained. The thermal drift in the LVDT signals is irrelevant, since they are used in a differential configuration, and only the difference in the signals is used in determining the angle of rotation.

Figure 3.12 shows the displacement data, with the variation on account of thermal drift accounted for by plotting the averaged value of the displacements for each instance of loading. A linear least square fit is shown with the goodness of fit according to the normalized residual norm of 93.3%. Also shown are the mean values of the out-of-plane translation and angular rotation for the chosen loading conditions (-1in through +1in X offset), along with the $\pm 3\sigma$ errors about both the axes. The pitch of twist of motion is estimated from the slope as -721.66nm/mrad. The 95% confidence intervals for the pitch estimate are determined from the F-test to be [-695, -749]nm/mrad.[1] Thus, the pitch of twist estimate is known with a precision of ±27nm/mrad.

Remarks

The experimental work offers several insights into the design of test setup and the measurement of parasitic motion of flexure mechanisms. Since the undesirable motion is in general several orders of magnitude smaller compared to the dominant motion of the flexure mechanisms, measuring it precisely is quite challenging. Special attention is required in designing the test

---

[1] The confidence intervals correspond to those values of the slope for which the sum of squared residuals are within 95% of the sum of squared residuals obtained from the best fit value, as determined from the F-distribution. For P parameters and N data points, the 'F' value for 95% confidence is found from the F-distribution (Excel function `finv(0.05,P,N-P)`). Then,

$$\mathrm{SS}_{95} = \mathrm{SS}_{\mathrm{LS}} * \left(1 + \mathrm{F} * \frac{\mathrm{P}}{\mathrm{N}-\mathrm{P}}\right)$$

where, $\mathrm{SS}_{\mathrm{LS}}$ and SS_{95} are the sum of squared residuals from the best fit value, and from the 95% confidence interval values. The confidence intervals are back-calculated from SS_{95}.

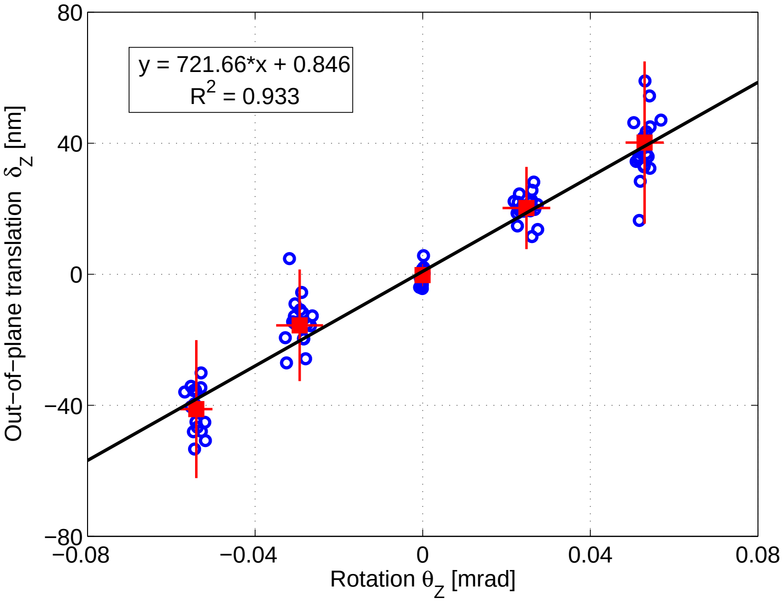

Figure 3.12: Pitch estimation results: smoothed data.

setup with the aim of minimizing the variation in the measured data. In the test setup developed in this work, the principal sources of variation in the experimental data are the actuation scheme, and the thermal variations. Improving the repeatability in the mechanism actuation can be accomplished by developing an automated loading scheme with controlled force, and constrained location. In the current loading scheme, although the force is well known, the location where it is applied is uncertain. Temperature induced variations can be minimized by redesigning the test setup can to improve its thermal stability, and carrying out the experiments in a temperature controlled environment. Both of these are investigated in the next section. The resulting experimental data shows significantly reduced variation, leading to better estimation of the intrinsic parasitic motion.

3.4 Parasitic Motion Estimation: Modified Test Setup

The schematic of the modified test setup is shown in Figure 3.13. Since the capacitive sensor is most sensitive to temperature variations, the test setup is redesigned to be thermally balanced around the capacitive sensor. This is accomplished by clamping the flexure mechanism and the sensor mounts in such a way that, the fixed reference for the entire setup is introduced between the two plates of the capacitive sensor. Figure 3.14 shows a picture of the new test setup.

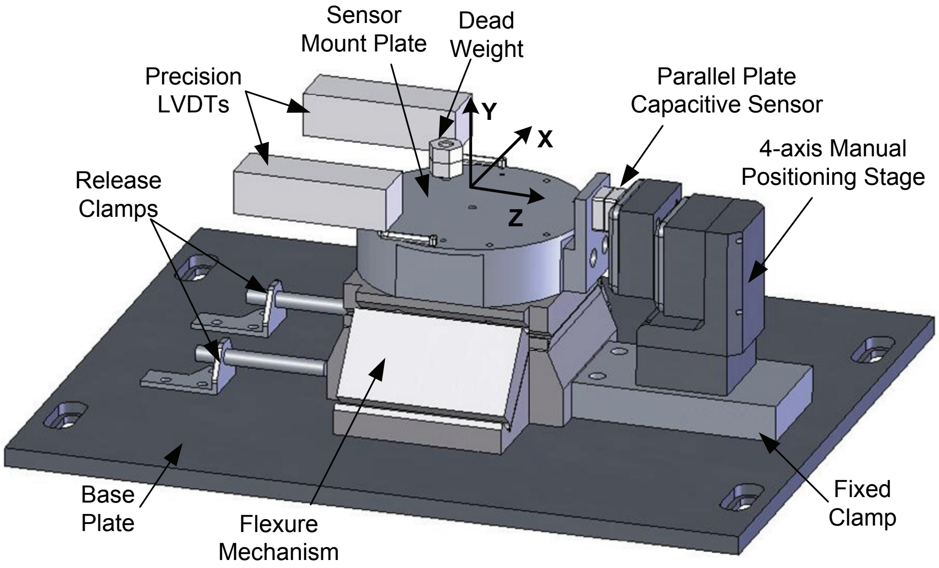

Figure 3.13: Schematic of modified test setup.

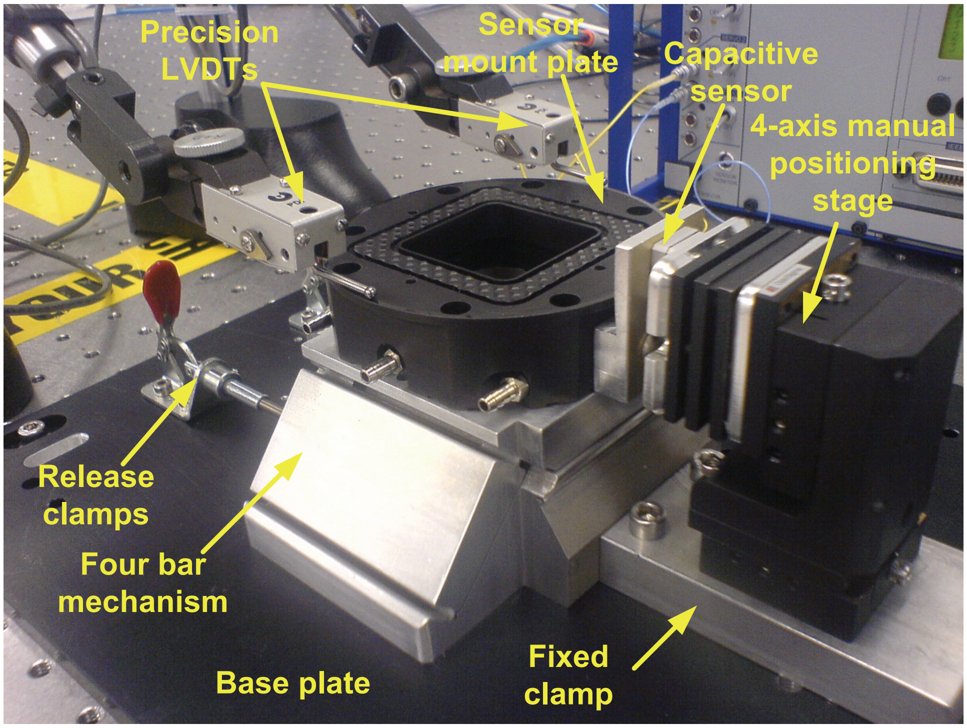

Figure 3.14: Modified test setup.

Figure 3.15 shows the data from the capacitive sensor along with the temperature for a period of 2 hours with the new setup. The sensor follows the temperature variation much more closely as compared to that of the previous setup (see Figure 3.9). By enclosing the setup in a temperature controlled environment, the variation can thus be significantly reduced.

Figure 3.16 shows the unbiased data from the the capacitive sensor and LVDT1, for the case of loading the flexure mechanism by placing the dead weight at X-axis offsets of ±1in. The experiment is carried out in a class 10 clean room, with temperature stability of $\pm 0.2^0$C. The signal from LVDT2

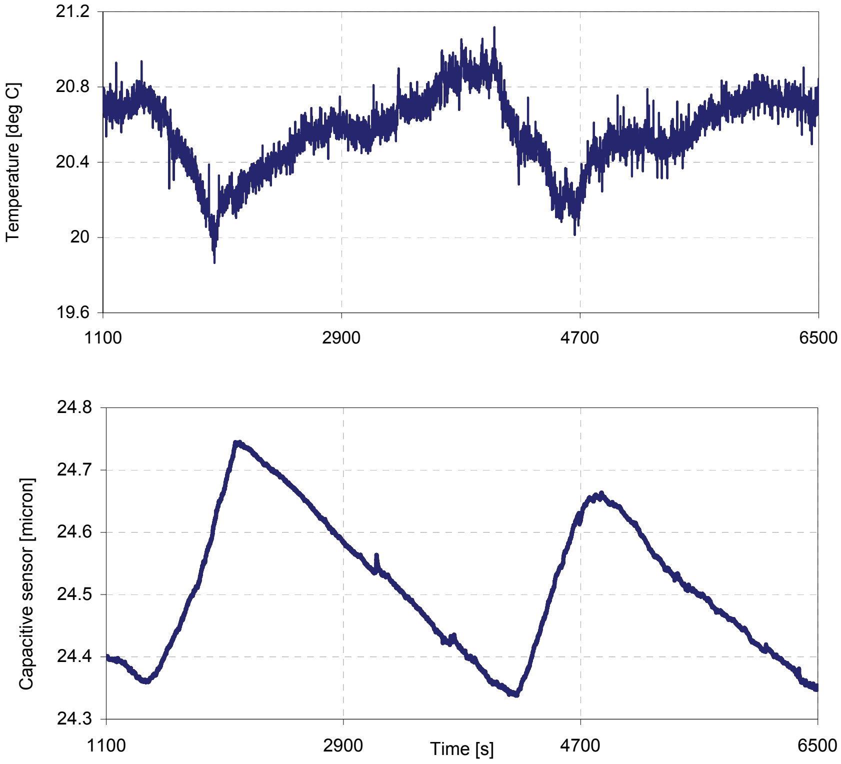

Figure 3.15: Log of capacitive sensor with temperature measurement for the modified setup.

is not shown as it is similar to LVDT1 except for polarity. The temperature drift that was significant in the capacitive sensor data in the old setup (see Figure 3.10) is eliminated by the combined effect of the modified setup and temperature controlled environment.

Figure 3.17 shows the pitch estimation plot from the new data set. The angle of rotation is determined from the two LVDT signals as before, with the capacitive sensor measuring the out-of-plane translation of the platform.

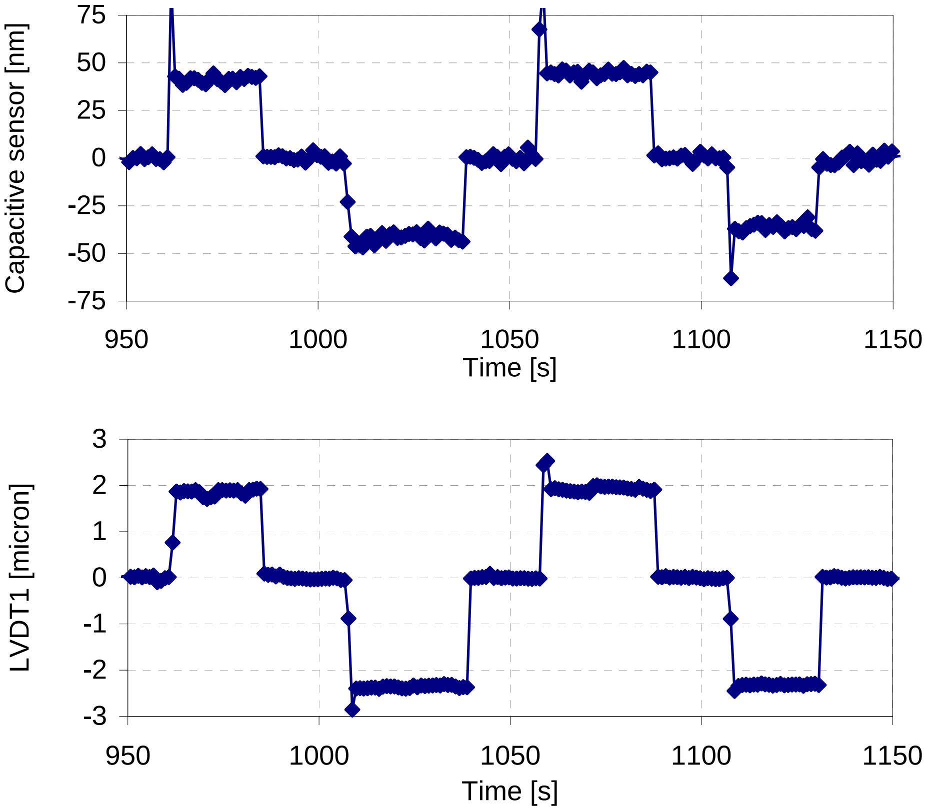

Figure 3.16: Unbiased sensor data; experiment carried out with modified test setup, in a temperature controlled environment.

The goodness of fit is found to be 0.98, and the pitch of twist is estimated as -923.03nm/mrad. A 95% confidence interval determined from the data is found to be 22nm/mrad.

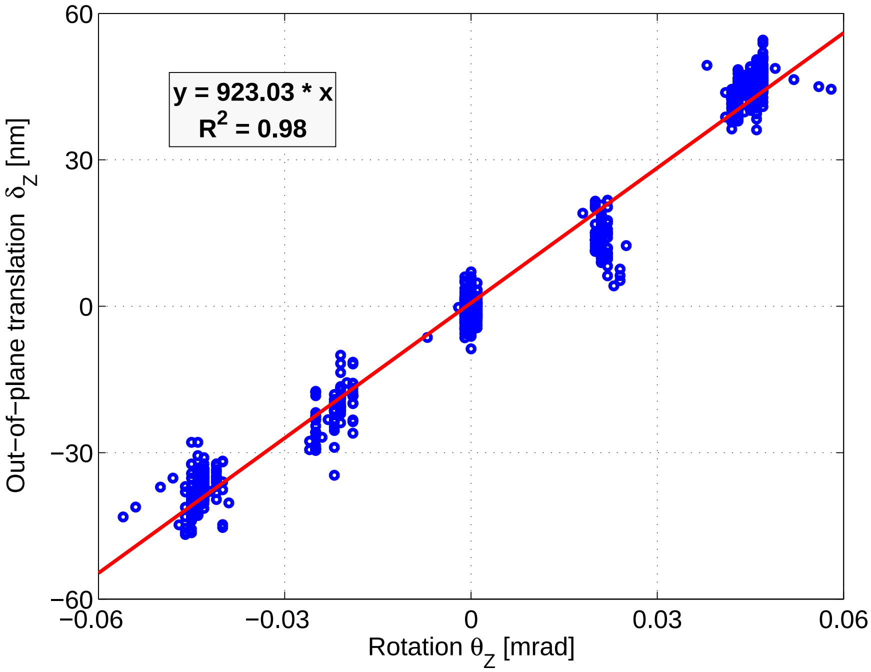

Figure 3.17: Pitch estimation with modified setup.

Chapter 4

Robust Design of Flexure Mechanisms

The parametric nature of the spatial kinetostatic model, developed to analyze the parasitic motion of flexure mechanisms, presents the unique opportunity to investigate the problem of robust synthesis of mechanisms that are less sensitive to geometric errors induced by manufacturing tolerances. The influence of the geometric errors in the flexure joints on the mechanism spatial motion is captured in terms of systematic intrinsic parasitic motion metric. Further, the metric is expressed in terms of the geometry and compliance of flexure joints of the mechanism, the external wrench actuating the mechanism, and the machining process variations in a functional form, as

$$\mathrm{m} = fn\left(\hat{\$}, \mathbf{c}, \boldsymbol{\epsilon}, \hat{\$}_{\mathrm{f}}\right) \tag{4.1}$$

The robust synthesis problem is, in essence, the selection of the parameters of the flexure mechanism such that the standard deviation of the intrinsic parasitic motion metric is minimized for a given variation of the machining process. From the analytical model, it can be inferred that, there are four possible approaches to improve the robustness of flexure mechanisms. Each of them is described below, along with related approaches presented in literature.

4.1 Techniques for Robustness Improvement

1. Kinematic design ($\hat{\$}$) - involves the selection of location and orientation of the flexure joints, to influence the motion characteristics of the mechanism.

   Carretero et al [61] present architecture optimization of a 3-DOF spatial mechanism to reduce parasitic motion. Li [62] describes a kinematic algorithm to adjust the spatial arrangement of a 3RPS mechanism to optimize its dexterity, workspace volume etc. It may be possible to extend these approaches which apply to rigid-link mechanisms to flexure mechanisms kinematic design with the goal of minimizing parasitic motion.

2. Manufacturing process improvement ($\boldsymbol{\epsilon}$) - reduction in the variation of the machining process will indirectly bring about improvement in the precision capability of flexure mechanisms. This is the classical approach, whereby the machining tolerances are reduced and a batch of flexure mechanisms are fabricated. The mechanism which satisfies both desired and undesired motion specifications is selected based on a 'build-test-select' approach. The approach is feasible because the compliant flexure mechanisms in general account for only a small portion of the actual precision positioning system.

3. System design ($\mathbf{c}$) - allocation of the mechanism compliance to achieve robust system performance. This belongs to the category of the well-

defined problem of parameter design in the presence of system uncertainty [63, 64].

Mawardi [65] presents the optimal design of a micro machined compliant force gauge in the presence of machining uncertainties. Wittwer [66, 67] discusses the performance variation of compliant microelectromechanical systems due to surface micro machining process variations, and the optimal design of mechanism parameters to improve robustness. Ryu et al [68] present the optimal design of flexure joint parameters to maximize the yaw motion capability of a precision XYθ mechanism. Kim et al [8] present the optimal design of the spatial stiffness of a flexure hinge based XYZ atomic force scanner translation stage to minimize the parasitic Abbe errors.

4. Active feedback control ($\hat{\$}_{\mathrm{f}}$) - design of the actuation scheme and active control of applied wrench aimed at achieving desired flexure mechanism motion even in the presence of uncertainties in the mechanism geometry.

   Wischnewskiy et al [23] present a commercial sub-nanometer precision XY scanner stage with active compensation of parasitic motion. The precision mechanism is a full six-DOF stage with six actuators operating to achieve planar motion under full state feedback from capacitive sensors arranged in six-axis metrology scheme. Pham et al [69] discuss a selective actuation scheme to kinematically decouple the motion of flexure mechanism as a means of precise micromanipulation.

The kinematic design and active control approaches are application-specific, and have to be implemented for flexure mechanisms on a case-by-case basis. In contrast, the improvement in machining process variations and system design techniques are applicable for the whole class of selectively compliant flexure mechanisms. Further, improving the flexure mechanism precision capability by reducing the tolerance limits is associated with increased cost of the fabricated mechanism. The flexure joint compliance values, on the other hand, are related only to the local joint geometry, namely, the notch radius, the minimum thickness and the hinge width, all of which can be tuned with minimal disruption to the system-level configuration of the application, and at no added system cost. In this thesis, the improvement in robustness of flexure mechanisms to the machining process variation by appropriate selection of the flexure joint compliance, i.e., the system design approach is investigated.

The design of flexure joints is typically aimed at achieving maximum rotational compliance about the sensitive axis of the notch hinge joint, and maximum stiffness about the other axes [9, 16, 70]. This is done so that the flexure joint motion characteristics behavior approaches that of a classical revolute joint (pin joint). While this methodology works well if no geometric errors exist in the mechanism, the precision capability of the flexure mechanism with the idealized joint in the presence of geometric errors may be diminished. For example, the precision capability of the one DOF rotational mechanism is determined with an alternate flexure joint design. Table 4.1 lists the geometry and the compliance distribution of the new flexure joint. The ratio of compliance about the off-axes, cx and cy, to that about the joint sensitive axis, cz, is an order of magnitude larger for the new joint, compared to flexure joint design listed in Table 2.1. However, as seen in Figure 4.1, the precision capability of the four-bar flexure mechanism is found to be 198nm/mrad. This is more than 40% improvement, compared to 340nm/mrad achieved from the original flexure joint design, an improvement that is realized without any changes to the machining tolerances, i.e., at no additional cost.

Table 4.1: Properties of right circular flexure joint: alternate design

(a) Joint properties

Parameter	Value
R	5.0mm
t	1.0mm
b	50.0mm
w	0.0mm
E	69GPa

(b) Joint scalar compliance

Parameter	Value	
cx	7.875×10^{-5}	rad/Nm
cy	7.895×10^{-6}	
cz	8.410×10^{-3}	
cX	1.580×10^{-9}	m/N
cY	1.510×10^{-8}	
cZ	5.0×10^{-9}	

A systematic approach for selection of geometric parameters of flexure joints of the mechanism using the analytical model via an optimization scheme aimed at minimizing the intrinsic parasitic motion metric is presented next. The robust design approach is illustrated using one DOF rotational and one DOF translation flexure mechanisms. The optimization problem is setup first, along with a discussion of the mapping of the scalar compliance of a notch type flexure joint with the joint geometric parameters. The results of the optimization are then discussed.

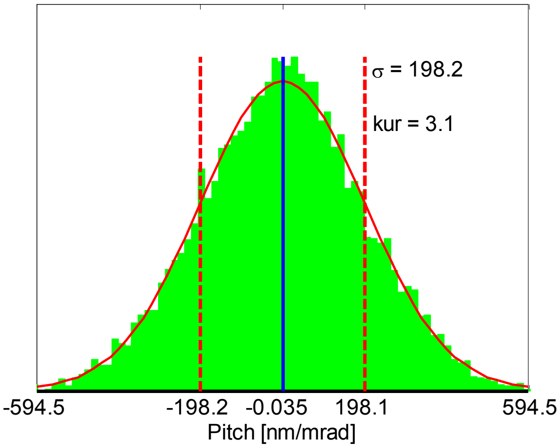

Figure 4.1: Pitch distribution of four-bar flexure mechanism with alternate flexure joint design.

4.2 Flexure Mechanisms Robust Design

The robust design problem is formulated with the standard deviation of the intrinsic parasitic motion metric chosen as the objective function. Minimization of the intrinsic parasitic motion leads to reduced sensitivity of the flexure mechanism to the machining tolerances. The design variables that will be optimized include the flexure joint scalar compliance parameters. Thus, the optimization problem can be stated mathematically as,

$$\underset{\mathbf{c} \in \Re^{+}}{\arg\min} \quad \sigma_{\mathrm{m}} = fn\left(\hat{\$}, \mathbf{c}, \sigma_{\boldsymbol{\epsilon}}, \hat{\$}_{\mathrm{f}}\right) \tag{4.2}$$

The joint compliance terms **c** are related to the joint geometric parameters and the material elasticity. Analytical relationships to determine the compliance parameters from the joint geometry are available for the notch type flexure joint [9, 16, 70, 71]. However, the reference frame chosen to define the compliance terms is different from the centroidal reference frame of the flexure joint that is used in the current compliance model. Further, not all the six compliance terms are defined, most notable exclusion in all the works being the torsional compliance of the flexure joint. Therefore, in order to facilitate robust joint compliance design, an approach to map the relationships between the flexure joint geometric parameters and the six compliance terms is presented, using a combination of finite element analysis and polynomial interpolation scheme.

4.2.1 Flexure Joint Compliance Mapping

Figure 4.2a shows the six compliance parameters of the notch hinge flexure element representing the six degrees of freedom of the joint. Figure 4.2b shows the geometric parameters of the right circular notch-type flexure joint that define the six scalar compliance values associated with the joint.

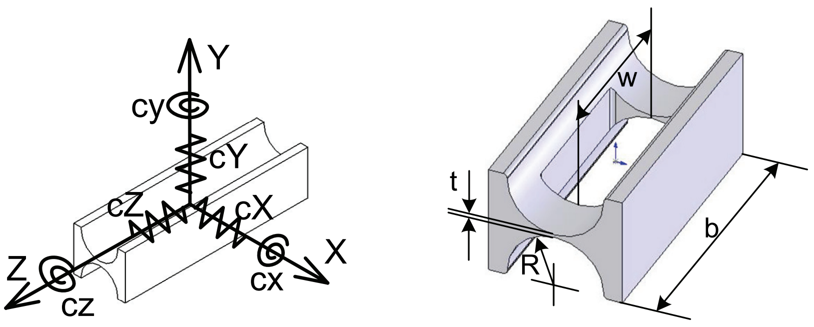

(a) Compliance of a notch type flexure joint.

(b) Right circular notch hinge flexure joint geometry.

Figure 4.2: Compliance mapping.

Table 4.2: Values of flexure joint geometric parameters used in FE analysis

Parameter	Values
R [mm]	[1.5, 3.0, 4.5]
t [mm]	[0.5, 0.625, 0.75, 0.875, 1.0]
w/b	[0.0, 0.33, 0.5]

The relationship between the scalar compliance and the joint geometric parameters is known to be polynomial, with at most linear variation in the notch radius, and cubic variation in hinge thickness [9]. A numerical approximation is developed to map the geometric parameters on to the joint compliance terms. A total of 45 different combinations of the geometric parameters are formed and the six compliance values are determined by FE analysis for each combination. Specifically, three values each are chosen for the geometric parameters R and the width ratio w/b, and five for thickness t. The Table 4.2 lists the numerical values of the parameters chosen for FE analysis.

Figure 4.3a shows the finite element model of the flexure joint used to determine the compliance terms. One end of the joint is fixed and the other end is rigidly connected to a free link, to which loads are applied. The rotational compliance terms cx, cy and cz are determined by applying a unit moment about the X, Y or the Z axis, and finding the angle of rotation about the screw of motion associated with the displacement of the link. Translational compliance terms are determined by applying a unit force about X, Y or the Z axis and finding the corresponding linear displacement. Figure 4.3b shows the joint displacement with a moment applied about the sensitive axis of the joint. The material chosen for the flexure joints in the analysis is aluminum alloy 6061 with Youngs modulus of 69GPa. The FE analysis is carried out using CosmosWorks Linear Solver.

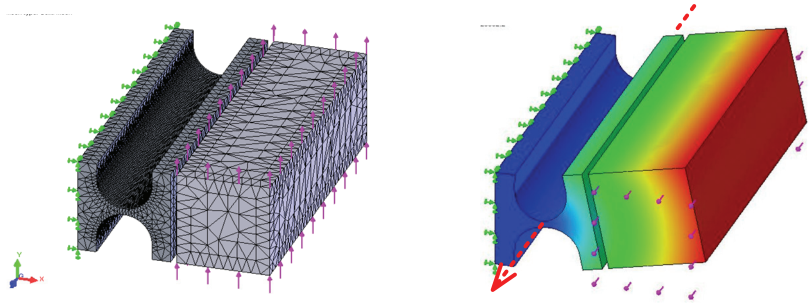

(a) FE Model of notch type flexure joint.

(b) Displacement of the joint for unit moment about sensitive axis.

Figure 4.3: FE analysis used for compliance mapping.

Finally, with the six compliance terms known for the 45 joint designs, piecewise cubic hermite interpolation polynomials (pchip) [48] are used to find the numerical value of the compliance terms for any combination of geometric parameters values. Figure 4.4a shows the numerical approximation for the compliance of the flexure joint about the sensitive axis, ‘cz’, along with the % error in approximation with respect to the analytical formulation [9], shown in Figure 4.4b. The analytical expression used is,

$$\mathrm{cz}\left(\mathrm{R},\mathrm{t},\mathrm{b}\right)=\frac{9\cdot\pi\cdot\mathrm{R}^{0.5}}{2\cdot\mathrm{E}\cdot\mathrm{b}\cdot\mathrm{t}^{2.5}} \tag{4.3}$$

The maximum error of ≈ 10% occurs for the joint geometric parameter ratio (t/2R) of 0.5, which is consistent with the reported difference between FE analysis and the analytical expression [9].

4.2.2 Robust Design Problem Formulation

Combining the statistical sampling to account for the random geometric errors, with the numerical approximations for each of the joint compliance values in terms of the flexure joint geometry parameters, the robust design problem can be formulated as,

$$\underset{\mathbf{d}\,\in\,\Re^{+}}{\arg\min} \quad \sigma_{\mathrm{m}} = fn\left(\hat{\$}, \mathbf{c}\left(\mathbf{d}\right), \sigma_{\varepsilon}, \hat{\$}_{\mathrm{f}}\right) \tag{4.4}$$

where, $\mathbf{d} = \begin{bmatrix} \mathrm{R} & \mathrm{t} & \mathrm{w/b} \end{bmatrix}$ are the design parameters that will be optimized. The upper and lower bounds on the design parameters act as constraints. The minimization is solved via the Nelder-Mead simplex algorithm [72] which is a search based optimization method. Given an initial values of the design variables, the algorithm iteratively searches the design space guaranteeing the improvement of the objective function. As the algorithm is designed for unconstrained nonlinear optimization problems, the constraints are accommodated by using penalty function method, and the augmented objective function is given by,

$$\underset{\mathbf{d}\,\in\,\Re^{+}}{\arg\min} \quad \sigma_{\mathrm{m}} + \lambda_1 \cdot \max\left\{0, \left(\mathbf{d} - \mathbf{d}_{\mathrm{max}}\right)\right\} - \lambda_2 \cdot \min\left\{0, \left(\mathbf{d} - \mathbf{d}_{\mathrm{min}}\right)\right\} \tag{4.5}$$

The values of the penalty coefficients λ_1 and λ_2 are set to an arbitrarily large number. The bounds can be set uniquely for different flexure mechanism designs.

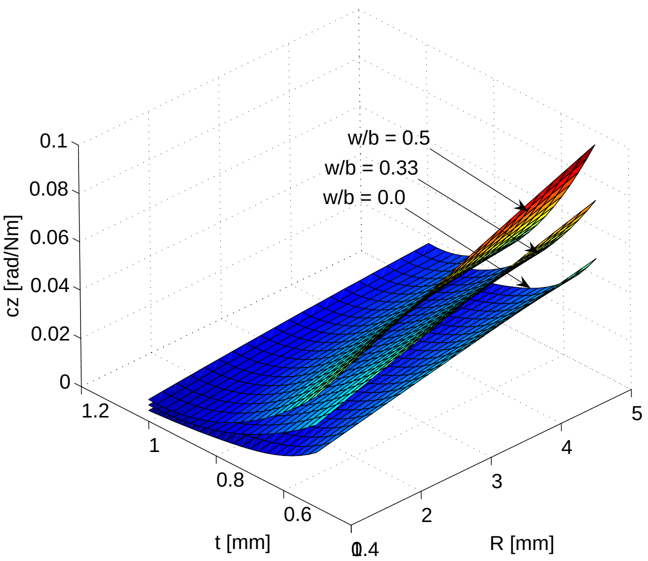

(a) Numerical approximation of cz.

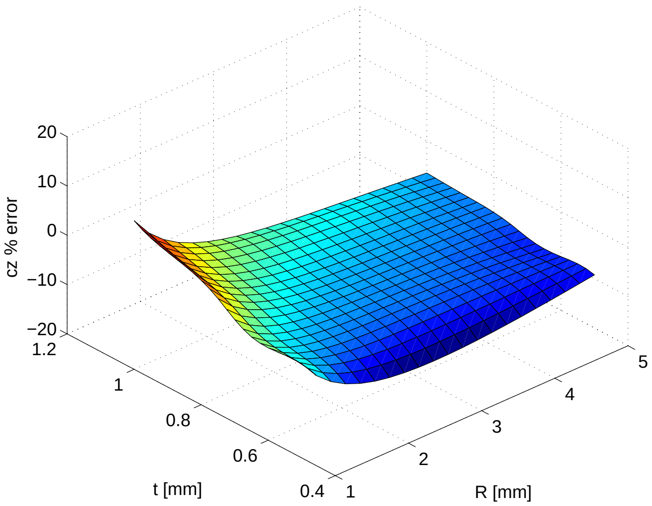

(b) Error in approximation.

Figure 4.4: Compliance mapping with approximation error

4.3 Robust Design of One DOF Rotational Mechanism

4.3.1 Optimization setup

The robust design approach is applied to the one DOF rotational mechanism. The geometry of the mechanism, the external wrench actuating the mechanism, and the statistical properties of the geometric error parameters are all chosen identical to those used in the analysis of the parasitic motion in Chapter 2. Specifically, the geometry of the mechanism is shown in Figure 2.8a. The external wrench acting on the mechanism is given in equation (2.28). The statistical properties of the geometric errors are given in equation (2.24).

The sample size of the geometric error terms used to find the standard deviation of the metric at every iteration of the optimization algorithm is chosen via a convergence analysis. Figure 4.5 shows the plot of the estimate of the standard deviation of pitch of twist of the mechanism versus the sample size. The smallest sample size which consistently yields a 1% error in estimation of the standard deviation of the pitch of twist is found to be 10^4.

The limits on the design variables are chosen so as to keep the optimization algorithm searching for the values within the design space created to map the geometric parameters with the six joint compliance terms. The values of the limits are set as,

$$\mathrm{R}\,[\mathrm{mm}] \subset \left[\begin{array}{cc} 1 & 9 \end{array}\right], \quad \mathrm{t}\,[\mathrm{mm}] \subset \left[\begin{array}{cc} 0.5 & 1 \end{array}\right], \quad (\mathrm{w/b}) \subset \left[\begin{array}{cc} 0 & 0.75 \end{array}\right] \tag{4.6}$$

The MATLAB Optimization Toolbox routine `fminsearch(·)` is used solve the optimization [73]. Five different flexure joint geometry parameters

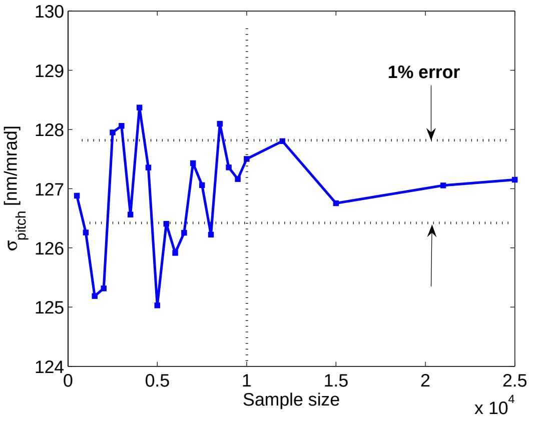

Figure 4.5: Convergence analysis to determine sample size for stochastic optimization.

are chosen as the starting values of the design variables. The number of iterations is set at 25, which was found to yield consistently same results from the optimization.

4.3.2 Results and discussion

The search algorithm results for the standard deviation of the pitch and the trajectories of the design variables between the initial values and their corresponding optimal values are shown in Figure 4.6. The nominal (start) and the optimal geometric parameters for the four flexure joint designs are shown in the Table 4.3 along with the optimal values of the metric. A maximum improvement of 37% in the intrinsic parasitic motion metric is observed (design 1). Also, the optimal value of the metric is found to be nearly identical for all the optimization trials. The six scalar compliance values of the flexure joint are determined from the joint geometric parameters at each step of the optimization and are shown in Figure 4.7.

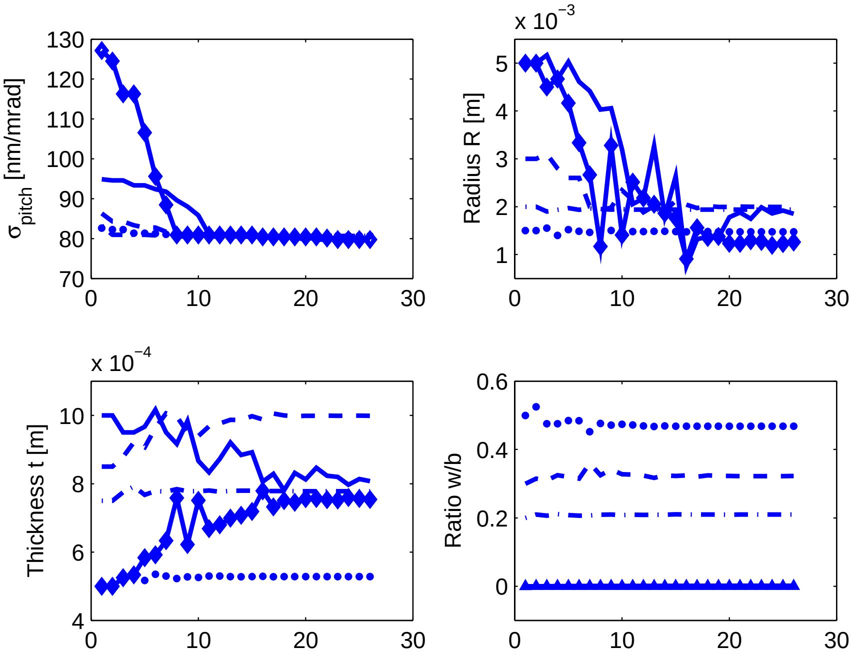

Figure 4.6: Optimization results for one DOF mechanism: metric and design variable trajectories.

Based on the results, it can be inferred that due to the nature of the optimization problem, no single global optimal flexure joint design exists. Rather, the design space is segmented into regions, some of which exhibit improved robustness over others. The analytical model, along with the optimization scheme enables categorization of flexure joint designs as optimal or not. Any of the optimal designs from Table 4.3 may be used in the precision four-bar

Table 4.3: Nominal and optimal values geometric parameters of flexure joint for one DOF rotational mechanism.

#	Nominal				Optimal			
	R [mm]	t [mm]	w/b	σ_m	R [mm]	t [mm]	w/b	σ_m
1	5.0	0.5	0.0	127.169	1.26	0.75	0.0002	79.754
2	5.0	1.0	0.0	94.885	1.85	0.81	0.001	79.882
3	3.0	0.85	0.3	86.282	1.99	0.99	0.32	79.733
4	2.0	0.75	0.2	83.245	1.94	0.78	0.21	80.639
5	1.5	0.5	0.5	82.623	1.48	0.53	0.47	80.682

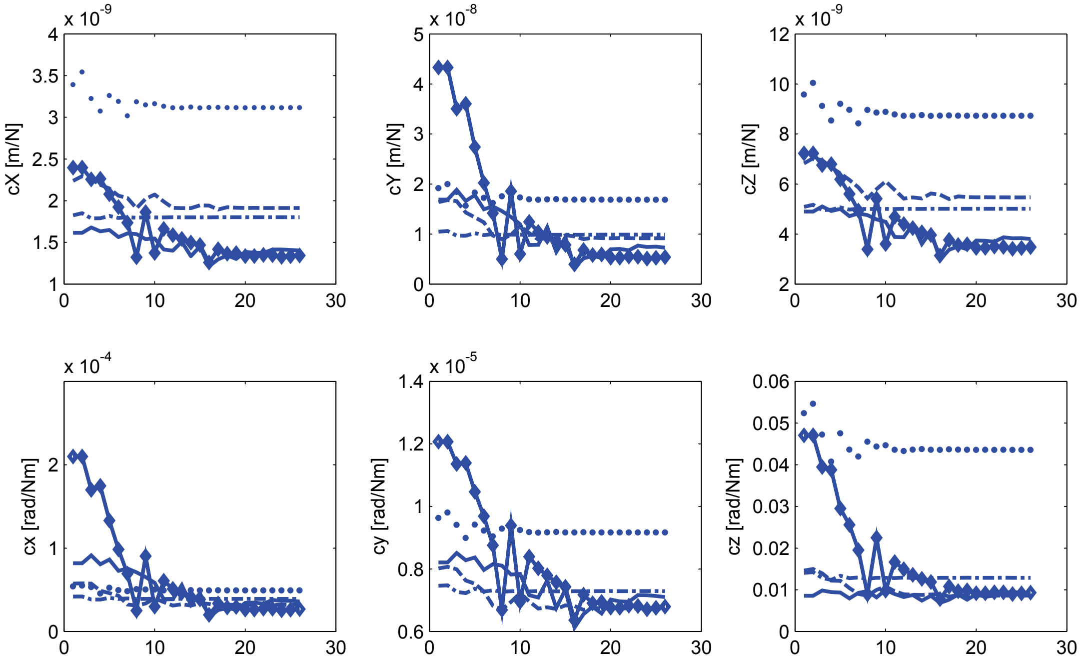

Figure 4.7: Scalar compliance trajectories in one DOF rotational mechanism.

mechanism. The final choice of the design may depend on other considerations such as range of motion, packaging, etc.

To demonstrate that the optimal joint designs are indeed robust over the corresponding nominal ones, the following Eigenscrew analysis of the mechanism compliance is presented.

4.3.3 Interpretation of Robustness through Eigenscrew Analysis

As the twist of motion of a compliant mechanism is governed by the mechanism spatial compliance, it can be expressed as a linear combination of the motion about the eigenscrews of the compliance matrix [34]. Thus by observing the influence of geometric errors due to machining tolerances on the properties of the eigenscrews of the compliant mechanism with the nominal and the optimal flexure joints, the improvement in robustness can be traced back to the improvement in the compliance structure of the mechanism. The details of the eigenscrew analysis of compliance matrices is presented in Appendix B.

The one DOF rotational mechanism is found to possess a dominant eigenscrew pair 1-2, which defines the rotational degree of freedom of the mechanism. Table 4.4 lists the parameters of the eigenscrew pair 1-2.

The twist of motion can then be represented in terms of the eigenscrew pair 1-2 as,

$$\hat{\mathrm{t}} = \hat{\mathrm{E}}_1 \cdot \theta_{\mathrm{E1}} + \hat{\mathrm{E}}_2 \cdot \theta_{\mathrm{E2}} \tag{4.7}$$

The pitch of this twist can be determined from the eigenscrew pair 1-2

Table 4.4: Eigenscrew pair 1-2 of one DOF rotational flexure mechanism

Parameter	$\hat{\mathrm{E}}_1$	$\hat{\mathrm{E}}_2$
$\mathbf{w}$	1.50E-01	1.50E-01
	-1.32E-18	-4.74E-18
	9.89E-01	-9.89E-01
$\boldsymbol{\rho}$	8.00E-18	8.01E-18
	4.16E-04	4.16E-04
	-1.21E-18	1.21E-18
h_{Ei}	-2.77E-03	2.77E-03
c_{Ei}	2.24E-03	2.24E-03

as [31],

$$\begin{aligned}\mathrm{h}_{\mathrm{t}} &= \frac{1}{\sqrt{\theta_{\mathrm{E1}}^2+\theta_{\mathrm{E2}}^2}} \cdot \left[\mathrm{h}_{\mathrm{E1}} \cdot \theta_{\mathrm{E1}}^2 + \mathrm{h}_{\mathrm{E2}} \cdot \theta_{\mathrm{E2}}^2 + \right. \\ &\quad \left. \{(\mathrm{h}_{\mathrm{E1}}+\mathrm{h}_{\mathrm{E2}}) \cdot \mathbf{w}_{\mathrm{E1}} \bullet \mathbf{w}_{\mathrm{E2}} + (\rho_{\mathrm{E1}}-\rho_{\mathrm{E2}}) \bullet \mathbf{w}_{\mathrm{E1}} \otimes \mathbf{w}_{\mathrm{E2}}\} \cdot \theta_{\mathrm{E1}} \cdot \theta_{\mathrm{E2}}\right]\end{aligned} \tag{4.8}$$

If the external wrench acts symmetrical to both the eigenscrews of the pair 1-2, i.e., $\theta_{\mathrm{E1}} = \pm\theta_{\mathrm{E2}}$, the pitch of twist is zero since from Table 4.4, $\mathrm{h}_{\mathrm{E1}} = -\mathrm{h}_{\mathrm{E2}}$, and $\rho_{\mathrm{E1}} = \rho_{\mathrm{E2}}$.

In the presence of geometric errors induced by machining process variations, the above condition is no longer satisfied as the geometry of the mechanism spatial compliance matrix is perturbed. As the variation of the eigenscrew pitch values are directly related to the geometric errors and the constituent flexure joint compliance values, it can be used to compare the nominal and optimal joint compliance for identical machining process variation.

Table 4.5 lists the values of the standard deviation of the pitch difference between the eigenscrew pair 1-2, along with the error in their location.

The optimal joint designs show lower values for both the variations, clearly indicating improved joint compliance distribution with respect to the machining induced geometric errors.

Table 4.5: Perturbation of Eigenscrew properties due to geometric errors with nominal and optimal flexure joint compliance.

	Nominal		Optimal	
#	$\sigma_{(\mathrm{h}_1+\mathrm{h}_2)}$	$\sigma_{(\|\rho_1-\rho_2\|)}$	$\sigma_{(\mathrm{h}_1+\mathrm{h}_2)}$	$\sigma_{(\|\rho_1-\rho_2\|)}$
1	8.964	27.130	5.585	22.950
2	18.709	38.523	5.210	26.152
3	7.963	28.175	7.113	27.923
4	6.043	24.259	5.943	23.812
5	2.295	17.669	2.094	17.080

4.4 Robust Design of One DOF Translation Stage

4.4.1 Optimization setup

The geometry of the mechanism is shown in Figure 2.10. The external wrench acting on the mechanism is given in equation (2.31). The statistical properties of the geometric errors are given in equation (2.24). The sample size of the geometric error terms used to find the standard deviation of the metric at every iteration of the optimization algorithm is chosen as 10^4. The limits on the design variables are kept the same as that for the one DOF rotational mechanism, given in equation (4.6). The same five values of flexure joint geometry parameters used for the one DOF rotational mechanism, are chosen as the start conditions of the design variables. The number of iterations is set at 50, which was found to yield consistently same results from the optimization.

4.4.2 Results and discussion

The search algorithm results for the standard deviation of the pitch and the trajectories of the design variables between the initial values and their corresponding optimal values are shown in Figure 4.8. The nominal (start) and the optimal geometric parameters for the four flexure joint designs are shown in the Table 4.6 along with the optimal values of the metric. The six scalar compliance values of the flexure joint are determined from the joint geometric parameters at each step of the optimization and are shown in Figure 4.9.

The results of the optimization are very different in comparison with the one DOF rotational mechanism. A maximum improvement of only 2% in the intrinsic parasitic motion metric is observed (design 1). The nominal and the optimal values of the metric for each of the design are nearly identical. This is possibly because the nominal flexure joints are already in the region of the design space that corresponds to the optimal performance and no further improvement in the metric is possible. Further, the larger number of joints in the one DOF translation stage induce the elastic averaging effect [17], due to which the influence of flexure joint compliance on the parasitic motion of the mechanism is not as significant as in the one DOF rotational mechanism.

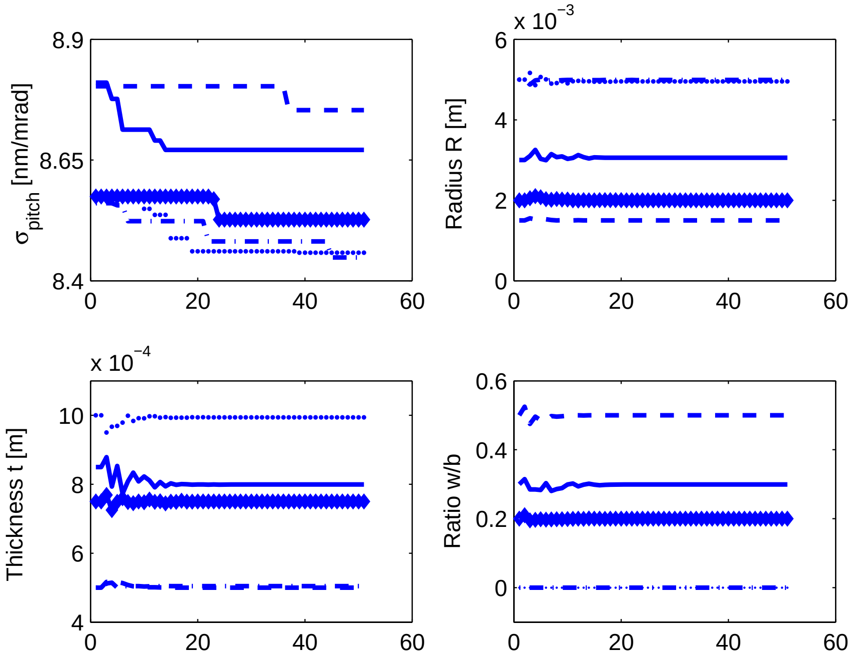

Figure 4.8: Optimization results for one DOF translation stage: metric and design variable trajectories.

Table 4.6: Nominal and optimal values geometric parameters of flexure joint for one DOF translation stage.

	Nominal				Optimal			
#	R [mm]	t [mm]	w/b	σ_m	R [mm]	t [mm]	w/b	σ_m
1	5.0	0.5	0.0	8.8104	1.26	0.75	0.0002	8.6711
2	5.0	1.0	0.0	8.8026	1.85	0.81	0.001	8.7531
3	3.0	0.85	0.3	8.5604	1.99	0.99	0.32	8.4483
4	2.0	0.75	0.2	8.5807	1.94	0.78	0.21	8.4580
5	1.5	0.5	0.5	8.5744	1.48	0.53	0.47	8.5266

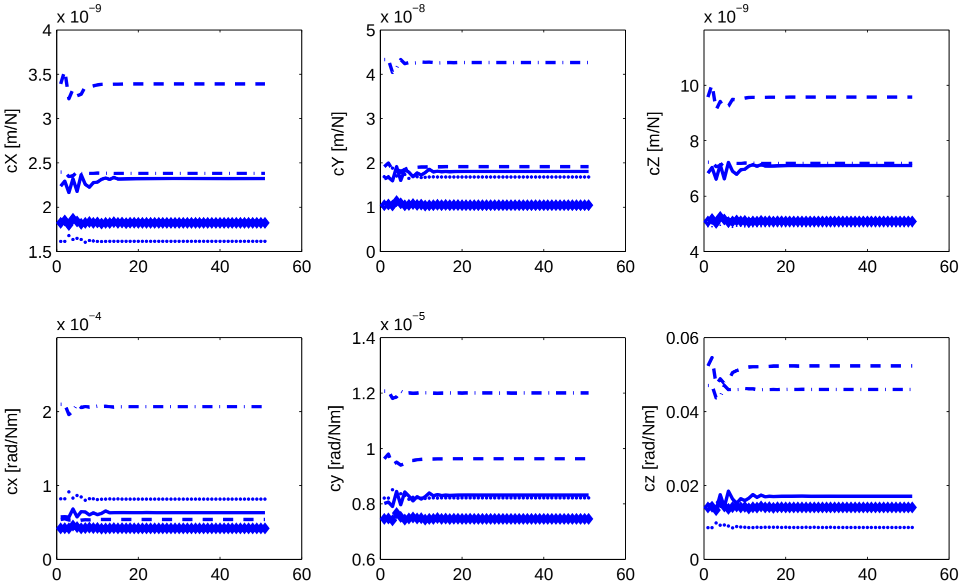

Figure 4.9: Scalar compliance trajectories in one DOF translation stage.

Chapter 5

Conclusions

5.1 Summary and Contributions

The problem of parasitic motion in flexure based compliant mechanisms used in precision applications is addressed in this thesis. Geometric errors induced by machining process variations lead to significant discrepancies in the desired motion of flexure mechanisms at the nano-scale. The undesirable motion, termed parasitic motion, decreases the precision capability of the flexure mechanism. The interaction of flexure joint compliance and geometry in compliant mechanisms makes the analysis of the error motion different from classical rigid-link mechanisms. While finite element analysis can present numerical estimates of the parasitic motion, no insight is available that can lead to better understanding of the geometry of the error motion or in synthesizing flexure mechanisms that are robust to the machining process variations. A systematic approach to analyze the parasitic motion in flexure-based precision compliant mechanisms, and to design flexure mechanisms with reduced sensitivity to machining process variations is presented.

The parasitic motion of the flexure mechanisms induced by the geometric errors due to machining tolerances is determined using a spatial kinetostatic model based on screw systems. The model not only enables numerical computation of complete spatial motion of the flexure mechanism, it also reveals a key geometric insight into the parasitic motion problem. It is found that, regardless of the special screw system of motion the mechanism is designed with, in the presence of geometric errors, the twist of motion belongs to the general screw system of the same order. The geometric insight enables decoupling of the parasitic motion into extrinsic and intrinsic error motions. It is shown that the intrinsic parasitic motion is inherently tied to the mechanism motion, and metrics are defined to quantify it for rotational and translational DOF flexure mechanisms.

The extent of intrinsic parasitic motion of a one DOF rotational flexure mechanism is experimentally determined. A test setup is built for the purpose using two precision LVDTs and a capacitive sensor in a three axis metrology scheme. The setup is also used to estimate the effective rotational compliance of the mechanism about its DOF, and is shown to compare well with finite element analysis results.

The parametric model is used to formulate the robust design problem. The flexure joint geometric parameters, which define the scalar compliance associated with the flexure joint, are tuned to minimize the intrinsic parasitic motion metric. The geometric error terms in the model are sampled with Gaussian distribution, thereby converting the stochastic optimization into a deterministic one. The sample size is chosen via convergence analysis. Nonlinear search technique using Nelder-Mead algorithm is used to solve the optimization problem. The robust design approach is demonstrated with a one rotational DOF flexure mechanism chosen as the example. Starting nominal flexure joint design parameters, the optimization algorithm finds the optimal values which lead to a maximum of nearly 40% improvement in the precision capability of the one DOF rotational flexure mechanism. The improvement is shown to be related to the improvement in the compliance distribution of the mechanism via eigenscrew analysis of the mechanism compliance matrix. Improvement in the precision capability of the one DOF translation stage via compliance optimization was found to be insignificant, owing to the elastic averaging effect of the large number of flexure joints.

The research presented in this thesis makes the following contributions in the study of motion characteristics of precision flexure-based compliant mechanisms.

- The analysis of flexure mechanisms using screw systems presented here is the first mathematical/geometric characterization of parasitic motion. The analysis leads to decoupling of parasitic motion into extrinsic and intrinsic error motion, based on whether or not they can be corrected via calibration. Metrics to quantify the intrinsic error motion of rotational and translational DOF mechanisms are defined based on screw systems analysis.
- A test setup is developed to demonstrate the metrology capability requirement for experimental investigation of parasitic motion of flexure

mechanisms. It is used to determine the pitch of screw motion of a one DOF rotational flexure mechanism.

- The problem of robust synthesis of flexure-based precision compliant mechanisms is developed based on the parametric compliance model. Geometric parameters of flexure joints are chosen via an optimization scheme to minimize the intrinsic parasitic motion metric. Results of optimization are presented for one DOF rotational and translational flexure mechanisms, and the enhanced robustness is shown to be related to improvement in compliance distribution in the mechanisms.

5.2 Directions for Future Work

Active compensation of parasitic motion

The proposed robust design approach of the flexure mechanisms does not completely eliminate the intrinsic parasitic motion. The residual error motion can, however, be compensated by active control of the applied wrench to the mechanism. The developed spatial kinematics based model of flexure compliance can be used as the plant, with the geometric errors modeled as parametric uncertainties. The proposed six axis metrology, or in the particular case of the one DOF rotational mechanism, the developed three axis measurement scheme, can be employed to provide real-time estimate of the intrinsic parasitic motion. The only subsystem that requires to be developed is an actuation system capable of applying any specified wrench. Further analysis of the motion in terms of eigenscrews of the mechanism compliance can help in reducing the complexity of the actuation system. The costs associated with the active control scheme may be offset by the improved precision that can be achieved.

Extension of parasitic motion analysis to MEMS-based precision mechanisms

MEMS-based precision compliant mechanisms are becoming popular for a number of applications in the field of biotechnology, electronics, micromanipulation (see for example, [6, 65, 66, 74]). A unique feature of using screw systems for analyzing spatial motion is that, the modeling is invariant to scale of the motion. The parasitic motion analysis approach developed for macroscale flexure mechanisms can be extended to the study of motion characteristics of micro-scale mechanisms. The nature of the geometric errors induced by microfabrication techniques will be different than those due to wire EDM process considered in this thesis. The robust synthesis approach will differ in terms of the choice of design variables, and constraints on the optimization. The metrics for intrinsic parasitic motion, however, can be used without any change.

Extension of parasitic motion analysis to complex flexure systems

The analysis of precision flexure mechanisms promises better understanding of the intrinsic parasitic motion and leads to robust precision applications with improved precision capability. The analysis of parasitic motion can be extended to complex flexure systems, which consist of a number of flexure mechanisms are assembled together (see for example, [18, 75]). The effective precision capability of the complex system is a not affected just by the individual flexure mechanism precision, but also includes the errors in assembly. Using the flexure mechanism analysis procedure in combination with a model of assembly tolerances [76], a methodology to study the motion characteristics complex flexure systems can be developed. Value judgments regarding the choice of improving either the machining tolerance of constituent flexure mechanisms, or the assembly tolerance of the system can be made by from the systematic analysis, leading to systems with improved robustness.

Appendices

Appendix A

Extraction of Twist Parameters from Displacement Results

The motion general rigid body motion is the screw motion, and the twist of motion provides the minimal representation for the spatial motion characteristic, namely, displacement, velocity, and acceleration. The representation of spatial displacement of flexure mechanisms in terms of screws provides critical geometric insight into the mechanism motion. However, the displacement results from such techniques as finite element analysis is often presented in terms of numerical displacement values along the Cartesian coordinates of the chosen reference frame. The procedure to obtain the twist of motion from the numerical displacement values is presented here.

The general representation for twist of motion in any reference frame '0' is given by,

$$ {}^{0}\hat{\mathrm{t}} = \begin{bmatrix} \mathbf{w} \\ \mathrm{h} \cdot \mathbf{w} + \boldsymbol{\rho} \otimes \mathbf{w} \end{bmatrix} \cdot \theta \tag{A.1} $$

Thus, in order to determine the twist, the direction vector $\mathbf{w}$, its location $\boldsymbol{\rho}$, the pitch of the screw axis h, and the rotation about the screw θ have to be identified.

Figure A.1 shows the displacement of a rigid body along with the associated twist. The initial locations of a set of points $\mathbf{p}_\mathrm{i}$, and the displacement of the corresponding points $\mathbf{d}_\mathrm{i}$, are known in some reference frame '0'. The final locations $\mathbf{d}_\mathrm{i}$, of the set of points are then known. The twist parameters are determined from this information as below.

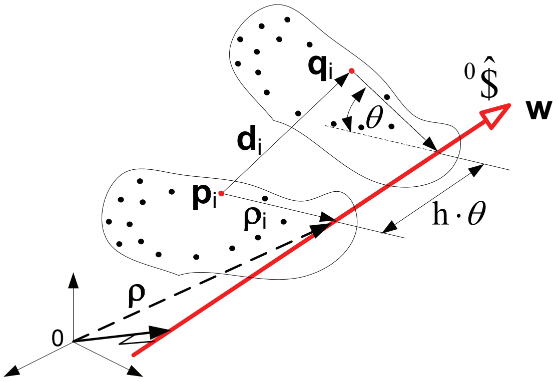

Figure A.1: Displacement of a rigid body and the associated twist.

Direction vector: w

The rotation matrix corresponding to the displacement of the rigid body can be obtained as in [52]. Firsly, the centroids of the set of points before and after displacement are obtained as,

$$\mathbf{p}_\mathrm{C} = \sum_{\mathrm{i}=1}^{\mathrm{N}} \mathbf{p}_\mathrm{i}, \quad \mathbf{q}_\mathrm{C} = \sum_{\mathrm{i}=1}^{\mathrm{N}} \mathbf{q}_\mathrm{i} \tag{A.2}$$

The vectors directed from the centroid to each of the points is then obtained,

$$\begin{aligned} \mathbf{p}_\mathrm{i}^{*} &= \mathbf{p}_\mathrm{i} - \mathbf{p}_\mathrm{C} \\ \mathbf{q}_\mathrm{i}^{*} &= \mathbf{q}_\mathrm{i} - \mathbf{q}_\mathrm{C} \end{aligned} \tag{A.3}$$

Then, determine the matrix,

$$\mathbf{A}_{3\times3} = [\mathbf{q}^*]^{\mathrm{T}}_{\mathrm{N}\times3}\,[\mathbf{p}^*]_{\mathrm{N}\times3} \tag{A.4}$$

and find its singular value decomposition,

$$\mathbf{A}_{3\times3} = \mathbf{u}\cdot\boldsymbol{\sigma}\cdot\mathbf{v}^{\mathrm{T}} \tag{A.5}$$

Finally, the rotation matrix associated with the displacement is given by,

$$\mathbf{R}_{3\times3} = \mathbf{u}\cdot\begin{bmatrix} 1 & 0 & 0 \\ 0 & 1 & 0 \\ 0 & 0 & \left\|\mathbf{u}\cdot\mathbf{v}^{\mathrm{T}}\right\| \end{bmatrix}\cdot\mathbf{v}^{\mathrm{T}} \tag{A.6}$$

The direction vector of the twist of motion corresponds to the eigen vector of the rotation matrix **R** which has a eigen value of 1 [77].

Angular rotation: θ

The rotation about the screw axis is given by the relationship,

$$\mathrm{tr}\left(\mathbf{R}\right) = 1 + 2\cos\left(\theta\right) \tag{A.7}$$

where, tr(·) is the matrix trace operation.

Pitch: h

The pitch of twist is defined as the translation along the axis of the screw vector, per unit rotation about the screw axis. Thus, knowing the direction vector **w**, the rotation angle θ, and the displacement $\mathrm{d_i}$ of any one point on the rigid body, the pitch of twist can be determined as,

$$h = \frac{\mathrm{d}_{\mathrm{i}}^{\mathrm{T}} \cdot \mathbf{w}}{\theta} \tag{A.8}$$

As a means of ensuring numerical consistency, the pitch of twist can be obtained for all the points with known displacement, and averaging the result.

Location vector: $\boldsymbol{\rho}$

The twist location $\boldsymbol{\rho}$ can be determined as,

$$\boldsymbol{\rho} = \mathrm{p}_{\mathrm{i}} + \boldsymbol{\rho}_{\mathrm{i}} \tag{A.9}$$

From the Figure A.1, the displacement vector of any point d_{i} can be expressed as,

$$\mathbf{d}_{\mathrm{i}} = \mathbf{q}_{\mathrm{i}} - \mathbf{p}_{\mathrm{i}} = \boldsymbol{\rho}_{\mathrm{i}} + \mathbf{w} \cdot (\mathrm{h}\theta) - \mathbf{R} \cdot \boldsymbol{\rho}_{\mathrm{i}} \tag{A.10}$$

Pre-multiplying by $\left(\mathbf{I} - \mathbf{R}^{\mathrm{T}}\right)$ on both sides yields,

$$\begin{aligned} \left(\mathbf{I} - \mathbf{R}^{\mathrm{T}}\right) \cdot \mathbf{d}_{\mathrm{i}} &= \left(\mathbf{I} - \mathbf{R}^{\mathrm{T}}\right) \cdot \left[\left(\mathbf{I} - \mathbf{R}\right) \boldsymbol{\rho}_{\mathrm{i}} + \mathbf{w} \cdot (\mathrm{h}\theta)\right] \\ &= \left[2\mathbf{I} - \left(\mathbf{R}^{\mathrm{T}} + \mathbf{R}\right)\right] \boldsymbol{\rho}_{\mathrm{i}} + 0 \end{aligned} \tag{A.11}$$

Writing the rotation matrix in terms of its invariant parameters [77]

$$\mathbf{R} = \mathbf{w}\mathbf{w}^{\mathrm{T}} + \cos(\theta)\left(\mathbf{I} - \mathbf{w}\mathbf{w}^{\mathrm{T}}\right) + \sin(\theta)\left(\mathbf{w}\otimes\right) \tag{A.12}$$

Then,

$$\begin{aligned} \left(\mathbf{R}^{\mathrm{T}} + \mathbf{R}\right) &= 2\mathbf{w}\mathbf{w}^{\mathrm{T}} + 2\cos(\theta)\left(\mathbf{I} - \mathbf{w}\mathbf{w}^{\mathrm{T}}\right) \\ &= 2\cos(\theta)\,\mathbf{I} + 2\left(1 - \cos(\theta)\right)\mathbf{w}\mathbf{w}^{\mathrm{T}} \end{aligned} \tag{A.13}$$

Substituting this result in equation (A.11),

$$\left(\mathbf{I}-\mathbf{R}^{\mathrm{T}}\right)\mathbf{d}_{\mathrm{i}}=2\left(1-\cos\left(\theta\right)\right)\left(\mathbf{I}-\mathbf{w}\mathbf{w}^{\mathrm{T}}\right)\boldsymbol{\rho}_{\mathrm{i}} \tag{A.14}$$

Further, if $\boldsymbol{\rho}_{\mathrm{i}}$ is chosen perpendicular to $\mathbf{w}$,

$$\left(\mathbf{w}\mathbf{w}^{\mathrm{T}}\right)\boldsymbol{\rho}_{\mathrm{i}}=\mathbf{w}\left(\mathbf{w}^{\mathrm{T}}\boldsymbol{\rho}_{\mathrm{i}}\right)=\mathbf{w}\left(\mathbf{w}\bullet\boldsymbol{\rho}_{\mathrm{i}}\right)=0 \tag{A.15}$$

Thus,

$$\boldsymbol{\rho}_{\mathrm{i}}=\frac{\left(\mathbf{I}-\mathbf{R}^{\mathrm{T}}\right)\cdot\mathbf{d}_{\mathrm{i}}}{2\left(1-\cos\left(\theta\right)\right)} \tag{A.16}$$

Appendix B

Mobility Analysis of Flexure Mechanisms via Eigenscrew Decomposition of Spatial Compliance Matrix

Mobility analysis of a mechanism involves identifying the degrees of freedom of its motion. Rigid-link mechanisms with classical joints like revolute, prismatic, cylindrical, etc., are analyzed via reciprocal screw systems to determine the twists of motion and wrenches of constraint [78–80]. The straight-forward extension of this approach to compliant mechanisms does not work well, since the compliance associated with the joints is not taken into account. For example, if the flexure joints are modeled with six degrees of freedom, the resulting degrees of freedom of the flexure mechanism will always be six from the reciprocal screw analysis. A methodology to identify the useful degrees of freedom of a flexure mechanism using eigenscrew analysis is presented here.

The spatial kinetostatic model of the flexure mechanism compliance developed in Chapter 2 determines the task-space compliance matrix of the mechanism in terms of the geometry and the compliance of the constituent flexure mechanisms. The compliance matrix can be decomposed into eigenscrews and eigen-compliances as described in [34, 81]. Since the twist of motion of a compliant mechanism is governed by the mechanism spatial compliance, it can be expressed as a linear combination of the motion about the eigenscrews of the compliance matrix [34]. By analyzing the contribution of each eigenscrew to the twist of motion, directions of motion and constraint in the flexure mechanism can be identified. The analysis is illustrated by using the one DOF and two DOF rotational flexure mechanisms as examples.

The eigenscrew decomposition of a spatial compliance matrix is given by,

$$\mathbf{C} \cdot \lambda = \hat{\mathbf{E}} \cdot \boldsymbol{\lambda} \tag{B.1}$$

where, $\hat{\mathbf{E}}$ is a 6×6 matrix containing the six eigenscrews, and $\boldsymbol{\lambda}$ is a 6×6 diagonal matrix containing the six eigen values of the matrix. The task-space compliance matrix is semi-definite with three positive and three negative eigen values [33, 45].

As the eigenscrews belong to a compliance matrix, they physically represent flexure joints themselves, and are associated with a scalar compliance. The eigen-compliance associated with the eigenscrew $\hat{\mathrm{E}}_{\mathrm{i}}$ is given by [34, 81],

$$\mathrm{c}_{\mathrm{Ei}} = \frac{\lambda_{\mathrm{i}}}{2 \cdot \mathrm{h}_{\mathrm{Ei}}} \tag{B.2}$$

where, h_{Ei} represents the pitch of the eigenscrew $\hat{\mathrm{E}}_{\mathrm{i}}$. The eigen-compliances are always positive since the signs of the eigen values and the eigenscrew pitches are the same [34].

The eigen structure representation of the compliance matrix can then be written as,

$$\mathbf{C} = \hat{\mathbf{E}} \cdot \mathbf{c_E} \cdot \hat{\mathbf{E}}^{\mathrm{T}} \cdot \boldsymbol{\Delta} \tag{B.3}$$

Here, $\mathbf{c_E}$ is a diagonal matrix containing the eigen-compliance values corresponding to the six eigenscrews.

For an external wrench, $\hat{\mathrm{f}}$, acting on the compliant mechanism, the twist of motion can be expressed as,

$$\begin{aligned} \hat{\mathrm{t}} &= \mathbf{C} \cdot \hat{\mathrm{f}} \\ &= \left(\hat{\mathbf{E}} \cdot \mathbf{c_E} \cdot \hat{\mathbf{E}}^{\mathrm{T}} \cdot \boldsymbol{\Delta}\right) \cdot \hat{\mathrm{f}} \\ &= \hat{\mathbf{E}} \cdot \theta_{\mathrm{E}} \end{aligned} \tag{B.4}$$

Here, the reciprocal product $\hat{\mathbf{E}}^{\mathrm{T}} \cdot \boldsymbol{\Delta} \cdot \hat{\mathrm{f}}$ represents the effective moment acting on each of the eigenscrews due to the external wrench. This yields the effective rotation about the eigenscrews, θ_{E}, whose magnitude is determined by the corresponding eigen-compliance. The twist of motion can thus be expressed as a linear combination of the motion about the eigenscrews of the compliant mechanism, i.e.,

$$\hat{\mathrm{t}} = \sum_{\mathrm{i}=1}^{6} \hat{\mathrm{E}}_{\mathrm{i}} \cdot \theta_{\mathrm{Ei}} \tag{B.5}$$

One DOF Rotational Mechanism

Table B.1 shows the eigenscrews and eigen-compliances of the spatial compliance matrix of one DOF rotational flexure mechanism for the ideal case of zero geometric errors. The flexure joint design used in the analysis is the nominal design # 1 from Table 4.3. The mechanism geometry is shown in

Figure 2.8a. The mechanism compliance shows three pairs of eigenscrews with equal eigen-compliances. The pairs intersect and have equal and opposite pitch values. One pair of eigenscrews coincide, thus forming a compliant axis in the mechanism [33], while the other two pairs intersect this compliant axis orthogonally. The eigenscrew pairs are shown in Figure B.1.

Table B.1: Eigenscrew parameters of four bar flexure mechanism compliance

	$\hat{\mathrm{E}}_1$	$\hat{\mathrm{E}}_2$	$\hat{\mathrm{E}}_3$	$\hat{\mathrm{E}}_4$	$\hat{\mathrm{E}}_5$	$\hat{\mathrm{E}}_6$
$\mathbf{w}$	1.50E-01	1.50E-01	8.80E-01	8.80E-01	7.96E-11	-7.94E-11
	-1.32E-18	-4.74E-18	-6.75E-13	-6.75E-13	1.00E+00	-1.00E+00
	9.89E-01	-9.89E-01	-4.76E-01	4.76E-01	-4.03E-11	-4.02E-11
$\boldsymbol{\rho}$	8.00E-18	8.01E-18	2.80E-14	2.80E-14	-3.29E-12	-3.28E-12
	4.16E-04	4.16E-04	4.23E-03	4.23E-03	3.03E-23	3.02E-23
	-1.21E-18	1.21E-18	4.58E-14	-4.58E-14	-5.74E-12	5.73E-12
h_t	-2.77E-03	2.77E-03	-7.83E-03	7.83E-03	-8.16E-02	8.16E-02
c_{Ei}	2.24E-03	2.24E-03	2.59E-05	2.59E-05	2.33E-06	2.33E-06

Noting that the eigen-compliances corresponding to eigenscrew pairs 1-2 are two orders of magnitude larger compared to the other four eigen-compliances, the influence of the eigenscrew pairs 3-4 and 5-6 on the twist of mechanism can be neglected. Further, the linear combination of the eigenscrew pair 1-2 yields a zero pitch screw, i.e., $\left(\hat{\mathrm{E}}_1 + \hat{\mathrm{E}}_2\right)$ is a line vector. The combined line screw is located at the origin of the reference frame and oriented along the Z axis, as shown schematically in Figure B.2. In other words, the effective degree of freedom of the flexure mechanism is represented by a single zero pitch screw, i.e., the ideal four bar flexure mechanism in the absence of any geometric errors has one purely rotational degree of freedom.

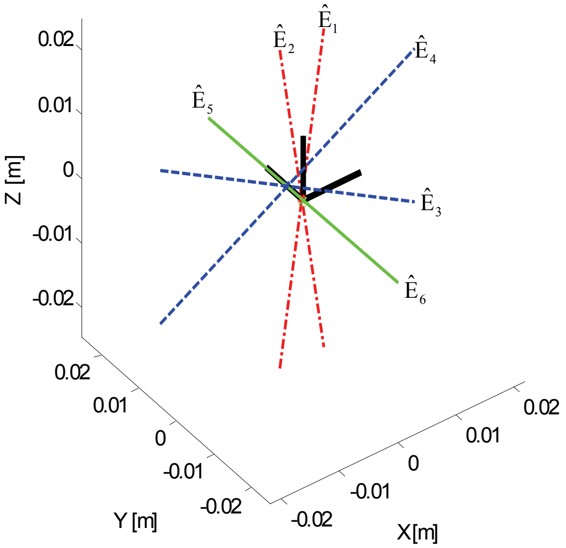

Figure B.1: Eigenscrews of the one DOF rotational flexure mechanism.

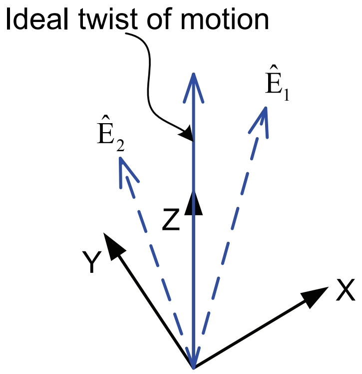

Figure B.2: Equivalent DOF of four-bar flexure mechanism.

Two DOF Rotational Mechanism

Table B.2 shows the eigenscrews along with the eigen compliances of the mechanism. The mechanism compliance exhibits three pairs of eigenscrews with equal eigen compliances. The pairs intersect and have equal and opposite pitch values. One pair of eigenscrews coincide, and thus form a compliant axis in the mechanism, while the other two pairs intersect this compliant axis orthogonally. They are shown schematically in Figure B.3a.

Table B.2: Eigenscrew parameters of tip-tilt flexure mechanism compliance

	$\hat{E}_1$	$\hat{E}_2$	$\hat{E}_3$	$\hat{E}_4$	$\hat{E}_5$	$\hat{E}_6$
$\mathbf{w}$	-8.297E-1	8.297E-1	-5.562E-1	-5.562E-1	9.43E-15	9.43E-15
	-5.582E-1	-5.582E-1	8.311E-1	-8.311E-1	-3.87E-14	3.87E-14
	-3.27E-14	3.27E-14	-2.95E-14	-2.95E-14	1.00	1.00
$\boldsymbol{\rho}$	7.86E-16	7.86E-16	-1.10E-15	-1.10E-15	7.55E-18	7.55E-18
	-1.20E-15	1.20E-15	-7.18E-16	7.18E-16	1.73E-16	-1.73E-16
	5.515E-4	5.515E-4	5.857E-4	5.857E-4	6.65E-30	6.65E-30
h_t	7.013E-3	-7.013E-3	6.998E-3	-6.998E-3	-1.896E-2	1.896E-2
c_{Ei}	2.151E-4	2.151E-4	2.189E-4	2.189E-4	2.966E-5	2.966E-5

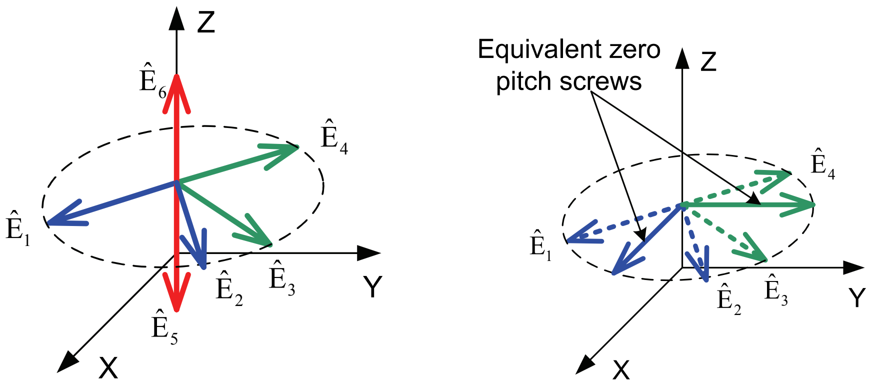

(a) Eigenscrews of tip-tilt mechanism

(b) Equivalent DOF of tip-tilt mechanism

Figure B.3: Mobility analysis of tip-tilt mechanism via eigenscrews.

The eigen compliances corresponding to eigenscrew pairs 1-2 and 3-4 are nearly equal, and the eigen compliances along the compliant axis 5-6 are an order of magnitude smaller compared to the other four eigen compliances. Thus, the influence of the compliant axis on the twist of mechanism can be neglected. Further, the linear combination of the eigenscrew pairs 1-2 and 3-4 results in zero pitch screws, i.e., $\left(\hat{\mathrm{E}}_1 + \hat{\mathrm{E}}_2\right)$ and $\left(\hat{\mathrm{E}}_3 + \hat{\mathrm{E}}_4\right)$ are line vectors, and that they intersect orthogonally, as shown in Figure B.3b. Thus, the effective degrees of freedom of the mechanism is represented by two zero pitch screws intersecting orthogonally, i.e., the mechanism is equivalent to a universal joint. The resultant twists of freedom of the mechanism belong to the special two-system characterized by a planar pencil [31].

Bibliography

[1] Choi, B. J., Sreenivasan, S. V., Johnson, S., Colburn, M., and Wilson, C. G., 2001. "Design of orientation stages for step and flash imprint lithography". *Precision Engineering,* **25**(3), pp. 192–199.

[2] Lee, J., Choi, K. B., and Kim, G. H., 2006. "Design and analysis of the single-step nanoimprinting lithography equipment for sub-100 nm linewidth". *Current Applied Physics,* **6**(6), pp. 1007–1011.

[3] Mavroidis, C., and Dubey, A., 2003. "Biomimetics: From pulses to motors". *Nature,* **2**(9), pp. 573–574.

[4] Dubey, A., Sharma, G., Mavroidis, C., Tomassone, S. M., Nikitczuk, K., and Yarmush, M. L., 2004. "Dynamics and kinematics of viral protein linear nano-actuators for bio-nano robotic systems". In IEEE International Conference on Robotics and Automation, ICRA '04, Vol. 2, IEEE, pp. 1628–1633.

[5] Kang, B. H., Wen, J. T.-Y., Dagalakis, N. G., and Gorman, J. J., 2004. "Analysis and design of parallel mechanisms with flexure joints". In IEEE Conference on Robotics and Automation.

[6] Gorman, J. J., Kim, Y.-s., and Dagalakis, N. G., 2006. "Control of mems

nanopositioner with nano-scale resolution". In ASME International Mechanical Engineering Congress and Exposition, ASME.

[7] Kim, D., Lee, D. Y., and Gweon, D. G., 2007. "A new nano-accuracy afm system for minimizing abbe errors and the evaluation of its measuring uncertainty". *Ultramicroscopy,* **107**(4-5), pp. 322–328.

[8] Kim, D., Kang, D., Shim, J., Song, I., and Gweon, D. G., 2005. "Optimal design of a flexure hinge-based xyz atomic force microscopy scanner for minimizing abbe errors". *Review of Scientific Instruments,* **76**(7), p. N.PAG.

[9] Smith, S. T., 2000. *Flexures: Elements of Elastic Mechanisms*, 1st ed. CRC Press.

[10] Smith, S. T., and Chetwynd, D. G., 1992. *Foundations of ultraprecision mechanism design*, Vol. xv of *Developments in nanotechnology 1053-7465 ; v. 2.* Gordon and Breach Science Publishers, Philadelphia, Pa., U.S.A.

[11] Howell, L. L., 2001. *Compliant mechanisms.* Wiley-Interscience, New York.

[12] Saggere, L., and Kota, S., 2001. "Synthesis of planar, compliant four-bar mechanisms for compliant-segment motion generation". *Journal of Mechanical Design,* **123**, pp. 535–541.

[13] Frecker, M. I., Kota, S., Fonseca, J., and Kikuchi, N., 1995. "A systematic synthesis method for the design of distributed compliant mechanisms". In Fourth National Applied Mechanisms and Robotics Conference, Vol. 2.

[14] Saxena, A., and Ananthasuresh, G. K., 1998. "An optimality criteria approach for the topology synthesis of compliant mechanisms". In ASME Design Engineering Technical Conferences, MECH-5937, ASME.

[15] Bacher, J. P., Joseph, C., and Clavel, R., 2002. "Flexures for high precision robotics". *Industrial Robot,* **29**(4), pp. pp. 349–353.

[16] Lobontiu, N., 2003. *Compliant Mechanisms: Design of flexure hinges.* CRC Press.

[17] Smith, S. T., Chetwynd, D. G., and Bowen, D. K., 1987. "Design and assessment of monolithic high precision translation mechanisms". *Journal of Physics, E: Scientific Instruments,* **20**, pp. 977–983.

[18] Cherala, A., Choi, B.-J., Nimmakayala, P. K., Meissl, M. J., and Sreenivasan, S. V., 2007. "Apparatus to vary dimensions of a substrate during nano-scale manufacturing". *US Patent: 7,170,589 B2 (Date issued : 01/30/2007)*, p. 28.

[19] Yao, Q., Dong, J., and Ferreira, P. M., 2007. "Design, analysis, fabrication and testing of a parallel-kinematic micropositioning xy stage". *International Journal of Machine Tools and Manufacture,* **47**(6), pp. 946–961.

[20] Phillips, J., 1984. *Freedom in Machinery: Introducing screw theory*, Vol. 1. Cambridge University Press, Cambridge.

[21] Phillips, J., 1984. *Freedom in Machinery: Screw theory exemplified*, Vol. 2. Cambridge University Press, Cambridge.

[22] Chen, K.-S., Trumper, D. L., and Smith, S., 2002. "Design and control for an electromagnetically driven x-y-th stage". *Precision Engineering,* **26**, pp. 355–369.

[23] Wischnewskiy, W., Kovalev, S., and Vyshnevskyy, O., 2002. "Adaptive mechanics provides multi-axis motion with sub-nanometer flatness and sub-mrad yaw/pitch/roll". *AZoNanotechnology, (online) http://www.azonano.com,* **ArticleID = 1587**.

[24] Xu, Y., Atherton, T. R., McConnell, M., and Rhead, P., 2001. "Design and characterisation of an ultra-precision x-y stage". *AZoNanotechnology, (online) http://www.azonano.com,* **ArticleID = 1463**.

[25] Chen, S.-C., Golda, D., Herrmann, A., and Slocum, A., 2004. "Design of an ultra precision diaphragm flexure stage for out-of-plane motion guidance". In DETC'04, ASME 2004 Design Engineering Technical Conferences and Computers and Information in Engineering Conference, ASME, p. 7.

[26] Yeo, S. H., Ngoi, B. K. A., Poh, L. S., and Hang, C., 1997. "Cost-tolerance relationships for non-traditional machining processes". *Inter-*

national Journal of Advanced Manufacturing Technology, **13**, pp. 35–41.

[27] Jordan, S., and Marth, H., 2007. "Novel high-bandwidth active parasitic motion compensation for sub-nm planarity in afm and profiler applications". In 22nd Annual ASPE Meeting, ASPE.

[28] Ryu, J. W., and Gweon, D. G., 1997. "Error analysis of a flexure hinge mechanism induced by machining imperfection". *Precision Engineering,* **21**, pp. 83–89.

[29] Niaritsiry, T.-F., Fazenda, N., and Clavel, R., 2004. "Study of the sources of inaccuracy of a 3-dof flexure hinge-based parallel manipulator". In IEEE International Conference on Robotics and Automation, IEEE, pp. 4091–4096.

[30] Huh, J. S., Kim, K. H., Kang, D. W., Gweon, D. G., and Kwak, B. M., 2006. "Performance evaluation of precision nanopositioning devices caused by uncertainties due to tolerances using function approximation moment method". *Review of Scientific Instruments,* **77**(1), pp. 015103–1–9.

[31] Hunt, K. H., 1990. *Kinematic geometry of mechanisms.* Oxford Engineering Science Series - 7. Oxford Science Publications.

[32] Davidson, J. K., and Hunt, K. H., 2004. *Robots and screw theory.* Oxford University Press.

[33] Patterson, T., and Lipkin, H., 1990. "Structure of robot compliance". In ASME Design Engineering Technical Conferences, Vol. 26, pp. 315–322.

[34] Huang, S., and Schimmels, J. M., 2000. "The eigenscrew decomposition of spatial stiffness matrix". *IEEE Transactions on Robotics and Automation,* **6**(2), pp. 146–156.

[35] Lipkin, H., and Patterson, T., 1992. "Geometrical properties of modelled robot elasticity: part 1 - decomposition". In ASME Design Engineering Technical Conferences, Vol. 45, pp. 179–185.

[36] Ciblak, N., and Lipkin, H., 1998. "Synthesis of stiffnesses by springs". In ASME Design Engineering Technical Conferences, pp. 1–10.

[37] Huang, S., and Schimmels, J. M., 2002. "Realization of those elastic behaviors that have compliant axes in compact elastic mechanisms". *Journal of Robotic Systems,* **19**(3), pp. 143–154. 10.1002/rob.10029.

[38] Schimmels, J. M., and Huang, S., 1996. "A passive mechanism that improves robotic positioning through compliance and constraint". *Robotics and Computer-Integrated Manufacturing,* **12**(1), pp. 65–71.

[39] Peshkin, M. A., 1990. "Programmed compliance for error corrective assembly". *Ieee Transactions on Robotics and Automation,* **6**(4), pp. 473–482.

[40] Roth, Z., Mooring, B., and Ravani, B., 1987. "An overview of robot calibration". *Robotics and Automation, IEEE Journal of [legacy, pre - 1988],* **3**(5), pp. 377–385. 0882-4967.

[41] Beyer, L., and Wulfsberg, J., 2004. “Practical robot calibration with rosy”. *Robotica,* **22**, pp. 505–512.

[42] Featherstone, R., 2001. *Robot Dynamics Algorithms*, 1st ed. The International Series in Engineering and Computer Science. Kluwer Academic Publishers.

[43] Zhang, S., and Fasse, E. D., 1998. “Spatial compliance modeling using a quaternion-based potential function method”. *Multibody System Dynamics*, pp. 1–24.

[44] Dai, J. S., and Ding, X., 2006. “Compliance analysis of a three-legged rigidly-connected platform device”. *Journal of Mechanical Design,* **128**(4), pp. 755–764.

[45] Patterson, T., and Lipkin, H., 1990. “A classification of robot compliance”. In ASME Design Engineering Technical Conferences, Vol. 26, pp. 307–314.

[46] Hale, L. C., and Slocum, A., 2001. “Optimal design techniques for kinematic couplings”. *Precision Engineering,* **25**, pp. 114–127.

[47] Pham, H. H., and Chen, I. M., 2005. “Stiffness modeling of flexure parallel mechanism”. *Precision Engineering,* **29**, pp. 467–478.

[48] Moler, C. B., 2004. *Numerical computing with MATLAB.* Society of Industrial and Applied Mathematics, Philadelphia.

[49] Sommer, C., and Sommer, S., 1997. *Wire EDM Handbook*, 3 ed. Advance Publisher, Houston.

[50] McCarthy, J. M., 2000. *Geometric Design of Linkages.* Interdisciplinary Applied Mathematics. Springer, New York.

[51] Myers, R. H., and Montgomery, D. C., 1995. *Response Surface Methodology: Process and Product Optimization using Designed Experiments.* Wiley Series in Probability and Statistics. John Wiley and Sons, New York.

[52] Challis, J. H., 1995. "A procedure for determining rigid body transformation parameters". *Journal of Biomechanics,* **28**(6), pp. 733–737.

[53] Zhang, S., and Fasse, E. D., 2001. "A finite-element-based method to determine the spatial stiffness properties of a notch hinge". *Journal of Mechanical Design,* **123**, pp. 141–147.

[54] Meggiolaro, M. A., Dubowsky, S., and Mavroidis, C., 2005. "Geometric and elastic error calibration of a high accuracy patient positioning system". *Mechanism and Machine Theory,* **40**, pp. 415–427.

[55] Smith, S. T., and Seugling, R. M., 2006. "Sensor and actuator considerations for precision, small machines". *Precision Engineering,* **30**(3), pp. 245–264.

[56] Slocum, A. H., Hardt, D. E., and Greenspan, L., 1988. "Development of a six degree-of-freedom position and orientation sensing device: design

theory and testing". *International Journal of Machine Tools Manufacturing,* **28**(4), pp. 325–339.

[57] Barriere, J. C., Cloue, O., Duboue, B., Fontaine, M., Gautard, V., Graffin, P., Guyot, C., Jiolat, G., Perrin, P., Ponsot, P., Schuller, J., Schune, P., and Reinert, Y., 2005. "Six axis position sensor: principle and calibration". In 6th International Workshop on Research and Education in Mechatronics (REM - 2005).

[58] Fan, K.-C., and Chen, M.-J., 2000. "A 6-degree-of-freedom measurement system for the accuracy of x-y stages". *Precision Engineering,* **24**, pp. 15–23.

[59] Farago, F. T., and Curtis, M. A., 1994. *Handbook of Dimensional Measurement*, 2nd ed. Mensuration. Industrial Press, New York.

[60] Box, G. E. P., Hunter, J. S., and Hunter, W. G., 2005. *Statistics for experimenters: Design, Innovation, and Discovery*, second ed. Wiley series in Probability and Statistics. John Wiley and Sons, Hoboken, New Jersey.

[61] Carretero, J. A., Podhorodeski, R. P., Nahon, M. A., and Gosselin, C. M., 2000. "Kinematic analysis and optimization of a new three degree-of-freedom spatial parallel manipulator". *Journal of Mechanical Design,* **122**(1), pp. 17–24.

[62] Li, Y., and Xu, Q., 2006. "Kinematic analysis of a 3-prs parallel manipulator". *Journal of Robotics and Computer-Integrated Manufacturing,* **(Corrected proof; In press)**.

[63] Hajela, P., and Vittal, S., 2006. "Optimal design in the presence of modeling uncertainties". *Journal of Aerospace Engineering,* **19**(4), pp. 204–216.

[64] Giunta, A., Eldred, M. S., Swiler, L. P., and Trucano, T. G., 2004. "Perspectives on optimization under uncertainty: algorithms and applications". In AIAA/ISSMO Multidisciplinary analysis and optimization, Vol. 10, AIAA, p. 10.

[65] Mawardi, A., and Pitchumani, R., 2005. "Optimal design of a micromachined force gauge under uncertainty". *Journal of Micromechanics and Microengineering,* **15**(12), p. 2353.

[66] J W Wittwer, T. G., and Howell, L. L., 2002. "Surface micromachined force gauges: uncertainty and reliability". *Journal of Micromechanics and Microengineering,* **12**(1), pp. 13–20.

[67] Wittwer, J. W., 2005. "Simulation-based design under uncertainty for compliant microelectromechanical systems". Phd dissertation, Brigham Young University.

[68] Ryu, J. W., Gweon, D.-G., and Moon, K. S., 1997. "Optimal design of a flexure hinge based xy[phi] wafer stage". *Precision Engineering,* **21**(1),

pp. 18–28.

[69] Pham, H.-H., Yeh, H.-C., and Chen, I. M., 2006. "Micromanipulation system design based on selective actuation mechanisms". *The International Journal of Robotics Research,* **25**(2), pp. 171–186.

[70] Paros, J. M., and Weisbord, L., 1965. "How to design flexure hinges". *Machine Design,* **25**, pp. 151–156.

[71] Wu, Y., and Zhou, Z., 2002. "Design calculations for flexure hinges". *Review of Scientific Instruments,* **73**(8), pp. 3101–3106.

[72] Bertsekas, D. P., 2003. *Nonlinear programming*, 2nd ed. Athena Scientific, Belmont, Mass.

[73] Ventakataraman, P., 2002. *Applied optimization with MATLAB programming.* Wiley, New York.

[74] Chen, S.-C., and Culpepper, M. L., 2006. "Design of a six-axis micro-scale nanopositioner–[mu]hexflex". *Precision Engineering,* **30**(3), pp. 314–324.

[75] Henein, S., 2002. "Movement transmission unit and movement transmission apparatus". *US Patent: 6453566 (Date issued: 09/24/2002),* p. 20.

[76] Davidson, J. K., and Shah, J. J., 2002. "Geometric tolerances: a new application for line geometry and screws". *Proceedings of Institution of*

Mechanical Engineers, Part C; Journal of Mechanical Engineering Science, **216**, pp. 95–104.

[77] Angeles, J., 1997. *Fundamentals of robotic mechanical systems: theory, methods and algorithms*, 1st ed. Mechanical Engineering Series. Springer-Verlag, New York.

[78] Dai, J. S., Li, D., Zhang, Q., and Jin, G., 2004. "Mobility analysis of a complex structured ball based on mechanism decomposition and equivalent screw system analysis". *Mechanism and Machine Theory,* **39**, pp. 445–458.

[79] Gogu, G., 2005. "Mobility of mechanisms: a critical review". *Mechanism and Machine Theory,* **40**, pp. 1068–1097.

[80] Dai, J. S., Huang, Z., and Lipkin, H., 2006. "Mobility of overconstrained parallel mechanisms". *Journal of Mechanical Design,* **128**, pp. 220–229.

[81] Huang, S., and Schimmels, J. M., 2002. "The duality in spatial stiffness and compliance as realized in parallel and serial elastic mechanisms". *Journal of Dynamic Systems, Measurement, and Control,* **124**(1), pp. 76–84.

Vita

Chinmaya Baburao Patil was born on September 7, 1978, in Hubli, India, as the second son of Baburao Rangarao Patil and Leela Baburao Patil. He completed lower division education in Bangalore and Hubli, and high school in Belgaum. He then enrolled in the Karnataka Regional Engineering College (now, National Institute of Technology), Surathkal, India, for undergraduate education in Mechanical Engineering, in 1996. He graduated in 2000, receiving a Gold Medal from the Mangalore University in the discipline of Mechanical Engineering. During the following year, he was employed as a Design Engineer with Tata AutoComp Ltd., Pune.

In Fall 2001, he entered The University of Texas at Austin to pursue graduate studies in Mechanical Engineering, with a scholarship from the distinguished J. N. Tata Endowment Trust. He received the Master of Science degree in August 2003, having written the thesis titled ‘Antilock brake system redesign and control prototyping for a one-fifth scaled test vehicle’, under the supervision of Dr. Raul G. Longoria. The research was supported by National Instruments. His current research on precision mechanisms design under the supervision of Drs. Raul G. Longoria, and S. V. Sreenivasan, is partly supported by Molecular Imprints. His teaching experience includes serving as a Tutor with the College of Engineering’s Equal Opportunity in Engineering program during Spring, 2002, and as a Teaching Assistant for ME 244L Dynamic Systems and Control from Fall 2003, until Fall 2007. He is the recipient of David Bruton Jr. Fellowship in 2005, and Professional Development Award in 2007, both from Office of Graduate Studies at The University of Texas at Austin.

Permanent address: 7201 Wood Hollow Dr. #388
Austin, Texas 78731

This dissertation was typeset with LaTeX[†] by the author.

[†] LaTeX is a document preparation system developed by Leslie Lamport as a special version of Donald Knuth's TeX Program.